The effect of water-soluble polymers on water-alternating CO_2 performance in porous media

T.J. van Wieren

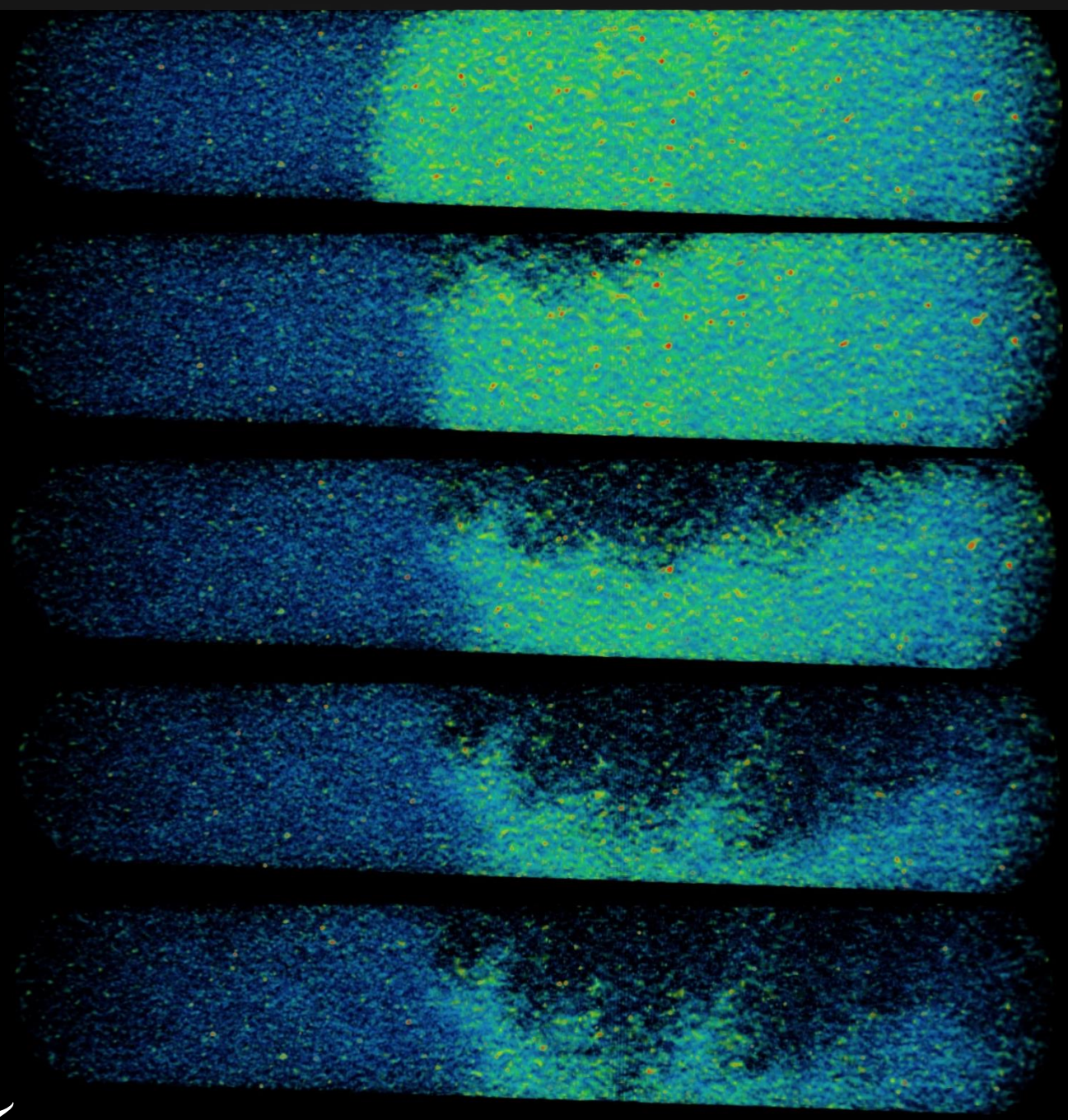

Delft University of Technology

TU Delft

The effect of water-soluble polymers on water-alternating CO_2 performance in porous media

by

T.J. van Wieren

to obtain the degree of
Master of Science
in Applied Earth Sciences
at the Delft University of Technology,
as a project for the consortium of Shell, Dutch Polymer Institute and SNF Floeger,
to be defended publicly on Wednesday August 31, 2022 at 10:30 AM.

Student number:	4572289	
Project duration:	November 1, 2021 – August 31, 2022	
Supervisors:	Prof. dr. P.L.J. Zitha	TU Delft
	Dr. M. Mirzaie Yegane	TU Delft
Thesis Committee:	Prof. dr. P.L.J. Zitha	TU Delft
	Dr. M. Mirzaie Yegane	TU Delft
	Dr. A. Fadili	Shell
	Dr. K.H.A.A. Wolf	TU Delft
Faculty:	Faculty of Civil Engineering and Geosciences	Delft

This thesis is confidential and cannot be made public until October 31, 2022

TU Delft

Abstract

In order to supply the demand of oil, enhanced oil recovery (EOR) techniques are nowadays widely applied in the oil recovery industry to maximize reservoir sweep efficiencies. CO_2-EOR method has been largely used in the petroleum industry for several decades, which can contribute to the reduction of global greenhouse gas emission through CO_2 sequestration in geological formations besides the elevation of oil recovery levels. Conventionally, CO_2 is implemented as a continuous flooding scheme. But CO_2 flooding is prone to unfavorable displacements, viscous fingering, gravity segregation and early breakthrough due to the high mobility ratio, low viscosity and low density of CO_2. A method to overcome these problems is the alternation of water and CO_2 slugs. This method, better known as water alternating gas (WAG) injection, is widely applied through the field. But despite the successes of the WAG injection scheme, the method still suffers from a relatively poor mobility ratio and gravity override. In this experimental study, the performance of the polymer assisted water alternating gas (PA-WAG) EOR method is examined. This method makes use of the high viscosity of the polymer solution in combination with immiscible CO_2, to improve the improve the mobility ratio, volumetric sweep efficiency as with that the ultimate recovery of the WAG process. For the polymer, a specially modified polymer is considered, which uses the ATBS (2-acrylamido-terbutylsufonic acid) addition to HPAM in order to improve the stability of the polymer under reservoir conditions. In this thesis, the displacement and recovery performance of the ATBS-modified HPAM polymer is studied via a series of core-flood experiments and the stability is tested via polymer aging in the presence of CO_2. The results of this work have shown that the addition of the ATBS-modified HPAM polymer to the water in the WAG method increased the recovery by 10% over the normal WAG injection, by improving the mobility ratio and displacement efficiency. By implementing the PA-WAG on a carbonate rock saturated with crude oil, a base line experiment with regarding reservoir simulated recovery was established, with a recovery of 76%. The stability test under the presence of CO_2 showed that the dissolved CO_2 impacts the polymer viscosity. After the initial decrease in apparent viscosity to 54% of the original viscosity, the ATBS-modified HPAM polymer was able to recover its viscosity to 84% of its original apparent viscosity after 29 days of aging. These results were achieved under full saturation of the polymer solution with CO_2 . In addition, the impact of CO_2 at PA-WAG flooding CO_2 concentrations was evaluated, which showed now degradation with the exposure to CO_2. The study concludes that the ATBS-modified HPAM polymer performs excellently in the PA-WAG method for enhanced recovery, significantly outperforming the WAG injection method.

Acknowledgements

For this project, I had the change to work in the Dietz laboratory on the faculty of Civil Engineering and Geosciences and conduct experimental work. I want to extend my sincere thanks to Prof. Dr. Pacelli Zitha, my head supervisor, for granting this opportunity and sharing his experience, time and knowledge throughout the full extend of this thesis. For the daily supervision, I would like to thank Mohsen Mirzaie Yegane for his devotion into the project and granting me his continuous support, guidance, knowledge and encouragements to deliver quality work. Thanks go to the committee members of my graduation, who showed interest in my work and provided me the chance to graduate.

The experimental work in the Dietz laboratory would not be possible without the help of the technical support staff, in particularly Michiel Slob and Ellen Meijvogel-de Koning. Without the assistance and expertise of Michiel for building experiment set-ups and Ellen's extensive knowledge about the medical CT-scanner, my experimental work would not have been possible.

The thesis was a part of a collaboration study with Shell, DPI and SNF Floeger. I am grateful to Shell, DPI and SNF Floeger for funding this project, as well as supplying materials and providing feedback and knowledge throughout the research.

Lastly, I would like to show my gratitude to my family, girlfriend and close friends, for supporting me throughout this thesis and providing me with comfort, a laugh or a beer from time to time.

Contents

List of Figures

List of Tables

Nomenclature

Abbreviations

Abbreviation	Definition
% RF	percentage of total recovery
1D	one dimensional
AMPS	2-acrylamido-2-methyl propane sulfonic acid
ATBS	acrylomido tertiary butyl sulfonate
BT	breakthrough
°C	degrees Celsius
CGI	continuous gas injection
CO_2	carbon dioxide
CT	computed tomography
cP	centipoise
demi	demineralized
dP	differential pressure
EOR	enhanced oil recovery
HPAM	partially hydrolyzed polyacrylamide
HU	Hounsfield units
IFT	interfacial tension
M	mobility ratio
MMP	minimum miscibility pressure
OIIP	oil initialy in place
OIP	oil in place
PAM	polyacrylamide
PA-WAG	polymer assisted-water alternating gas
PEEK	polyether ether ketone
PF	polymer flooding
pH	pondus Hydrogenium
ppm	parts per million
PV	pore volumes
rep.	repetition
RF	recovery factor
WAG	water alternating gas
wt%	weight percent

Symbols

Symbol	Definition	Unit
A	area	m^2
a	width transition zone	-
CT	Computed-Tomography response of the core	HU
CT_{air}	Computed-Tomography response of the gas phase	HU
CT_{brine}	Computed-Tomography response of the water phase	HU
CT_{dry}	Computed-Tomography response of the dry core	HU

Symbol	Definition	Unit
CT_o	Computed-Tomography response of the oil-saturated core	HU
CT_{oil}	Computed-Tomography response of the oil phase	HU
CT_{wet}	Computed-Tomography response of the brine-saturated core	HU
dP	differential pressure	bar
dz	length of capillary	m
g	gravitation acceleration	m/s^2
h	displacement height	m
k	permeability	$Darcy$
k_o	effective oil permeability	-
k_{rg}	relative permeability gas	-
k_{ro}	relative permeability oil	-
k_{rp}	relative permeability polymer	-
k_{rw}	relative permeability water	-
k^e_{rg}	relative endpoint permeability gas	-
k^e_{ro}	relative endpoint permeability oil	-
k^e_{rp}	relative endpoint permeability polymer	-
k^e_{rw}	relative endpoint permeability water	-
L	length	m
n	power law coefficient	-
P_{in}	inlet pressure	bar
P_{out}	outlet pressure	bar
R	radius	m
Q	total discharge/volumetric flow rate	m^3/s
$R_{v/g}$	viscous/gravity number	-
S_g	gas saturation	-
S_{gt}	trapped gas saturation	-
S_o	oil saturation	-
S_{oi}	initial oil saturation	-
S_{or}	residual oil saturation	-
$S_{or,PF}$	residual oil saturation after polymer flooding	-
S_{or,CO_2}	residual oil saturation after CO_2 flooding	-
$S_{or,cycle1}$	residual oil saturation after cycle 1	-
$S_{or,cycle2}$	residual oil saturation after cycle 2	-
S_w	water saturation	-
S_{wc}	conate water saturation	-
u_{total}	superficial velocity	m/s
$\dot{\gamma}$	shear rate	s^{-1}
$\dot{\gamma}_A$	apparent shear rate	s^{-1}
$\dot{\gamma}_{crit}$	critical shear rate	s^{-1}
$\Delta\rho$	density difference	kg/m^3
ΔP	differential pressure	bar
η	viscosity	cP or $Pa.s$
η_A	apparent viscosity	cP or $Pa.s$
η_g	gas viscosity	cP or $Pa.s$
η_o	oil viscosity	cP or $Pa.s$
η_t	viscosity at time	cP or $Pa.s$
η_w	water viscosity	cP or $Pa.s$
$\eta_{t=0}$	viscosity at time 0	cP or $Pa.s$
η_0	viscosity at zero shear rate	cP or $Pa.s$
η_∞	viscosity at infinity shear rate	cP or $Pa.s$
$\eta^{\%}$	viscosity % ratio	-
λ	relaxation time	s

Symbol	Definition	Unit
ν	Darcy velocity	m/s
π	pi	-
σ_ω	wall shear stress	Pa
ϕ	porosity	-

1 Introduction

1.1. General introduction

The last decade and the coming years are vital with respect to the energy transition that needs to be made, in order to guarantee a live-able world for the generations to come. A large focus in this transition must be set on finding alternative ways to supply the energy demand and to reduce greenhouse gasses that are and are going to be emitted, especially CO_2. But with forecasts [3], oil is expected to remain the largest energy supply for the coming future. Not only are renewable energy projects often far from profitable, but oil plays a role as well in the production of, e.g., plastics, lubricants, candles and other day to day products besides the fuels it produces, making the oil production quite a necessity. While the world is searching and developing new energy sources and the oil demands should be decreased to meet environmental agreements, the demand of oil is projected by various forecast to grow further instead [51, 19], while others project a decline with the new momentum [3]. In order to provide for the demand and while doing that, be as efficient as possible with reducing CO_2 along the way, innovative methods are needed to be implemented in the oil recovery sector.

The development of an oil field can be divided into three stages of production, namely the primary, secondary and tertiary recovery [26]. With primary recovery, the oil is produced via natural mechanisms and is mainly pressure driven. This leads to depletion of reservoir pressure over the course of this primary recovery. The secondary recovery techniques are mostly used to maintain the reservoir pressure during production, often done by implementing water and gas injections. With this injection, the oil is displaced to the production well and can be subsequently recovered. The injection techniques applied after this initial pressure maintenance of the reservoir can be labelled under tertiary recovery modes and are most often called enhanced oil recovery (EOR) methods, or as Lake (1989)[26] defines: techniques that recover oil by the injection of external materials which are originally not present in the reservoir. These tertiary recovery methods in general improve the oil recovery from conventional fields by 5-20% from the 35-45% normally reached with only the secondary injections [57]. With the discovery of new oil fields to an almost all time low in the year 2015 and the demand of oil continuing to increase, the oil in place from already existing fields has become an important target for oil companies by using new and innovative EOR techniques to improve the recovery [42].

CO_2 has been used for decades to enhance the recovery levels of oil production [63, 30, 32]. Besides steam flooding, CO_2 injection is the most applied EOR method in the world [32]. CO_2 EOR can utilize captured and stored CO_2 to enhance recovery levels, while decreasing greenhouse gas. But CO_2 flooding suffers from relative poor sweep efficiency. The low density and viscosity of CO_2 compared to oil lead to gravity segregation and fingering, resulting in early breakthrough and production of the injected gas instead. New methods have been developed in the past. One example has been the water alternating gas (WAG) injection scheme. This combines the water and gas flooding techniques to improve the gravity segregation and high gas mobility to enhance recovery even further. But despite all the successes of WAG implementations for EOR, the sweep efficiency and use of CO_2 gas are still not optimal.

To overcome the issues regarding displacement efficiency and early breakthrough encountered in the WAG method, a new technique has been proposed. It uses the superior mobility control of polymer flooding with the solubility and displacement of CO_2, namely polymer alternating gas (or polymer assisted water alternating gas (PA-WAG)). But polymers are not always as stable when reservoir conditions are applied to it, such as higher pressure, temperature, salinity levels and likewise, the presence

of CO_2 as it lowers the pH of the solution in contact with water. So polymers are synthesized in order to better withstand these conditions and retain their viscosifying powers. In order to be implemented widely as an EOR method, it is necessary that extensive research is conducted regarding the recovery levels, flow regimes through the reservoir and interaction behaviours when injecting these modified polymers in a reservoir alongside carbon dioxide.

1.2. Research background

Worldwide, more than 60% of the oil reserves resides in carbonate reservoirs. Those reservoirs are mostly oil-wet and display typically recoveries lower than 40%. The targeted field behind this study is such a carbonate reservoir, where the recovery is the field is to be enhanced by an EOR method. For this enhancement of recovery, the polymer assisted water alternating gas method, using an AMPS modified HPAM polymer, is considered. This thesis forms the basis of a elaborate study towards the feasibility of the modified polymer in the PA-WAG injection method. The stability of the polymer is assessed, along with the flow regimes, displacement improvements over the normal WAG injection and in the end the recovery achieved with the PA-WAG method, starting in Bentheimer sandstone cores and eventually testing the method on carbonate rocks.

1.3. Research questions and objectives

The polymer assisted water alternating g (PA-WAG) injection is designed to improve the performance of the water alternating gas (WAG) injection scheme for enhanced oil recovery purposes. With this research, the aim is to study the behaviour of CO_2 and the selected polymer during the PA-WAG injection for oil recovery and therewith improve the sweep efficiency and oil recovery over the WAG injection. The work is structured around two main hypotheses: (1) sweep efficiency and hydrocarbon recovery is improved with respect to Water Alternating Gas optimisation with the use of the modified polymer assisted water alternating gas technique, and (2) carbon dioxide will have minimal impact on the AMPS modified HPAM polymer slug behaviour with respect to the viscosity reduction during the flooding process. These hypotheses are built up from under-laying sub-questions, disclosed below:

(1) Sweep efficiency and hydrocarbon recovery improvements by applying the polymer assisted water alternating gas EOR method.

Here, the sub-question arises in order to validate the first hypotheses: which flow patterns can be expected during the PA-WAG cycles through real porous media? Regarding this sub-question, the hypothesis holds that the polymer injected for mobility control during the PA-WAG cycles will stabilize the sweep fluid front, canceling significant viscous fingering and gravity segregation during flooding. This results in a noticeable delay in gas breakthrough, significant water cut decrease and reduced utilization of CO_2 and polymer. The objective here is to perform representative core-floods in a systematic study, comparing the results and mechanisms from separate gas flooding, polymer flooding, WAG and PA-WAG. During those core-floods, the goal is to not only display the potential enhanced recovery of oil, but visualise the flow patterns through the core with the use of a CT-scanner during the different cycles of the flooding procedures and analyse the displacement efficiency of the PA-WAG over the other flooding techniques.

(2) Effect of carbon dioxide during flooding process on the viscosity reduction of AMPS modified HPAM polymer slug.

For this second hypothesis, the first sub-question reads: what is the effect of CO_2 dissolution on the polymer? The hypothesis associated with this sub-question is that the presence of CO_2 in the system alongside the polymer will have a multistage impact of decreases and increases in the viscosity of the polymer. This occurs due to the changes in pH by the formation of carbonic acid from CO_2 in contact with water. The lowered pH from this acid formation can neutralize the charges on the polymer backbone and result in a drop in viscosity. Subsequently, after an initial reduction in viscosity, it can recover as a consequence of the hydrolysis reaction promoted by the lower pH of the solution. The objective here is to investigate the rheology response of the SAV-10 XV polymer in combination with CO_2 dissolution. Important to observe alongside the viscosity fluctuations of the polymer is the pH value during

the dissolution, being the expected cause of both the decrease and followed increase of viscosity of the polymer.

1.4. Thesis outline

The research is structured around a series of core-flood experiments in cores that represent sandstone and carbonate reservoirs. At the end, the core-floods are closed off with a final core-flood at reservoir conditions, using a crude oil instead of the nonpolar n-hexadecane in Indiana limestone at the same temperature and pressure as for the Bentheimer experiments. All of these core-floods are aided with dual energy CT-scans, capable of analyzing three-phase flow systems. Besides the core-floods, the effect of dissolved CO_2 in the polymer solution will be investigated during a degradation experiment over a longer time period.

The thesis is organized in the form of five chapters, including this introduction, where the research objectives from section 1.3 are addressed. In chapter 2, a theoretical background study is performed and and a thorough review of previous studies and literature concerning PA-WAG, WAG and polymer and CO_2 behaviour in EOR processes are discussed. Chapter 3 states the used materials and methods of the experimental study, discussing the used chemicals, cores, experimental set-ups and procedures of the individual experiments, CT-scanner and data processing methods. The materials and methods are succeeded by the presentation of the retrieved results from those experiments in chapter 4, which are thoroughly discussed at the end of this chapter. Finally, the research questions are answered in the conclusions section, with the recommendations for future work given.

2
Theoretical Background

2.1. Water-soluble polymers flow in porous media

With the easy application to increase the viscosity of water, water soluble polymers have been an attractive method for multiple decades for enhanced oil recovery (EOR) purposes. Characterisation of the polymer and its rheological behaviour under reservoir conditions are an important part for the successful appliance of polymers in the field of EOR.

Polymers are molecules with long chains of repeated smaller sub-units of atom groups (monomers) that form the large molecule. The polymer can consist out of two distinctive monomers, then referred to as a copolymer (three monomers will result in a terpolymer etc.), or just from one monomer, called a homopolymer [33]. Polymers can be subdivided into two groups: biopolymers and synthetic polymers. Synthetic polymers are mostly used for EOR purposes these days, while biopolymers have clear advantages regarding their shear resistance, insensitivity to high salt and temperature levels and high viscosifying powers [23]. Biopolymers however are very susceptible to biodegradation [23, 37] and are less mature than synthetic polymers concerning field application, logistics, handling, product design (easily adjustible molecular weight) and lab evaluation, hence the nowadays preferred use of synthetic polymers over biopolymers [23]. Polymers are known for their very high molecular weights (varying up to $30 * 10^6 \frac{g}{mol}$ [37]), that is not fixed on one value within a volume of polymers, but forms a distribution of molecular weights. The average weight can by calculation to take the sum of the total weight of the molecule, divided by the total amount of polymer molecules.

2.1.1. Polymer characteristics, rheology and performance

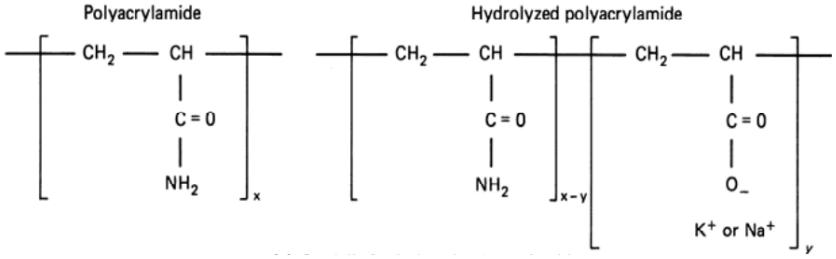

Figure 2.1: The structures of PAM on the left and HPAM on the right [26].

Most commonly used synthetic polymer in field applications is hydrolysed polyacrylamide (HPAM), mainly because of its high water solubility [37, 27, 46]. HPAM is derived from PAM (polyacrylamide) via a partial hydrolysis, which made anionic (negative charged) carboxyl groups (COO^-) to dispersed along the backbone chain of the polymer (see Figure 2.1. This partial hydrolysis causes the HPAM molecule to be negatively charged, which attributes for most of the physical properties of HPAM. Solved in flooding drive water, the oil-water mobility ratio improves [37, 27, 26, 52, 23, 12] via Equation 2.1:

$$M = \frac{\lambda_w}{\lambda_o} = \frac{k^e_{rw}\eta_o}{k^e_{ro}\eta_w} \tag{2.1}$$

, where λ is phase mobility, k^e_r is endpoint relative permeability and η is viscosity. Lower mobility ratios represent better fluid displacements and with the mobility ratio below 1, the displacement can be con-

sidered favourable.

With better mobility control of the present phases in the system, the drive water front is stabilised, counteracting the early breakthrough of water via viscous fingering occurring in independent water flooding (see Figure 2.2).

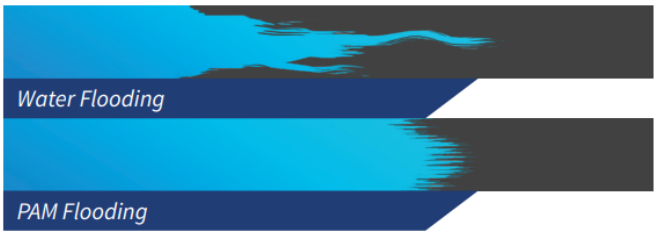

Figure 2.2: Stabilised front by the addition of polyacrylamide to the drive water [12].

This mobility control by the application of polymer in the drive water leads to an increased volumetric sweep efficiency, which is achieved by two principal mechanisms: (1) by the increased viscosity of the drive water and (2) by the significant decrement of the relative permeability of the aqueous phase, while the oil relative permeability decreases minimally [37, 64, 26]. The latter is likewise called a decrease in disproportionate permeability, which is the result of a formed layer of absorbed polymer on the pore walls and with that the segregation of both water and oil fluid-flow pathways [37]. The former mechanism is due to two reasons: (1) the degree of hydrolysis and (2) the high molecular weight of the polymer [26, 37]. As mentioned above, the hydrolysis of the PAM induces negative charges in the form of carboxylate groups along the backbone of the polymer. This causes anionic repulsion between separate polymer molecules and polymer segments of the same molecule, which lead the expansion and elongation of the polymer chains in water and to an increase of the viscosity of the aqueous phase [26, 37]. The hydrolysis is typically around the 30%-35%. This is optimised in order to make it soluble in water (when to small, it will not dissolve) and not to sensitive to reservoir characteristic such as elevated levels of salinity and hardness [26].

The specified mechanisms and sub-mechanisms that provide the polymer of its viscosifying power are however affected by the increased levels of salinity, hardness, shear rate and temperature, which are commonly characteristics of reservoir conditions. These effects need to be analysed in order to understand the rheological behaviour of the polymers.

2.1.2. Elevated salinity and hardness

The molecule of HPAM has a flexible chain structure, often referred to in polymer chemistry as a random coil. HPAM is also a polyelectrolyte, meaning it interacts heavily with present ions in the solution, or rather to the ionic strength of the aqueous solvent, due to the flexible chain structure [52, 37]. At low levels of salinity and hardness, the flexible coil of the HPAM molecule experiences electrostatic repulsion between the anionic groups along the polymer backbone chain. This repulsion would be not ionic-ally shielded, which causes a comprehensive expansion of the polymer molecule [26, 46] and a resulting high viscosity. But when the polymer molecules are exposed to high levels of salinity and hardness, the backbone fixed negative charges are interacting with the mobile ions in the solution. This will lead to the formation of an electrical double layer with counter-ions, which causes ionic shielding [26, 2, 46]. The freely rotation carbon-carbon bonds of the polymer molecule allow for the polymer to collapse or coil up, in order to reduce the surface free energy (see Figure 2.3)[26, 31]. This shrinking or coiling of the polymer molecules at high salinity and harness causes a reduction in the hydrodynamic radius of the polymer coils, resulting in a viscosity loss of the solution [37]. Following Akbari et al.(2017)[2], the size of the coil of the polyelectrolyte can be approximated as a function of the double layer repulsion and the polymer configuration. The repulsive energy is in this method balanced by the energy loss due to the changes in polymer configuration to a lower energy state (increased coiling of the molecule).

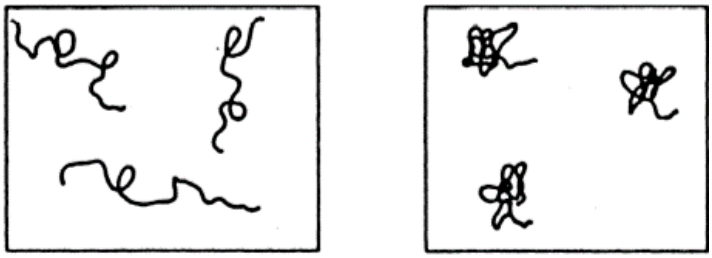

Figure 2.3: The effect of low and high salinity/hardness levels on the polymer molecule structure. Left: low salt/hardness. Right: high salt/hardness[52].

In the presence of divalent ions, such as Ca^{2+} and Mg^{2+}, the viscosity loss is higher, caused by the higher charge and polarizability which inflicts an even tighter coil of the polyelectrolyte compared to the monovalent ions Na^{+} and Ka^{+} [2]. Besides the increased viscosity loss by polymer coiling, the divalent cations present at high salinity can form polyion-metal structures, which results in polymer precipitation and with that loss of viscosity as well [37].

2.1.3. Temperature effects

Besides elevated salinity and harness, reservoirs are generally characterised with associated high temperatures. With increasing temperatures, the loss of viscosity becomes higher and polymer precipitation increases as a result of ongoing encouragement of hydrolysis of the polymer backbone chain [37]. This continued hydrolysis causes further interaction between the ions in the solvent and the charged backbone of the polymer and especially strong with the carboxylate group and divalent cations Ca^{2+} and Mg^{2+} [37, 23]. The interaction with divalent cations results in both intramolecular crosslinking and decreasing the polymers solubility, which in turn induce precipitation at beyond temperatures indicated as the cloud point temperature[23]. Following Jouenne(2020)[23], this cloud point temperature depends on the level of hydrolysis, harness and salinity expressed as the ratio of divalent cations.

2.1.4. Polymer rheology in bulk and porous media

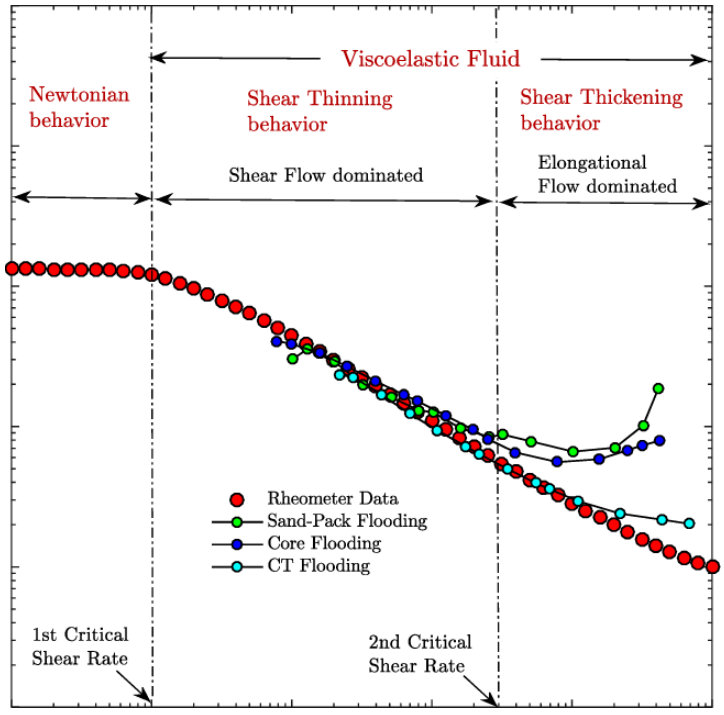

Figure 2.4: The shear rate dependency of the pseudoplastic polymers, with shear rate (1/s) on the horizontal axis and apparent viscosity (η_A(cP)) on the vertical axis. [44].

When polymer solutions are exposed to increased shear rates, the viscosity of the polymer will react accordingly, making the polymers behaving as a pseudoplastic. The viscosity dependent on shear rates displays three primary stages. When applying low shear rates, polymer viscosity shows in-dependency of shear rate, or better known as Newtonian behaviour. After the 1^{st} critical shear rate, the polymer enters the viscoelastic fluid domain. Here, the pseudoplastic polymers exhibit a decreasing viscosity with increasing shear rates (shear thinning behaviour) in dilute solutions [37, 26, 2, 52, 44]. This behaviour is caused by the disentanglement of the polymer chains and the elongation along the flow direction during shear flow domination. The pseudoplastic behaviour of the polymer solution can be described by the power-law model [26, 44]. If the shear flow further increases until very high shear rates above a 2^{nd} critical rate, polymer solutions tend to display shear thickening, or dilatant, behaviour under elongational flow domination [37, 52, 44]. For dilute homogeneous polymer solutions exposed to only rotational shear-viscosity measurements, this behaviour of shear thickening is not commonly seen [52, 44], but can be observed in polymer flooding in porous media. Following Rock et al.(2020)[44], it is believed that shear thickening occurs by the absence of flow motion, since increased viscosity of the solution is generally elucidated with the stretching of the polymer chain. With the high shear rates and this stretching, the polymer molecule can not re-coil itself and by that, the motion of the polymer is dominated by elongational flow and the viscosity is specified as elongational viscosity. The stages which the polymer solution is subjected to with increasing shear rates are visualised in Figure 2.4. During the stage at which the polymer solution is subjected to elongational flow, elastic responses of the solution lead to high elongational viscosity and consequently high elongational stresses in fact pull the molecule of the polymer apart. This behaviour is referred to as shear degradation.

2.1.5. Polymer retention in porous media

When a polymer solution flows through porous media, three mechanisms play a role in the retention of the polymer: adsorption, mechanical entrapment and hydrodynamic retention [37, 52]. Adsorption is the interaction between the molecules of the polymer and the solid rock surface, which is mediated by the (aqueous) solvent [37, 52, 17]. This interaction is results in the binding of the polymer molecule on the solid rock mainly by physical adsorption in the form of van der Waals forces and hydrogen bonding, rather than chemisorption (full chemical bonds are formed) [37, 52, 17]. In principle, the absorption onto the rock surface is caused by an overall low free energy. With polymer adsorbed to the rock, water molecules are released from the solution and entropy is increased. Reduction of bulk polymer in the solution, absorption being the only mechanism to do that [52], also increases entropy. This entropy increase is countered by the decrease in entropy caused by the configurational freedom loss from the polymer absorbed on the rock surface [17].

Retention resulting of mechanical entrapment occurs in porous media when large polymer molecules trapped in small pore throats [37, 52, 17]. When this happens, the relative pore throat size further decreases resulting in an increase in probability to trap more and smaller polymer molecules, leading through this self-amplifying process to pore-clogging [37]. The entrapment distribution of polymer molecules via the mechanical mechanism shows generally a trend, with highest retention close to the inlet and a decrease approximately exponential along the core length to the outlet [52].

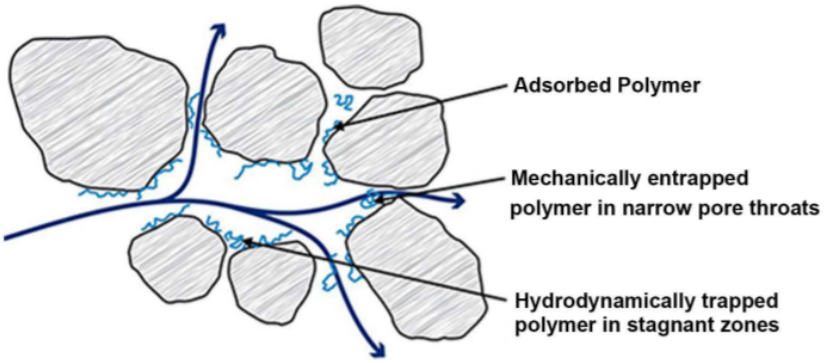

Figure 2.5: Overview of the retention mechanisms in porous media [53].

Hydrodynamic retention, just as mechanical retention, relays on the flow through porous media of the

solvent. The entrapment is caused by an elevation in hydrodynamic drag forces that act upon the polymer. This mechanism shows a dependency to flow rates: increased flow rate results in entrapment of polymer molecules in stagnant flow regions in the porous media, causing a local increase of polymer viscosity above the injected solvent. But when the flow is decreased or stopped, these trapped molecules may diffuse out of these regions into the flow channels, making the hydrodynamic retention reversible [37, 52].

The overall retention in a core-flood, also referred to as dynamic adsorption (DA), can be measured by adding a non absorbing tracer (e.g. potassium iodide) to the solution. The effluent after the experiment is then analysed in order to establish the fluctuation in polymer and tracer over elapsed time, which will provide the levels of polymer adsorption by the porous media. This can be achieved by the single injection method, where the tracer and polymer are injected simultaneously, after which the normalized concentrations (the effluent concentration divided by the original concentration) are displayed against pore volumes injected. Thereafter, the area between the two curves minus the inaccessible pore volume provides the absorption level [37].

2.2. CO_2 flow in porous media

For several decades, CO_2 has been used in the form of continuous injection for enhanced oil recovery for mostly extracting light to medium oils from low permeable reservoirs that approach a mature state. In view of the energy transition, it plays a role in reducing green house gasses by storing CO_2 while enhancing recovery. But with injecting for flooding purposes at reservoir conditions in the presence of multiple phases such as an oil or aqueous phase, CO_2 behaves characteristically with factors such as elevated temperatures and pressures. For a proper understanding of CO_2 usages for flooding purposes, behavioural knowledge under these conditions is desired.

2.2.1. CO_2 properties

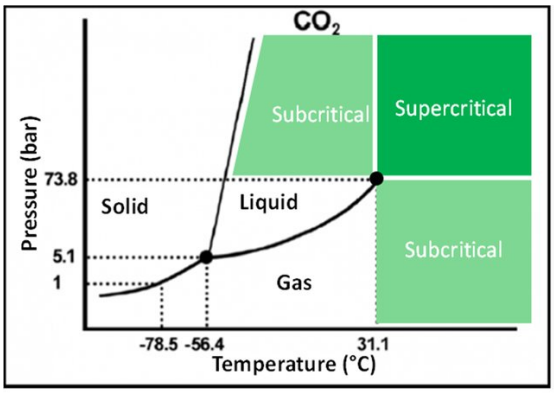

Figure 2.6: CO_2 phase diagram [25].

Standard conditions		
Molecular weight	44.01	g/mol
Density	1.84	kg/m^3
Viscosity	0.0146	cP
Critical point		
Critical pressure	73.8	bar
Critical temperature	31.05	°C
Critical density	440	kg/m^3
Critical viscosity	0.0035	cP
Triple point		
Triple point pressure	-56.4	°C
Triple point temperature	5.10	bar

Table 2.1: CO_2 properties

In Table 2.1, the properties of CO_2 at normal, critical and triple point conditions are displayed. Using CO_2 for flooding purposes in EOR, variations in phases of CO_2 can be present depending on temperature, pressure and composition (see Figure 2.6). At higher pressures and temperatures than the critical point, CO_2 will be in the supercritical state, with a density close to that of the liquid phase, but the viscosity of the gaseous phase (0.05-0.08 cp) [15].

The supercritical state, CO_2 preforms better in oil recovery than the gaseous state, due to the increased density. But with low viscosity compared to the oil phase, also in supercritical state, the mobility ratio from Equation 2.1 will remain unfavourable, leading to a less effective displacement of oil with the formation of viscous fingering (Figure 2.2) through high permeable layers and result in early CO_2 breakthrough at the outlet. Besides this effect, the lower density of CO_2 in every state compared to oil will result in gravity segregation, or gravity override, placing the CO_2 on top of the oil phase along the length of the reservoir, likewise causing early CO_2 production at the outlet. These phenomena cause a ineffective areal sweep of the in place oil (see Figure 2.7a) [33, 15]. The viscosity is found to be highly dependable on pressure and temperature, with a considerable increase in viscosity with increasing pressure for given temperatures, visible in Figure 2.7b.

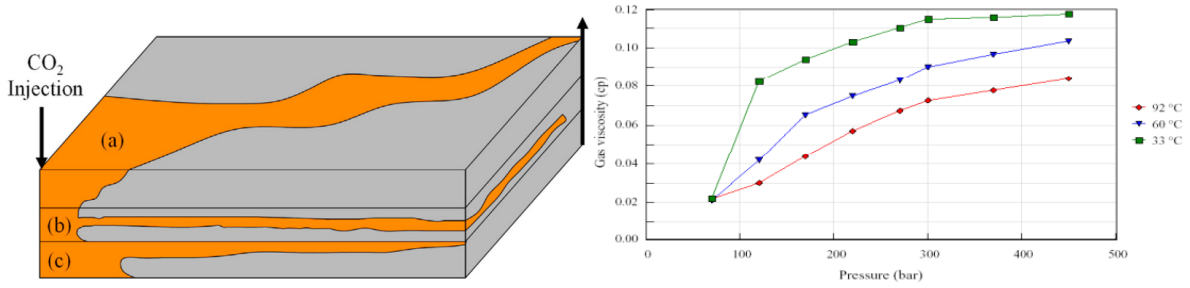

(a) (b)

Figure 2.7: (a) The complications in CO_2 flooding because of the highly mobile CO_2, with a: poor areal sweep, b: gas channeling or viscous fingering and c: gravity segregation [33]. (b) CO_2 viscosity depending in pressure and temperature [34].

2.2.2. CO_2 and oil interaction

With injecting CO_2 for EOR purposes, the CO_2 will interact with the oil phase in the reservoir. As explained in section subsection 2.2.1, the displacement of oil with the use of CO_2 often experiences complications. But when the so called minimum miscibility pressure (MMP) is reached and the CO_2 becomes miscible with the oil phase, the CO_2 -EOR process typically achieves higher recoveries rather than the immiscible state of CO_2 that experiences more severely the complications from Figure 2.7a. From the study of Wang et al.(2021)[58], it is clear that the MMP of CO_2 is temperature depended and decreases with decreasing temperature. At the reservoir conditions for this study of 40°C and 20 bar, as stated in section 1.4, the experimental pressure during the core-floods and with that of the injected CO_2 with some margin below the MMP for an CO_2 /water/n-hexadecane system (Table 2.2). The experiments are therefore performed in immiscible conditions for CO_2 injection.

Table 2.2: Minimum miscibility pressures of CO_2 at different pressures for the experimentally retrieved data and computed data, including the temperature condition of 40°C [58].

T (°C)	$CO_2/H_2O/n\text{-}C_{16}H_{34}$ exp. (MPa)	$CO_2/H_2O/n\text{-}C_{16}H_{34}$ cal. (MPa)
40.3	7.6	8.35
55.4	10.2	10.93
70	13	12.35

Immiscible CO_2 injection

The immiscible flooding process occurs when the reservoir pressure is below the MMP. This results in the case that CO_2 is not able to form a single phase with the oil and with that, remain immiscible [56, 39, 64]. However, solubility will likewise arise in immiscible injection, only with the difference that the interfacial tension between oil and CO_2 during miscible injection becomes zero [33]. With this dissolution of CO_2, the oil volume is set to increase in size (oil swelling). The swelling will facilitate the oil to overcome some of the unfavourable characteristics associated with CO_2 given at Figure 2.7a and relatively improve the sweeping efficiency and oil recovery. This is achieved by reducing the viscosity, increase the relative permeability and an increase in oil volume [9, 39, 56, 33]. Both the reduction viscosity and the elevation of the relative permeability of the oil phase result in a decreased mobility ratio (Equation 2.1).

The solubility of CO_2 is in principle depended on the temperature, saturation pressure and oil API gravity. With increasing pressure and API gravity, the solubility increases. On the other hand, the solubility is antithetical depended on increased temperatures. The study of Emera and Sarma(2006)[8] presents a correlation, based on a generic algorithm, to estimate oil solubility, swelling factor and viscosity reduction. The correlations are molecular weight of the oil, temperature, pressure and API gravity. The correlations are presented below with oil solubility in Equation 2.2, swelling factor in Equation 2.4 and viscosity reduction in Equation 2.6. Despite this improvement of sweeping efficiency, miscible displacement and recovery of oil will remain more efficient than the immiscible flooding process.

$$Sol(molefraction) = 2.238 - 0.33y + 3.235y^{0.6474} - 4.8y^{0.25656} \tag{2.2}$$

, where

$$y = \gamma(0.006897 \cdot \frac{(1.8T + 32)^{0.8}}{P_s})^{\frac{1}{MW}} \tag{2.3}$$

$$SF = 1 + 0.48411Y - 0.9928Y^2 + 1.6019Y^3 - 1.2773Y^4 + 0.48267Y^5 - 0.06671Y^6 \tag{2.4}$$

, where

$$Y = 1000.0 \cdot \left[(\frac{\gamma}{MW} \cdot Sol^2)^{\exp(\frac{\gamma}{MW})}\right] \tag{2.5}$$

$$\eta = y\eta_i + A(\frac{Sol}{\eta_i}) \tag{2.6}$$

, where

$$y = x^B \tag{2.7}$$

$$x = \left[C \cdot \eta_i(\frac{P_s}{1.8T + 32}^D\right]^{\gamma \cdot Sol} \tag{2.8}$$

2.2.3. CO_2 and water interaction

Besides oil, reservoirs contain formation water with which the CO_2 will interact. Under reservoir conditions, CO_2 and water are immiscible fluids, generally resulting in CO_2 floating on top of the aqueous phase by differences in density between the fluids. At the fluid contact however, dissolution of CO_2 into water occurs [18]. Given in Figure 2.8, the solubility of CO_2 is presented as a function of pressure and temperature and pressure and salinity. With increasing pressure, CO_2 has an increasing solubility in water, with the antithetical effect seen with increasing temperature and salinity [34].

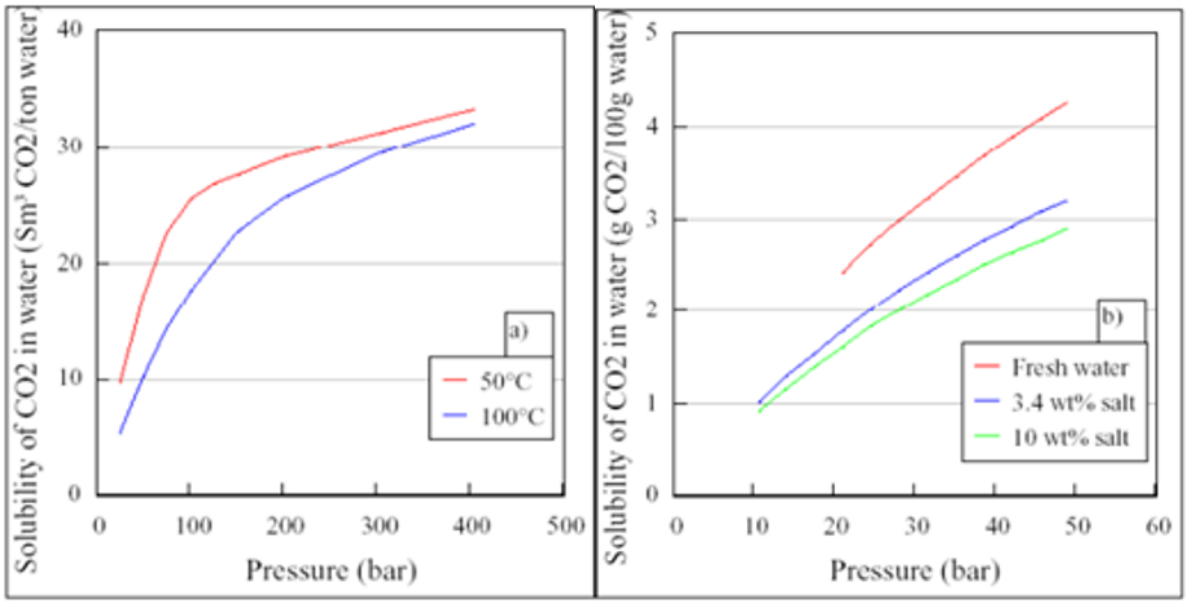

(a) (b)

Figure 2.8: CO_2 solubility in water as a function of (a) pressure and temperature and (b) pressure and salinity. [34]

When CO_2 is dissolved in water, depending on the length of time, it will undergo the following chemical reactions:

$$CO_2(g) \rightleftharpoons CO_2(aq) \tag{2.9}$$

$$CO_2(aq) + H_2O \rightleftharpoons H_2CO_3 \tag{2.10}$$

$$H_2CO_3 \rightleftharpoons H^+ + HCO_3^- \tag{2.11}$$

$$HCO_3^- \rightleftharpoons H^+ + CO_3^- \tag{2.12}$$

$$Ca_2^+ + CO_3^{2-} \rightleftharpoons CaCO_2(aq) \tag{2.13}$$

$$CaCO_3(aq) \rightleftharpoons CaCO_3(s) \tag{2.14}$$

Equation 2.9 refers to the dissolution of the gaseous CO_2 phase in to the aqueous state, continuing to react with water in order to form carbonic acid (Equation 2.10). From this carbonic acid, hydrogen ions will dissociate and produce bicarbonate (Equation 2.11). Continuing with the reaction in Equation 2.12, another hydrogen ion will dissociate and give a carbonate ion. These hydrogen ions will lower the pH of the solvent. The carbonate can react with available calcium cations to form calcium carbonate (Equation 2.13), which in its turn can precipitate from the solution (Equation 2.14) [38].

CO_2 in combination with water is also prone to have chemical interactions with certain rock formations, which can affect the petrophysical properties of the reservoir [14]. With the injection into carbonate rocks, the dissolution of CO_2 in water leads to the dissolution of carbonate minerals by the acidic nature of the CO_2 water solution. With the presence of $CaCO_3$, $MgCO_3$ and $FeCO_3$ in the carbonate rock, water-soluble bicarbonates might form following:

$$CO_2(aq) + H_2O + CaCO_3 \rightleftharpoons Ca(HCO_3)_2 \tag{2.15}$$

$$CO_2(aq) + H_2O + MgCO_3 \rightleftharpoons Mg(HCO_3)_2 \tag{2.16}$$

$$CO_2(aq) + H_2O + FeCO_3 \rightleftharpoons Fe(HCO_3)_2 \tag{2.17}$$

This dissolution of the minerals from the carbonate rock will initially lead to a reduction of permeability, which can be restored when precipitation of these solved minerals comes to pass. The injection of CO_2 with the interaction of formation water in sandstone rocks can induce a reduction in permeability by the dissolution of cementing fragments and subsequently precipitation. When these discharged fragment sizes are smaller than the pore throats, they may become lodged and decrease permeability [14]. In the presence of silicates, Ca_2^+, Fe_2^+ and Mg_2^+ in the solution combined with bicarbonate (from carbonic acid, see Equation 2.11), the solid minerals magnesite, calcite, siderite and silica form [14].

2.3. Polymer assisted water alternating gas (PA-WAG) enhanced oil recovery

In EOR, two main factors dominate the flooding process, acting synchronously in the reservoir while recovering oil: mobility ratio and capillary number. By increasing the capillary number or decreasing the mobility ratio, the efficiency of the overall displacement of the oil during recovery can be increased [24]. When achieving a miscible displacement process (see section subsection 2.2.2), the capillary number becomes infinite, while the residual oil saturation of the flooded area can reach almost zero with a favourable mobility ratio. The performance of the different flooding procedures (e.g. water, gas, polymer, etc.), is exceedingly dependent on both the microscopic displacement and macroscopic displacement efficiencies. While the two displacement efficiencies are associated with the oil that is produced from the pore spaces via the injected fluid, the volumetric sweep efficiency coincides to the amount of oil that is produced by being in contact with the injection fluid. For a total oil recovery efficiency, one had to combine both the displacement efficiency and the volumetric efficiency [1].

While CO_2 had a two to three times higher viscosity compared to e.g. nitrogen, methane of flue gas at the same pressure and temperature, the viscosity of CO_2 relative to oil is still low and likewise the density [54, 28]. Due to the considerable difference in both density and viscosity relative to oil, the injection of CO_2 displays rather poor sweep efficiencies which negatively impacts the total oil recovery, mostly due to unfavorable mobility ratio. This leads to fluid front instability called viscous fingering, gravity segregation, and resulting from that early breakthrough at the outlet (see Figure 2.7a) [1, 28, 54, 33, 15]. The heterogeneities in a reservoir aggravate these sweeping problems, as CO_2 is prone to flow through the higher permeability channels and fractures, reaching the producing well untimely [54, 1]. Once breakthrough of CO_2 has appeared at the production well, a major part of the injected CO_2 will travel straight from the injector to the producer via the higher permeability fluid pathways, bypassing the oil saturated low permeability zones and limiting the oil recovery. This decreased sweep efficiency the is the main complication of CO_2 flooding for EOR. A hybrid injection plan in order to control the mobility ratio of the injected CO_2 is needed to increase the incremental oil recovery [54].

2.3.1. WAG

WAG, or water alternating gas, is an EOR process that combines the principles of conventional water and gas flooding in cyclic injection schemes in order to increase oil recovery [1, 33]. Used extensively in the field, WAG has the main role to increase the water saturation in the reservoir, thereby decreasing the relative permeability to CO_2 [33, 54, 1]. The process gives a better mobility control of CO_2, with the potential to reduce viscous fingering, early breakthrough and increase sweep efficiency [33, 32]. With now the denser water compared to CO_2, the vertical sweep efficiency is largely improved by displacing oil, with especially the basement oil from the bottom of the reservoir being displaced which potentially had been bypassed by solely CO_2 injection [1]. The WAG injection and its sweeping process is illustrated in Figure 2.9a:

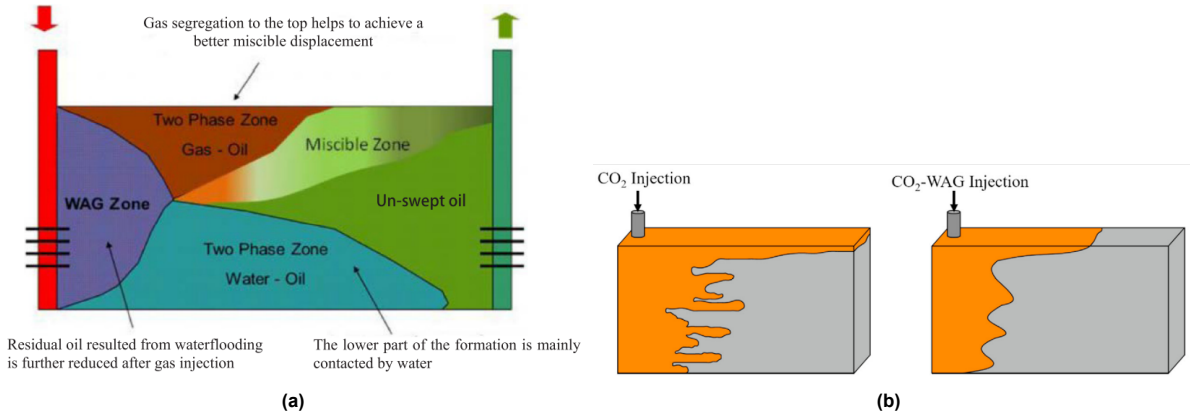

Figure 2.9: (a) Overview of the WAG flooding process along the reservoir. Gravity segregation takes places with CO_2 on top of the oil and water below. The CO_2 develops a miscible zone, allowing better displacement of the oil. The mid section of oil in the second half of the reservoir towards the producing well remains mostly untouched [1]. (b) Comparison of CO_2 flooding and WAG flooding. The WAG process decreases the viscous fingering effect and slightly reduces the gravity override of CO_2 [33].

The WAG process was introduced in EOR to enhance mainly the macroscopic sweep efficiency. The denser and more viscous water allows for an increase in macroscopic efficiency, while the less dense and viscous CO_2 improves the microscopic sweep efficiency. Further, the water injection increases reservoir pressures to levels above the MMP, establishing an increased mobility control by creating a miscible environment for CO_2 (see section subsection 2.2.2). With core flooding experiment executed by Massarweh and Abushaikha (2021)[33], the relative increase in oil recovery between waterflooding, CO_2 flooding and WAG is examined. The results can be seen in Figure 2.10, with WAG clearly achieving the highest recovery:

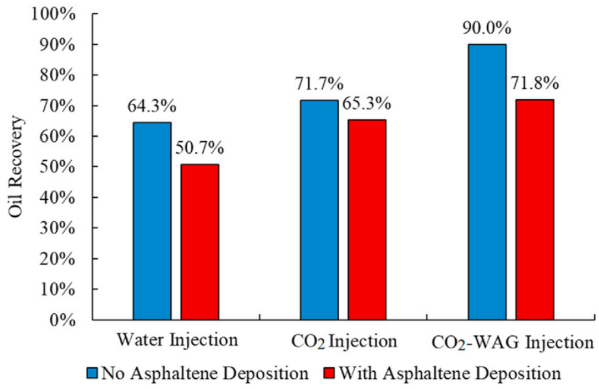

Figure 2.10: The increase in recovery comparing water flooding, CO_2 flooding and WAG [33].

The WAG process has proven in experiments and in the field to effectively increase the oil recovery, while reducing the uses of CO_2 gas during the EOR process [33]. However, the WAG process does not prevent the gravity segregation process, leaving a significant region of the reservoir relatively un-

touched. This happens especially in reservoirs with high permeability zones or fractures, still resulting in early breakthrough of both CO_2 and water. To overcome this complication and even further improve the sweep efficiency and recovery, a new technique called polymer assisted water alternating gas (PA-WAG) is being introduced to the field [32, 24, 30, 63, 64].

2.3.2. PA-WAG

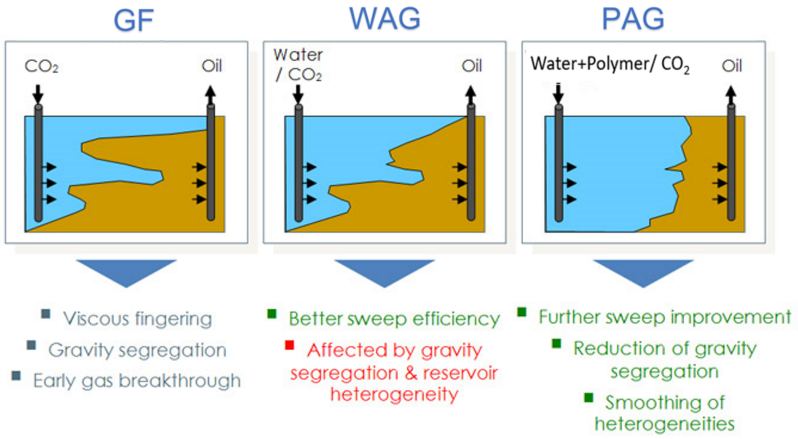

Figure 2.11: Schematic representation of the flooding front of gas flooding, WAG and PA-WAG. Altered from Sajad, Alexander, and Barron (2020)[45].

The PA-WAG method combines the features of miscible or immiscible CO_2 flooding with polymer flooding, resulting in a chemically enhanced WAG flood. Coupling the solubility of CO_2 injection with the effective mobility control of polymer solutions provides better microscopic and macroscopic sweep efficiencies and reduces gravity segregation that troubles both WAG and gas flooding while decreasing the use of polymers compared to polymer flooding [30, 32, 64, 63]. Figure 2.11 visualises the increased mobility control and stabilised front using PA-WAG compared to gas and WAG flooding.

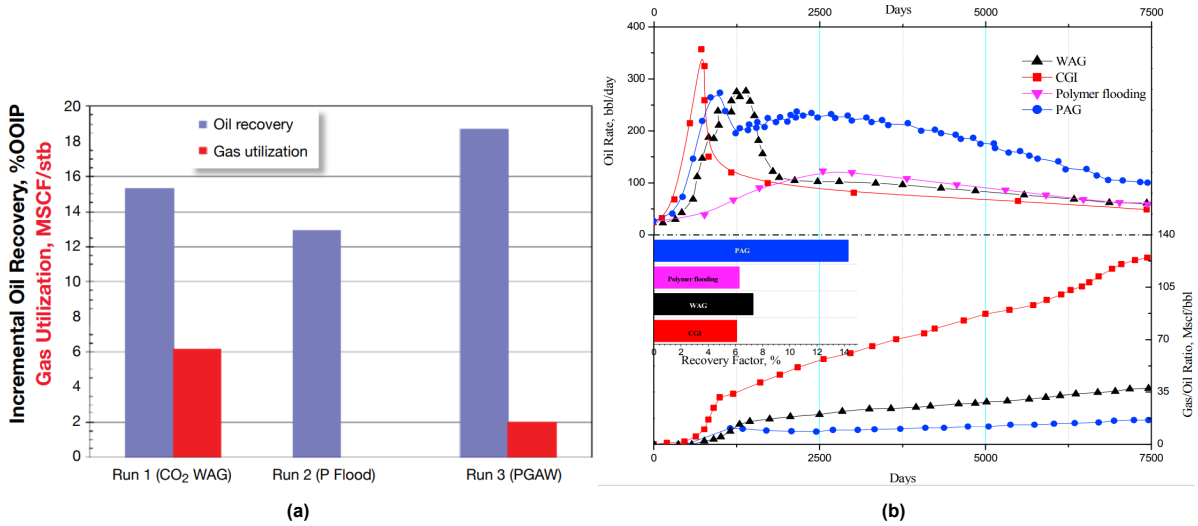

Figure 2.12: (a) Sand-pack core-flood results of the different EOR techniques WAG, PF and PA-WAG, comparing additional oil recovery as a percentage of the original oil in place (OIIP) [64]. (b) Oil rate, recovery factor and water cut modelled for PA-WAG, WAG, polymer flooding and CGI [32, 24].

Figure 2.11 shows two works of comparing different EOR techniques and their performance. In both, the PA-WAG method can be found with superior performance over WAG, PF and continuous gas injection

(CGI). The high CO_2 utilization with the WAG method in the left graph points to a small-scale fraction of the reservoir that has been contacted by the CO_2, illustrating the relatively lower sweep efficiency of the WAG process. The PA-WAG process shows a great improvement in sweep efficiency by using polymer in the solution to create a far more favourable mobility control. The process also required three times less CO_2 to be injected, while increasing the recovery factor by almost 5% [64].

The right image indicates the results of an extensive modelling study comparing the usages of PA-WAG with WAG, PF and CGI. The gas/oil ratio of the PA-WAG is visible to be considerably low and almost constant over the duration of the time of the experiment, which results in higher oil rate than the other methods. The performance of CGI and WAG are considerably lower than the PA-WAG method, mainly due to the issues with gas breakthrough and gravity override those methods are facing.

2.3.3. SAV-10 XV

For the use of polymers in PA-WAG EOR, the polymer is aimed to have a higher temperature and/or salt tolerance, as reservoir have characteristically both. These modified polymers are typically obtained by either hydrophobic modifications to conventional polymers or by incorporating monomers with a temperature and salt tolerance [37]. SAV-10 XV, which is used during this study (provided by the sponsor of this study SNF Floeger), has an incorporation of AMPS (2-acrylamido-2-methyl propane sulfonic acid, or also called ATBS: acrylomido tertiary butyl sulfonate) to the HPAM backbone. This addition increases the tolerance of the hydrolysed polyacrylamide to elevated levels of salinity, hardness and temperature [37, 23].

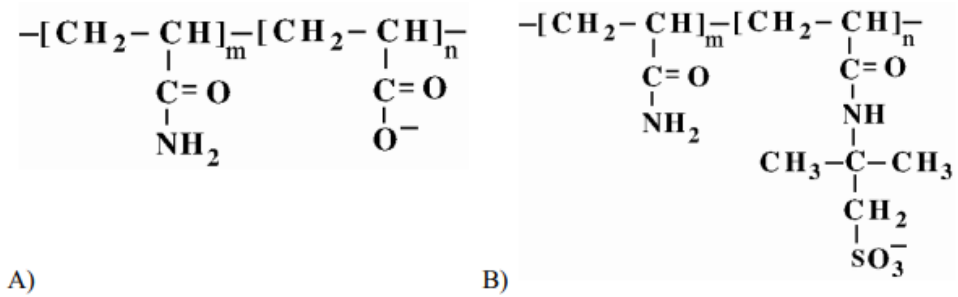

Figure 2.13: Molecule structure of (A) HPAM and (B) HPAM modified with a AMPS. [43]

Jouenne (2020)[23], conducted a study in order to evaluate the tolerance of HPAM modified polymer with AMPS/ATBS, namely SAV-10 (SAV-10 XV has an higher molecular weight). For salinity or hardness, that study found that SAV-10 still obeys the flexible coil behaviour when applying increasing shear rates (see Figure 2.14a). At the temperature range of 25°C-75°, the intrinsic viscosity behaves almost constant, with a similar trend until +120°C expected. For the SAV-10 polymer, the constant intrinsic viscosity with temperature gives a constant relative viscosity with temperature, whatever the salinity and hardness [23]. This is related to the difference in intensity of the interaction with divalent cation Ca^{2+}, with a strong interaction for HPAM between carboxylate and Ca^{2+} (see section 2.1.1) and a less strong interaction with sulfonate for SAV-10. This enforced interaction with divalent cations also results in an increase in the cloud point, which decreases the level of precipitation.

The modified SAV-10 polymer shows insensitivity and quasi constant to whatever pH (in salinity of seawater). AMPS in the polymer molecule stays dissociated when the pH decreases, due to the presence the strong sulfonic acid. This gives that the polymer SAV-10 can tolerate the pH associated to waters in which CO_2 is dissolved.

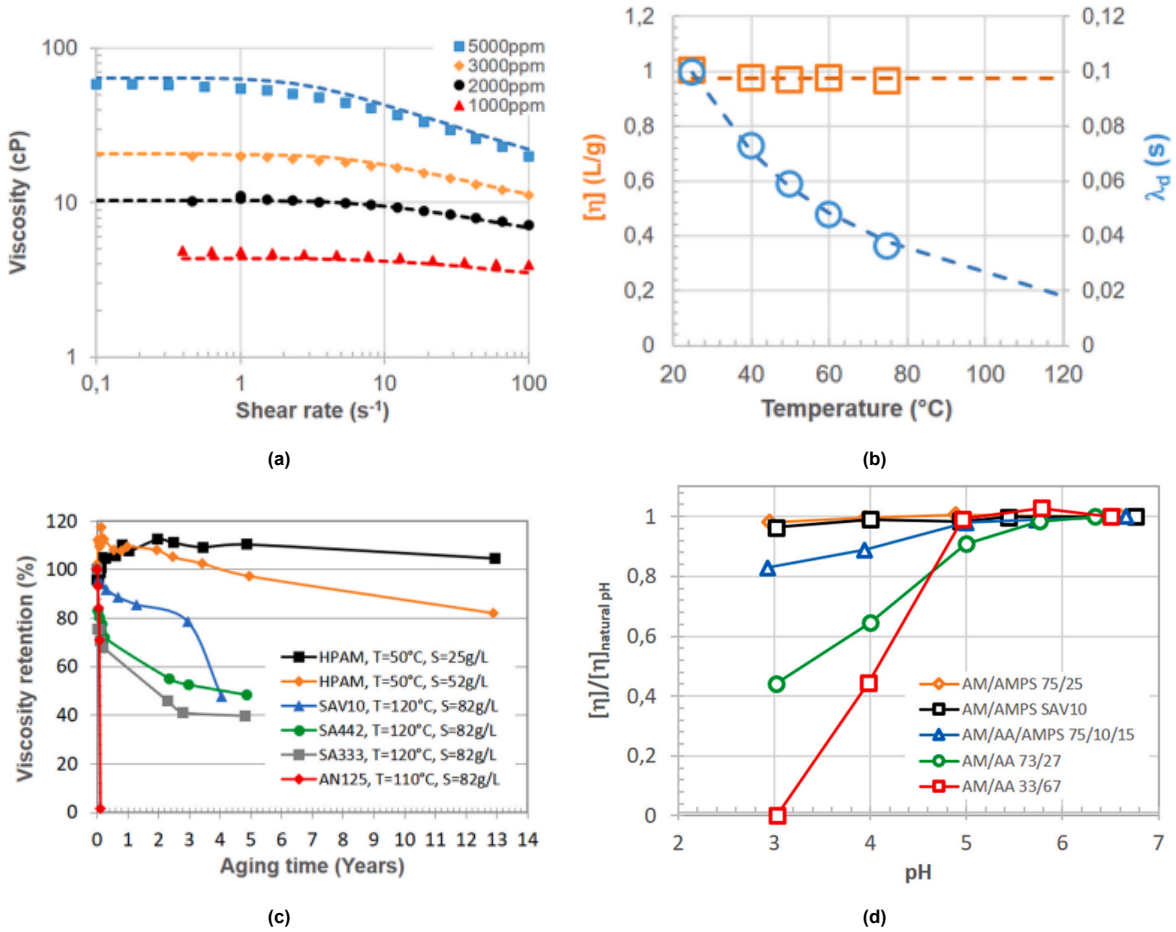

Figure 2.14: (a) Experimental derived viscosity-shear rate dependency of SAV at 25°C and 3543 ppm for the solution and 290 g/L brine. (b) Intrinsic viscosity (orange squares) and relaxation time (blue circles) for the range of temperatures of 25°C-75°C and 3543 ppm for the solution and 290 g/L brine. (c) Long term aging at 120°C of SAV-10 solution. Noticed is that SAV-10 retains 80% of its viscosity after 3 years, after which a sharp decrease occurs. (d) Ratio evolution with pH (addition of HCl) of the intrinsic viscosity of the solution with the original intrinsic viscosity at neutral pH, with varying composition at 2000 ppm for the solution, 25°C and 44 g/L brine (seawater). [23]

2.3.4. CO_2 with polymer behaviour

In PA-WAG, both polymer and CO_2 are used. Mutual behaviour between these two phases needs to be addressed to properly assess and estimate the PA-WAG performance.

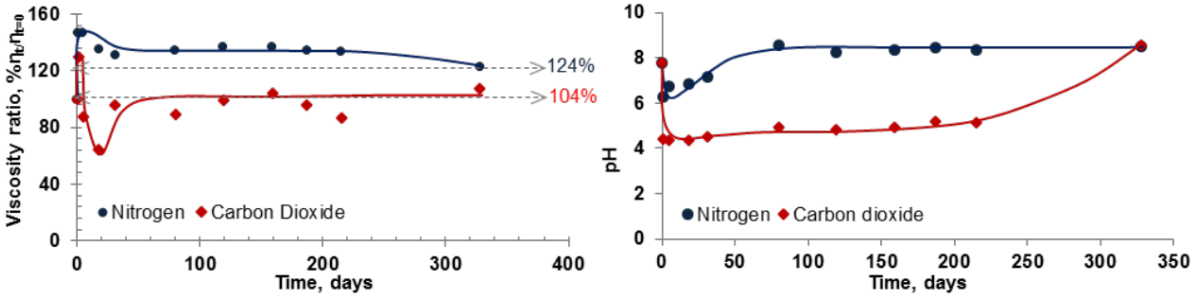

Figure 2.15: The viscosity retention and pH against time for a polyacrylamide ATBS hybrid, aged in both the presence of CO_2 and nitrogen at a temperature of 50°C and a shear rate of $20\frac{1}{s}$ [54].

In Figure 2.15, from the aging test of Tovar, Barrufet, and Schechter (2014) [54] in CO_2 of the PAM-ATBS polymer, a sharp increase in viscosity of 30% can be seen in the first days. After that, the formation of carbonic acid by the reaction of water with CO_2 (equations (2.9) and (2.11)) leads to both a decrease

in pH and viscosity. After 50 days, the viscosity recovered and stabilised at 104% of its initial viscosity. The low pH conditions developed in the early stages of aging promoted by carbonic acid in the solution increase the velocity of the hydrolysis reaction, which presumably causes the recovery of the viscosity [54].

In the study of Tovar, Barrufet, and Schechter (2014) [54], the aging performance of the PAM-ATBS polymer solution can be labelled excellent under the presence of CO_2, with stabilised retention of 104%, even it is around 20% beneath the retained viscosity in the presence of nitrogen gas. CO_2 usage for the PA-WAG process remains preferred over nitrogen, due to its higher viscosity and density.

The first decrease in viscosity during aging at reservoir conditions in CO_2 is important to note as it can have detrimental effects regarding sweep efficiency in that time period of flooding. In order to overcome this, polymer concentration could be increased for viscosity concentration [54].

Besides the effects on viscosity and pH, the combination of polymer with CO_2 is expected to reduce the harshness of corrosion, while likewise preventing oil trapping ensuing from the increased water saturation [33].

3
Materials and Methods

3.1. Chemicals

Table 3.1 presents the physical properties of the various chemical components used during the total of this MSc thesis. For visualization purposes, oleic phase n-hexadecane, was doped with Oil Red O, a red colorant. The Shell-brine composition salts were dissolved in demineralized water for the preparation of the synthetic brine. This composition can be found in Table 3.3 [22]. To perform immiscible gas flooding, WAG and PA-WAG core-flood experiments, carbon dioxide was used. The oleic phase in all experiments (n-hexadecane and crude oil) were doped with 20 wt% 1-iododecane, after extensive dopant analysis based of the study of Janssen, Azimi, and Zitha (2018) [21] (see Appendix B), for enhancing the CT contrast (see subsection 3.5.4 for CT processing information). The physical properties of this doped oleic phase, along with the brine and polymer solution utilized throughout the core-flood experiments are presented in Table 3.2.

Table 3.1: Physical properties of the chemicals. All densities and viscosities mentioned are at 20 °C and atmospheric pressure.

Chemical	Formula	Molecular weight (g/mol)	Density (g/cm3)	Viscosity (mPa·s)	Supplier	Purity
n-hexadecane	$CH_3(CH_2)_{14}CH_3$	226.45	0.775± 0.001	3.37±0.06	Merck	≥99
Oil Red O	$C_{26}H_{24}N_4O$	408.49	-	-	Sigma-Aldrich	≥75
1-iododecane	$CH_3(CH_2)_9I$	268.18	1.257±0.001	-	Sigma-Aldrich	≥ 99
Carbon dioxide	CO_2	44.01	$1.839 \pm 0.001 * 10^-3$	$1.46 \pm 0.5 * 10^-2$	-	100
Crude oil	-	-	-	-	Shell	100
SAV-10XV	-	-	-	-	SNF FLoeger	100
1,3-Diethyl-2-thiourea	$C_5H_{12}N_2S$	132.23	0.989	-	TGI	>97.0%

Table 3.2: Aqueous and oleic phase properties. All densities and viscosities are at 40 °C and atmospheric pressure. The viscosity of the polymer solution, due to the shear thinning behaviour of polymers under shear, is given at the apparent shear rate of the core-flood injection of 15 $\frac{1}{s}$ for the injection at 0.5 cm^3/min (exp. 1 to 3) and at 60 $\frac{1}{s}$ for the injection at 2 cm^3/min (PA-WAG injection). The effective shear rate in porous media is determined with the Blake-Kozeny or Cannella equation [5] and scales linearly with the superficial velocity.

Used fluid type	Density (g/cm^3	Viscosity (cP)
Shell brine	1.0184 ± 0.001	0.75 ± 0.02
Polymer solution 2000 ppm SAV-10XV (15 $\frac{1}{s}$)	1.0256 ± 0.001	11.4 ± 0.2
Polymer solution 2000 ppm SAV-10XV (60 $\frac{1}{s}$)	1.0256 ± 0.001	6.3 ± 0.2
n-hexadecane <0.0006 wt% Oil Red O 20 wt% 1-iododecane	0.8297 ± 0.001	2.26 ± 0.02
Crude oil 20 wt% 1-iododecane	0.9075 ± 0.001	6.96 ± 0.03

Table 3.3: The components used to make the synthetic brine with their concentrations [22].

Salt type	Concentration (g/L)
NaCl	24.501
KCl	0.673
$MgCl_2 \cdot 6H_2O$	10.150
$CaCl_2 \cdot 2H_2O$	1.449
$SrCl_2 \cdot 6H_2O$	0.015
$Na_2SO_4 \cdot 2H_2O$	8.717
$NaHCO_3$	0.328

3.2. Core samples

For most core-flood experiments in this study, where n-hexadecane is used as the oleic phase, well-characterized Bentheimer sandstone was used as a model reservoir. Bentheimer sandstone cores have high permeabilities (2.6 $\pm$ 1.2 Darcy) and a fairly homogeneous mineralogy (>91 wt% quartz) [41]. For the core-flood where crude oil is used as the oleic phase, Indiana limestone is used. Indiana limestone consists almost entirely out of calcite (> 98 wt% $CaCO_3$) [13] and in literature the porosity varies between 12 $\pm$ 2 in the study of Freire-Gormaly et al. (2015) [13] to 15.4 to 18.1 in the work of Meng et al. 2019) [36]. Indiana limestone shows much higher grades of heterogeneity and have a range of relatively low permeabilities compared to Bentheimer sandstone.

From either the Bentheimer or Indiana block, 40.00 cm length cores are drilled, with a diameter of 3.90 cm. After drying in the oven at 60 °C for 48 hours, the samples are first lubricated with a thin layer of epoxy resin grey glue, after which they are glued in a mall with a thicker layer of the same epoxy resin grey glue to withstand temperatures up to 90 °C (dried in both cases for 48 hours before any next step). The glue resin penetrates approximately 1.00 mm radially into the core, reducing its effective diameter to 3.80 $\pm$ 0.10 cm. The cores are then cut with a high precision diamond saw to the appropriate experimental length of 17.00 $\pm$ 0.10 cm and dried again. In order to measure the pressure drop values along the core, holes are drilled through the glue layer. The porosity is determined by CT scans (see subsection 3.5.4) and with the use of available literature [41]. The permeability of the core is determined at full brine saturation of the core. By applying different flow rates, recording the pressure drop along the core and with the knowledge of the brine viscosity at the reservoir temperature, the Darcy's law can be implemented for the permeability [6]:

$$Q = \frac{-kA\Delta P}{\eta L} \tag{3.1}$$

,where Q is the total discharge, k the Darcy's permeability, A the cross-sectional area of flow, ΔP the total pressure drop, η the viscosity of fluid and L the total length over which the pressure drop ΔP takes place.

The properties of the cores used in this study for the totality of experiments are presented in Table 3.4.

Table 3.4: Properties of the cores used throughout this study. PF = polymer flooding, rep. = repetition, CO_2 = CO_2 flooding, WAG = water alternating gas, PA-WAG = polymer assisted water alternating gas and ...+... indicates that the later injection modes comes after the former.

	Experiment					
	1	2	3	4	5	6
Injection scheme	PF + CO_2	PF + CO_2 (rep.)	CO_2 + PF	WAG	PA-WAG	PA-WAG
Rock type	Bentheimer	Bentheimer	Bentheimer	Bentheimer	Bentheimer	Indiana limestone
Porosity (%)	22.4 $\pm$ 0.10	23.1 $\pm$ 0.10	21.6 $\pm$ 0.10	21.6 $\pm$ 0.10	21.9 $\pm$ 0.10	18.7 $\pm$ 0.10
Permeability (Dacry)	2.31 $\pm$ 0.09	1.85 $\pm$ 0.07	2.69 $\pm$ 0.10	2.67 $\pm$ 0.10	2.66 $\pm$ 0.10	0.24 $\pm$ 0.009
Length (cm)	17.00 $\pm$ 0.10	17.00 $\pm$ 0.10	17.00 $\pm$ 0.10	17.00 $\pm$ 0.10	17.00 $\pm$ 0.10	17.00 $\pm$ 0.10
Diameter (cm)	3.80 $\pm$ 0.10	3.80 $\pm$ 0.10	3.80 $\pm$ 0.10	3.80 $\pm$ 0.10	3.80 $\pm$ 0.10	3.80 $\pm$ 0.10
Pore volume (cm^3)	43.21 $\pm$ 1.17	44.24 $\pm$ 1.20	41.60 $\pm$ 1.20	41.65 $\pm$ 1.23	42.22 $\pm$ 1.24	36.14 $\pm$ 1.10

3.3. Capillary viscometer

3.3.1. Experimental set-up

For evaluating the stability of the polymer over time when exposed to CO_2, the set-up from Figure 3.1 was designed. The set-up consists of a glass capillary tube with an inner diameter of 0.4 mm, an outer diameter of 7.5 mm and a length 12 cm, that is placed in a aluminium holder frame. In line, a transfer vessel is placed, in which the polymer solution will be mixed with CO_2 before being injected in the capillary tube. This transfer vessel is driven by a dual-cylinder liquid pump (Quizix QX-6000) with tab water. Below the transfer vessel, a magnetic stirring pad is placed to be able to stir the polymer solution inside the transfer vessel. A back pressure regulator (DEMO-TU Delft), couple with a nitrogen cylinder (200 bar), will be connected to the end of the capillary to control the outlet pressure of the system during the experiment at 15 bars. The CO_2 will be supplied to the system from a cylinder (200 bar). At the beginning and the end of the capillary, absolute pressure transducers are placed to monitor the P_{in} and P_{out} (20 bar), as well as a differential pressure transducer (+- 500 mbar) over the capillary. Behind the absolute pressure transducer monitoring P_{out} , a pH meter is placed to also monitor the pH during the experiment (maximum of 17 bar). A sampling tube is connected to the outlet tubing to collect the effluent. All the lines are made of steal, except from the backpressure to the waste collector. The whole set-up is placed in an oven to keep the temperature during the experiment constant at the desired experimental operating temperature of 40 °C.

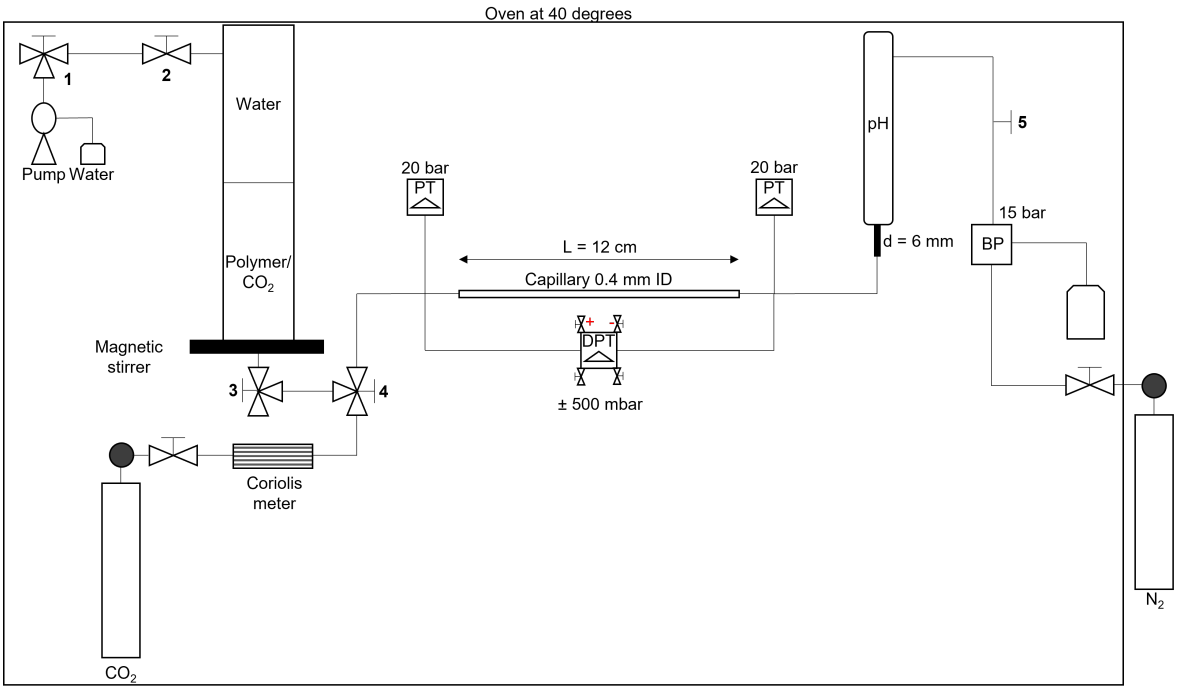

Figure 3.1: Schematic representation of the polymer aging in the presence of CO_2 experiment. PT = pressure transducer. DPT = differential pressure transducer.

3.3.2. Experimental procedure

To test the stability of the polymer solution properly when exposed to CO_2, an oxygen free environment is ensured when creating the polymer solution, by stirring the polymer inside of a glove box filled with nitrogen and the addition of the oxygen scavenger 1,3-Diethyl-2-thiourea at a concentration of 200 ppm. The desired volume for the polymer solution is 1.3 L (maximum of the transfer vessel is 2 L), which allows for testing over a month time at a flow rate of 0.03 cm^3/min and have a large enough volume of water at the other end of the transfer vessel to allow for retraction of the piston when injecting the amount of CO_2 that can dissolve in the polymer solution. This dissolve-able amount of CO_2 is retrieved from literature about the CO_2 solubility in seawater [7]. The work from Duan et al. (2006) [7] states the maximum volume of CO_2 that can dissolve in seawater at given pressures and temperatures, which will decrease by increasing temperature and increase by increasing pressure. Figure 3.2 presents the

solubility curve of CO_2 in seawater retrieved from [7].

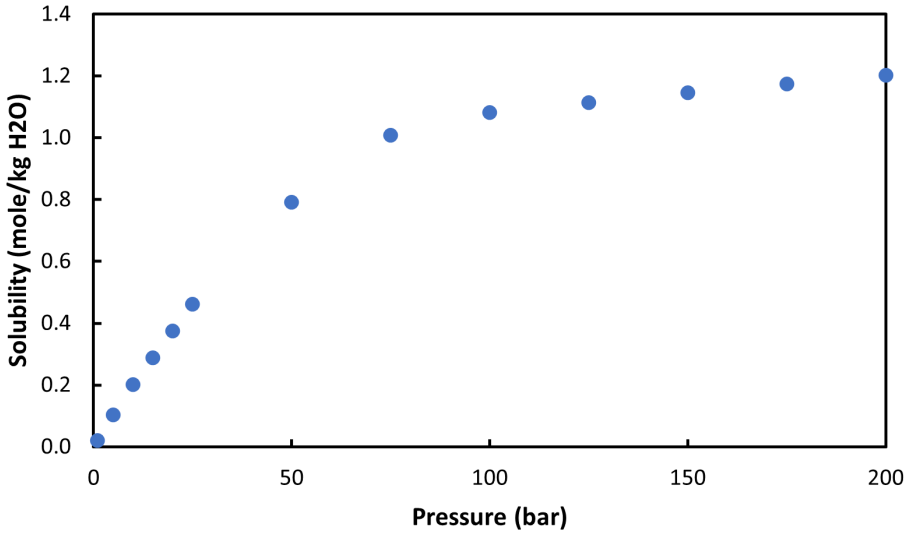

Figure 3.2: The solubility of CO_2 in seawater, given in mole/kg of H_2O, over pressure, at a constant temperature of 40 °C [7].

From this solubility curve, the solubility of CO_2 at 15 bar was retrieved, equivalent to 0.29 mole/kg, which translates to 0.57 L of CO_2 or 16.8 g for our polymer volume of 1.3 L.

Long term stability at full CO_2 saturation

The polymer solution is inserted in the bottom half of the transfer vessel. The pump, connected to valve 2, injects water in the upper half until the polymer is seen at the bottom (valve 3). With the help of the Coriolis meter, the exact amount of CO_2 able to dissolve is injected in the polymer solution from valve 4 (via valve 3 to the transfer vessel). The pump is set on receiving in order to retract the piston within the transfer vessel. After injecting the CO_2, the mixture is left to age for 24 hours before injecting into the capillary ([54]). During this time, the pump is set at a constant pressure delivery just over the experimental pressure of 15 bar to ensure the dissolving of the CO_2 completely in the polymer solution. This constant pressure will ”push down” the CO_2 in the polymer solution by injecting the retracted volume from inserting the CO_2 in the transfer vessel back over the time of aging, forming a control to indicate complete dissolution. Inside the transfer vessel on the polymer CO_2 mixture side, a magnetic stirring rot is placed in advance to stir the mixture during the injection and the whole experiment. The system is subjected to a thorough leak test, injecting helium from valve 4 (CO_2 side), ensuring that the system is leak tight (make sure that valve 5 is also open). Then, a vacuum is applied to the system from the outlet, until stabilisation at around -1 bar in order to remove any gas still remaining in the system. When this is reached, demi water is to be injected into the system to bring the pressure back to atmospheric pressure. Under a slight backpressure, the differential pressure transducer is filled with water, after which the backpressure is increased to 15 bar. With the demi water, the capillary tube diameter can be tested, as well as the pH meter and the offset of the PT’s can be set.

After the system is leak tested with helium and filled with demi water, the injection of the CO_2 - polymer solution can be started from the transfer vessel via valves 3 and 4 to the capillary, with the use of the pump to the top half of the transfer vessel via valves 1 and 2. First, the systems volume of approximately 60 mL is flushed at a flow rate of 3 cm^3/min, to ensure only polymer solution is present in the system when measuring at the desired experimental flow rate of 0.03 cm^3/min. The progression of the polymer solution containing CO_2 can be traced through this flushing firstly by the sudden increase in dP due to the higher viscosity than water, then the decrease in pH from around 7 for water to 4.2 $\pm$ 0.1 for the acidic polymer solution due to the dissolved CO_2 (see subsection 2.2.3) and lastly the bubbling of the CO_2 after the backpressure (due to pressure release, CO_2 will come out of solution).

When the system is flushed with the polymer solution containing CO_2, the sampling tube is installed at the outlet. At a established schedule, the effluent will be analysed through rheology measurements as well, comparing it to the original polymer solution without CO_2, that is kept at the same temperature over the whole experimental time. This will ensure for a clear view on the influence of only CO_2 on the polymer solution over a longer time scale of roughly a months time. All the experimental parameters of relevance can be found in Table 3.5.

During the experiment, differential pressure data is collected over the course of the polymer injection into the capillary. This differential pressure drop over the capillary can be converted into the apparent viscosity of the injected fluid [55]:

$$\eta_A = \frac{\sigma_\omega}{\dot{\gamma}_A} \tag{3.2}$$

, where σ_ω (wall shear stress) and $\dot{\gamma}_A$ (apparent shear rate) are given by:

$$\sigma_\omega = \frac{R}{2}(-\frac{dP}{dz}) \tag{3.3}$$

and

$$\dot{\gamma}_A = \frac{4Q}{\pi R^3} \tag{3.4}$$

Substituting equations (3.3) and (3.4) into Equation 3.2, the apparent viscosity of the fluid at the shear rate of the injection into the capillary is given by:

$$\eta_A = \frac{-dP\pi R^4}{dz8Q} \tag{3.5}$$

Here, dP, R, dz and Q represent the differential pressure over the capillary, radius, length of the capillary and volumetric flow rate, respectively.

Table 3.5: Experimental parameters of the capillary viscometer set-up, testing the stability of the polymer solution when exposed to CO_2. The molar concentrations are at 20 bar and 40 °C.

	Input	Units
Polymer concentration	2000	ppm
Oxygen scavenger concentration	200	ppm
Injection rate polymer flush	3	cm^3/min
Experimental injection rate	0.03	cm^3/min
Backpressure	15	bar
Temperature	40	°C
CO_2 molar concentration (long term)	0.295	mol/L

CO_2 impact on the polymer during PA-WAG injection

The SAV-10XV polymer is subjected to a second test. The first tests was focused on the longer scale stability of the polymer in contact with CO_2, at full saturation levels of dissolved CO_2 in polymer. The second test aims to illustrate the impact of CO_2 on the polymer during the PA-WAG injection, based on mole fractions just after the breakthrough of polymer during the experiment in Bentheimer sandstone. For the mole fraction determination, the brine molecular weight was estimated on the basis of the molecular weight of the individual components and their concentration (see Table 3.3). The molecular weight determination can be seen in Table 3.6. For the molecular weight of the polymer, the average of the range reported by Jouenne (2020) [23], being 21500 g/mol. This results in an estimated molecular weight of the 2000 ppm polymer of 453.7 g/mol. With determined mole fractions during the PA-WAG experiment, the molar concentration to mimic this situation is found to be 0.027 mol/L, which is a factor 11 lower than the fully saturated stability test.

Table 3.6: Molecular weight of every component of the Shell brine and their respective participating percentage in the total molecular weight of the brine, based on their concentrations (see Table 3.3).

	Molecular Weight (g/mol)	%
NaCl	58.44	0.024501
KCl	74.55	0.000673
$MgCl_2 \cdot 6H_2O$	203.3	0.01015
$CaCl_2 \cdot 2H_2O$	147.01	0.001449
$SrCl_2 \cdot 6H_2O$	158.53	0.000015
$Na_2SO_4 \cdot 2H_2O$	322.19	0.008717
$NaHCO_3$	84.01	0.000328
Water	18.02	0.954167
Total	23.79	1

Due to complications in glove bag strength and delivery time, no glove bag was available to prepare the polymer solution in an oxygen free environment. After the mixing of the polymer, the solution was degassed and the oxygen scavenger was added at 200 ppm concentration. The viscosity of the polymer was tested after one day to ensure a stable solution was created with only the oxygen scavenger in terms of viscosity retention. Thereafter, the polymer solution container was degassed to remove any air inside. With vacuum conditions in the container of the polymer solution, the CO_2 is injected into the system. After the amount needed to simulate the PA-WAG conditions is injected, the polymer solution is aged for 24 hours in the presence of the CO_2. To analyse the polymers stability under these conditions, the viscosity is measured with the use of a rheometer after the 24 hours of aging and again three days later. At all times, the polymer solution is kept in the oven at 40 °C.

3.4. Rheological measurements

In order to determine the viscosity and viscosity behaviour under shear rate of the fluids used, rheology measurements are performed with the Anton-Paar rheometer. Over a defined interval of shear rates, the viscosity is measured with the rheometer for mainly the polymer solutions, oil phases and brine used in this study. Then, for the polymer solutions, the data is fitted with the Carreau-Yasuda model to capture the shear-thinning behaviour of the polymer under implied shear rate.

3.4.1. Rheometer

Using the Aton-Paar Rheometer MCR 102, the rheology is measured. The schematic of the set-up of the rheometer, containing the measuring cylinder, isolating cap, measuring cup and fluid sample is presented in Figure 3.3. The fluid sample is inserted into the measuring cup. After loading the sample, the measuring cylinder is lowered until measuring position (gap of 1.000 mm). The measuring set: standard configuration is then selected and initiated for the measurements, with the desired temperature input of 40 °C. The measuring cup is closed off with a isolating cap, ensuring constant temperature over the course of the measurements. Over a desired shear rate interval of 0.01 to 1000 s^{-1}, the measuring cylinder will start apply the shear rate with creating appropriate torque by spinning inside of the measuring cup filled with the sample fluid. During this shear rate interval, the viscosity is measured in cP. This measuring is done over 4 intervals of 0.01 to 1000 s^{-1}, divided into 41 measurements of 5 seconds, which creates a duration of 205 seconds per interval of 0.01 to 1000 s^{-1}. Intervals 1 and 3 are in the order from 0.01 to 1000 s^{-1} and 2 and 4 from 1000 to 0.01 s^{-1}, to achieve a smooth transition from 1 interval to the other. Table 3.7 states the measurements input parameters.

Table 3.7: Measuring input parameters for the Aton-Paar Rheometer MCR 102 in order to carry out the rheology measurements.

Initializing set-up		Data points		Set Value	
Parameter	Input	Parameter	Input	Parameter	Input
Measuring set	standard configuration	Number	41	Profile	Ramp logarithmic
Measuring gap	1.000 mm	Duration	Constant	Initial(1,3)/Final(2,4)	0.01 s^{-1}
Temperature	40 °C	Point	5 s	Final(1,3)/Final(2,4)	1000 s^{-1}

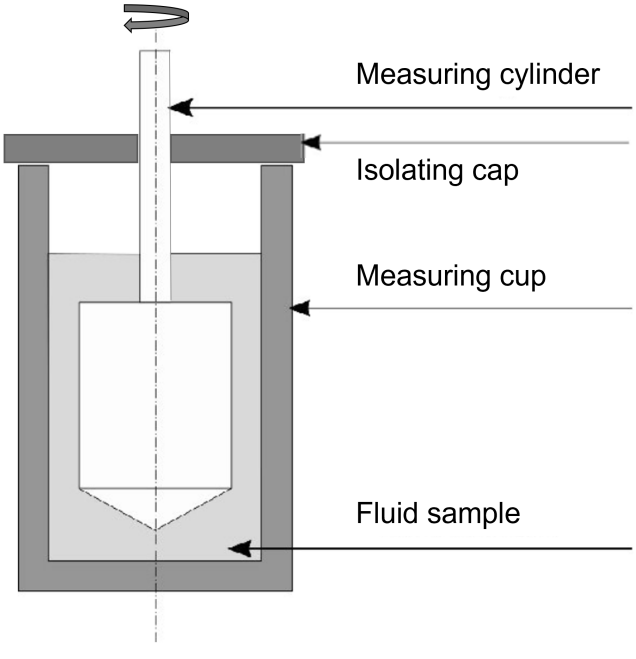

Figure 3.3: Schematic overview of the measuring element of the Aton-Paar Rheometer MCR 102. This schematic is an altered version from Werner (2018) [60].

3.4.2. Bird-Carreau-Yasuda model

The polymer Newtonian plateau followed by the critical shear rate (onset of shear thinning) and shear-thinning behaviour under implied shear rate can be modelled by the Bird-Carreau-Yasuda model [40]. The data retrieved from the rheology measurements with the rheometer are fitted with the Bird-Carreau-Yasuda equation [40]:

$$\eta(\dot{\gamma}) = \eta_{\infty} + (\eta_0 - \eta_{\infty}) \left[1 + (\dot{\gamma}\lambda)^a\right]^{\frac{n-1}{a}} \tag{3.6}$$

, where η, η_{∞}, η_0, $\dot{\gamma}$, λ, a and n are the viscosity, viscosity at infinite shear rate (assumed as solvent viscosity, in this case the brine from Table 3.3), zero shear rate viscosity, the shear rate, relaxation time (know as $\frac{1}{\dot{\gamma}_{crit}}$, where $\dot{\gamma}_{crit}$ is the critical shear rate or shear-thinning onset), width of the transition zone and the Power Law index, respectively.

3.5. Core-flood experiments CT aided

3.5.1. Experimental set-up

The experimental set-up is schematically visualised in Figure 3.4, used for performing the core flood experiments. The set-up uses a dual-cylinder pump (Quizix QX-6000) for injecting the aqueous phases into the core, that is placed into a polyether ether ketone (PEEK) core holder, with a low X-ray attenuation, surrounded by a heating sleeve in order to keep the temperature at the desired level. The core, with the core holder and the heating sleeve are placed in a fixed horizontal position (vertical scanning results in excessive artefacts, giving no meaningful insights. See Appendix C) on the CT bench. The back pressure regulator (DEMO-TU Delft) controls the outlet pressure at 20 bar by using nitrogen. The effluents at the outlet are sampled using a fraction collector at preset time intervals. From a CO_2 supply, carbon dioxide is injected via a mass flow controller (Bronkhorst, EL-FLOW, see Appendix D) into the system. Both the oleic phase in the primary drainage stages as well as the polymer solution used as either secondary or tertiary recovery mode are indirectly injected into the core by the pump by using a transfer vessel. Along the core, 4 pressure transducers are placed to be able to monitor the pressure behaviour during the floods (three for three separate ΔP's and one ΔP_{tot}). To see any temperature fluctuations, a thermocouple is used. The pressures and temperatures are recorded at a preset time interval of 10 seconds using a data acquisition system (National Instruments).

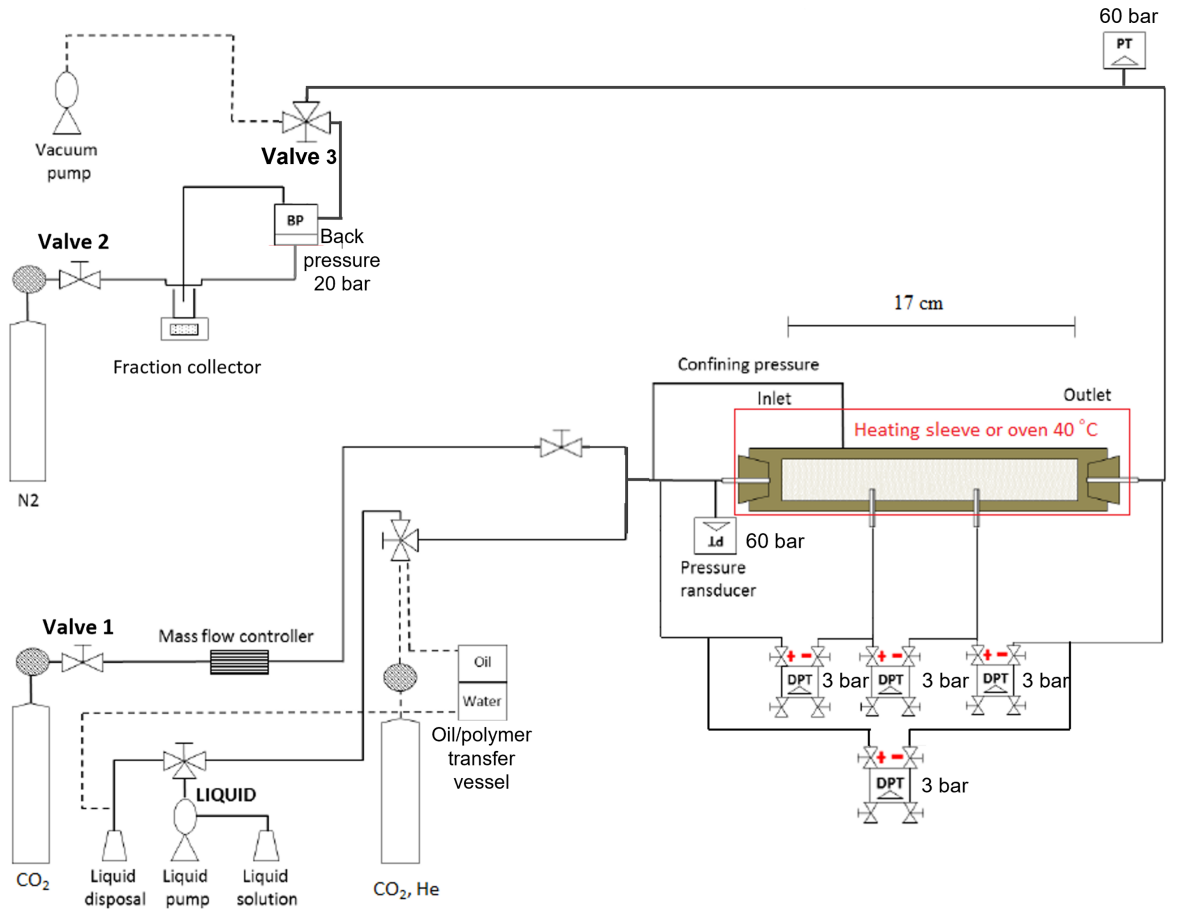

Figure 3.4: Schematic representation of the core-flood experimental set-up. PT = pressure transducer. DPT = differential pressure transducer.

3.5.2. CT scan

During all core-flood experiments, CT scans were taken on specific moments using a Siemens SOMATOM Definition CT scanner with full dual-energy scanning capabilities, which is needed to analyse 3-phase fluid systems and give insights on the phase saturation distribution during the displacement processes. On the bed of the CT scanner, the core is fixed horizontally. The scanner operates using two X-ray tubes simultaneously: 80 kV voltage and 550 mA current and 140 kV voltage and 250 mA current. One single scan consists of 302 slices of each 0.6 mm thick. Every slice contains 512 x 512 pixels with a pixel size of 0.2 x 0.2 mm. The scanning of the core is performed with the spiral scanning mode. Analysis and visualization of the data retrieved from the CT scans is done by the usage of ImageJ and Avizo software.

3.5.3. Experimental procedure

In total, six core-flood experiments were performed, from which five were conducted on Bentheimer sandstone cores and one on a Indiana limestone core. All the experiments were carried out under 40 $\pm$ 1 °C and 20 bar back pressure. In Table 3.8, an overview of the procedure for all 6 experiments is presented.

Table 3.8: Experimental procedure steps followed for all core-floods.

Step	Experiment	Procedure	Back pressure (bar)	Flow rate (cm^3/min)	CT-assisted
1	All	CO_2 flushing	-	-	No
2	All	Vacuuming	-	-	No
3	All	Brine saturation	20	2	No
4	All	Permeability test	20	1.0, 2.0, 3.0, 4.0, 5.0	No
5	All	Oil injection	20	0.5	Yes
6	All	Oil bump flood	20	0.5, 1.25, 2.5	Yes
7	PF + CO_2 (1, 2)	-	20	Polymer: 0.5, CO_2: 0.5	Yes
	CO_2 + PF (3)	-	20	Polymer: 0.5, CO_2: 0.5	Yes
	WAG (4)	-	20	Water: 2, CO_2: 0.5	Yes
	PA-WAG (5, 6)	-	20	Polymer: 2, CO_2: 0.5	Yes

After extensive leak testing, the system was flushed with CO_2 from the central lab system over a time of approximately 30 minutes at a pressure of 5 $\pm$ 0.5 bar in order to remove any air out from the system. Subsequently, a vacuum was applied to remove the remaining carbon dioxide gas. Thereafter, the core was saturated with brine with approximately 10 $\pm$ 0.5 pore volumes, set at a fixed flow rate of 2.00 cm^3/min, while a back pressure of 20 bar was applied. At the last stage of the brine injection, the absolute permeability of the core was measured by varying the flow rate and using Darcy's law (Equation 3.1 [6]).

Primary drainage followed upon brine saturation, initiated by injection of roughly 6 PV of oleic phase at a rate of 0.50 cm^3/min. The end-point relative permeability (k^e_{ro}) is determined by flow rate variations during the last PV injected and utilizing Darcy's law (Equation 3.1 [6]). At the end, conate water saturation (S_{wc}) state is reached in the core and either polymer flooding, CO_2 flooding, WAG or PA-WAG injection can be initiated at initial oil saturation (S_{oi}) level.

In the experiments 1, 2 (see tables 3.4 and 3.8) and 3 (see tables 3.4 and 3.8) polymer and CO_2 flooding were applied as secondary recovery mode, which were both injected at S_{oi} with 5 PV each at a constant back pressure of 20 bar and a flow rate of 0.50 cm^3/min (see Appendix D for the flow rate conversion for CO_2 injection throughout the course of experiments). Afterwards, as a tertiary recovery mode, continuous CO_2 injection followed up on polymer flooding at $S_{or,PF}$ and polymer flooding took place after CO_2 injection at S_{or,CO_2}.

The WAG (experiment 4, see Table 3.4) and PA-WAG (experiment 5 and 6, see Table 3.4) injection schemes were run for a total of 6 cycles, consisting out of an injected polymer or water slug of 0.22 PV followed by a CO_2 slug of 1.3 PV at S_{oi}. The results are analysed concerning recovered volume of oil, pressure date, relative permeabilities and mobility ratios, saturation profiles and CT illustrations of the flow through the core.

3.5.4. CT image processing

The usage of a medical CT scanner (see subsection 3.5.2) allowed for the evaluation and visualization of the phase saturation profile during the in injection and displacement of the various phases. CT scans were taken using both single and dual energies, where the single energy 140 kV was used for the two-phase saturation and dual energy (80 kV and 140 kV) for the three-phase saturation measurements. The CT response from these measurements is described by the amount of Hounsfield units (HU), which are retrieved from the scans by processing the images with the use of ImageJ. These CT responses in HU can be implemented in a series of equations to calculate porosity (Φ), two-phase S_o and S_w, three-phase S_o, S_g and S_w from the study of Sharma, Brigham, and Castanier (1997) [48] and Janssen, Azimi, and Zitha (2018) [21]. Avizo software is used to create a 3D visualization of the displacing fluids throughout the core. For both ImageJ and Avizo, a working process for the measurements and visualization can be found in the Appendix E.

Porosity

The porosity of the used cores throughout the entire study were calculated by using single energy 140 kV data (denoted throughout CT analysis formulas with subscript 1) with the use of the formula:

$$\Phi_1 = \frac{CT_{wet_1} - CT_{dry_1}}{CT_{brine_1} - CT_{air_1}} \tag{3.7}$$

, where Φ, CT_{dry}, CT_{wet}, CT_{air} and CT_{wet} denote respectively the porosity and CT responses in HU for the dry core, brine saturated core, the air phase in bulk and the brine phase in bulk. For the three-phase saturation distribution analysis, 80 kV single energy porosity is required. Equation 3.7 is used in these cases as well implemented with subscript 2 instead of subscript 1.

Two-phase oil and water saturation
Oil and water saturation for the two-phase system were calculated throughout the entire study were calculated by using single energy 140 kV data by the usage of the formulas:

$$S_o = \frac{1}{\Phi_1} \frac{CT_1 - CT_{wet_1}}{CT_{oil_1} - CT_{brine_1}} \tag{3.8}$$

$$S_w = 1 - S_o \tag{3.9}$$

, where S_o, S_w, CT and CT_{oi} represent respectively the oil saturation, water saturation, CT response in HU scanned core at the moment of interest and the CT response of the oleic phase in bulk.

Three-phase oil, gas and water saturation
For the calculations of the saturation distribution in a three-phase system, dual-energy CT data is needed. 140 kV (subscript 1) and 80 kV (subscript 2) CT response data is used throughout the entire study as follows:

$$S_o = \frac{(CT_1 - CT_{wet_1})(CT_{dry_2} - CT_{wet_2}) - (CT_2 - CT_{wet_2})(CT_{dry_1} - CT_{wet_1})}{\Phi_1(CT_{oil_1} - CT_{brine_1})(CT_{dry_2} - CT_{wet_2}) - \Phi_2(CT_{oil_2} - CT_{brine_2})(CT_{dry_1} - CT_{wet_2})} \tag{3.10}$$

$$S_g = \frac{(CT_1 - CT_{wet_1})\Phi_2(CT_{oil_2} - CT_{brine_2}) - (CT_2 - CT_{wet_2})\Phi_1(CT_{oil_1} - CT_{brine_1})}{\Phi_2(CT_{oil_2} - CT_{brine_2})(CT_{dry_1} - CT_{wet_1}) - \Phi_1(CT_{oil_1} - CT_{brine_1})(CT_{dry_2} - CT_{wet_2})} \tag{3.11}$$

$$S_w = 1 - S_o - S_g \tag{3.12}$$

, where S_g denotes the gas saturation.

Table 3.9 gives an overview of the determined HU responses for the several phases in bulk used throughout the equations (3.7), (3.8), (3.10) and (3.11).

Table 3.9: Overview of the HU responses for the phases in bulk for the different core-flood experiment analysis. Measured scanning small samples of the phase in bulk with dual energy.

Phase	140 kV ($_1$) (HU)	std	80 kV ($_2$) (HU)	std
Air	-998	4.1	-1002.7	5.3
Brine	43.4	5.7	70.9	7.8
n-hexadecane <0.0006 wt% Oil Red O 20 wt% 1-iododecane	1107.3	25.8	2514.5	24.1
crude oil 20 wt% 1-iododecane	1403.7	40.1	2975.2	53.7

4

Results and discussion

4.1. The impact of CO_2 dissolution on polymer viscosity

With the capillary viscometer, the impact of CO_2 dissolution on the SAV-10XV polymer solution is analysed. In this section, the results from the capillary set-up are presented in the form of the measured pH, dP and correlated apparent viscosity with the use of Equation 3.5.

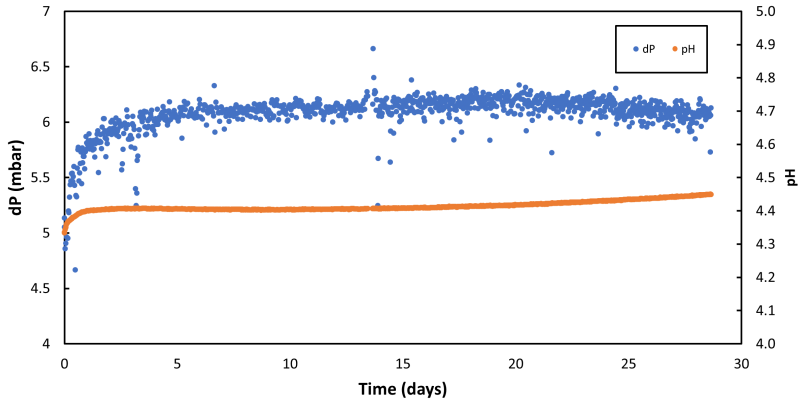

Figure 4.1: The pressure drop over the capillary and the pH of the polymer/CO_2 solution over the course of full injection in 29 days. After the initial drop in dP and pH, presumably due to still a mix of demi water and the polymer/CO_2 solution, both display a reasonably stable trend over the course of 29 days, with a slight increase in pH noticeable starting around day 15 and a decrease in dP starting around day 20 of the injection.

Figure 4.1 presents the measured pH and dP during the injection period of $\pm$ 29 days, after the CO_2 was allowed to dissolve in the polymer solution and reach equilibrium. Both the dP and pH have a slight increase from their initial values at t=0 of 5.05 $\pm$ 0.10 mbar and 4.33 $\pm$ 0.01, respectively. A presumed cause can be found in some left over demi water in the system at the start of injection, which lowers the viscosity of the polymer solution at that time when mixed. This would indicate that the polymer flush at the start of injection was not comprehensive enough. However, the pH should be higher if this is the case. The short term injection, capturing initial impact, should shine more light on the start of injection. Thereafter, the dP and pH stabilize around 6.3 $\pm$ 0.1 mbar and 4.4 $\pm$ 0.01, respectively. Around day 15 for the pH and day 20 for the dP, the trends change and start to slightly increase for the pH and decrease for the dP. The differential pressure transducer was evidently sensitive to the opening of the oven doors, which is mainly done for taking samples at the outlet of the system for rheometer measurements. This led to the larger fluctuations visible in the dP trend presented in Figure 4.1.

With the use of Equation 3.5, the dP measurements are correlated to apparent viscosity of the polymer/CO_2 solution flowing through the capillary. These results are given in Figure 4.2. From the original apparent viscosity of 6.81 $\pm$ 0.1 cP, retrieved from rheometer data at the apparent shear rate of 80 s^{-1} (determined for the capillary with the use of Equation 3.4) of the original solution before CO_2 injection, the apparent viscosity drops initially to a value of 5.29 $\pm$ 0.16 cP and continues with the same trend as the dP displayed (as they are proportional to each other). From the effluent samples that are taken at given times, the viscosity is analysed with the use of the rheometer.

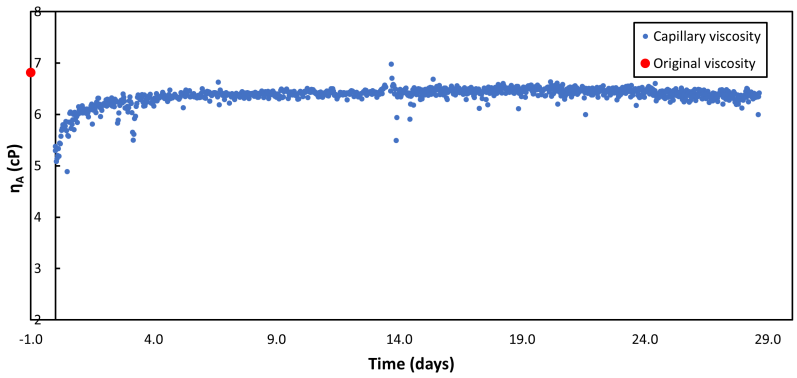

Figure 4.2: The correlated apparent viscosity from the dP presented in Figure 4.1, using Equation 3.5, with the original viscosity at 40 °C (note: from the rheometer, so under atmospheric pressure) at the apparent shear rate of 80 s^{-1}.

4.2. Rheological results

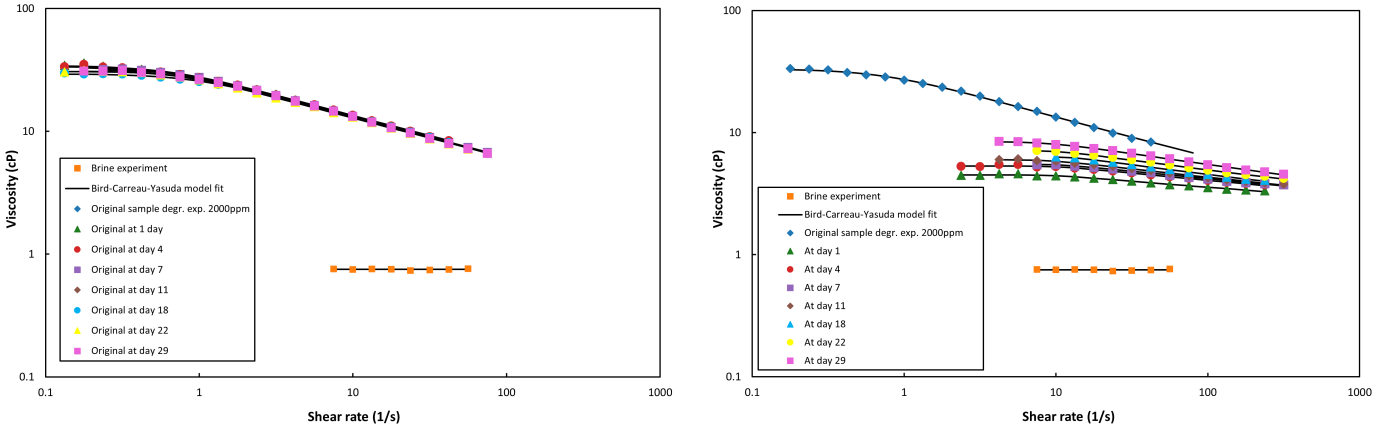

Figure 4.3: Rheometer results for thermal stability test and CO_2 stability test of the SAV-10XV polymer, both with the brine, that functions as solvent, as a reference measurement. (a) Thermal stability of the polymer solution (2000 ppm SAV-10XV) at 40 °C. The rheology over time displays no changes, retaining its viscosity under elevated temperature levels. (b) Stability of the polymer solution (2000 ppm SAV-10XV) with dissolved CO_2 at 40 °C and 20 bar. The polymer shows a decrease in overall viscosity, a lowering of the Newtonian plateau and shear thinning slope and a delay in shear thinning onset. Over time, the viscosity recovers slightly.

Throughout this study, the viscosity of the polymer solutions is analysed with the use of the rheometer, which allows to capture the shear thinning behaviour of the polymer with respect to the shear rate applied. In figures 4.3a and 4.3b, the results from the rheometer measurements of the analysed samples taken at the outlet of the capillary viscometer set-up are presented, along with the samples of the original batch at thermal stable conditions and their corresponding Bird-Carreau-Yasuda model fits. These results are from the stability test done at full CO_2 saturation for a longer aging time of 29 days. Figure 4.3a displays the thermal stability of the SAV-10XV polymer at 40 °C over the course of 29 days. The rheological profile of the polymer solution under shear rate displays no significant changes over that period, indicating a well created oxygen free environment for the polymer solution during the stability test (see Appendix K for comparison) and the viscosity retention capabilities of the polymer under the 40 °C conditions. Figure 4.3b provides the stability of the same polymer solution, only now with the addition of CO_2, over the course the same 29 days. The apparent viscosity of both their baseline original samples are therefore the same. The polymer solution saw, as illustrated in section 4.1, the initial decrease in viscosity after the aging of the polymer with dissolved CO_2. Besides this decrease in overall viscosity, the onset of the shear thinning ($\dot{\gamma}_{crit}$) was delayed from 0.7 s^{-1} of the original solution to 9.6 s^{-1} after 1 day of injection and the shear thinning slope decreased significantly from 1.55 to 1.14

(Power Law indices n of 0.65 and 0.88, respectively). Over the course of the successive days of testing, the viscosity of the polymer solution affected by CO_2 recovers slightly, along with a slightly increasing shear thinning slope. However, the shear thinning onset ($\dot{\gamma}_{crit}$) remained roughly the same ($10 \pm 1\ s^{-1}$).

The stability of the polymer at full CO_2 saturation at a longer time scale, the polymer was subjected to a shorter time scale aging test at the molar concentrations (0.027 mol/L) during the PA-WAG experiment. The results are presented in Figure 4.4. After keeping the sample at thermal stable conditions for one full day, the viscosity was measured in the rheometer (at day 1 thermal stability in Figure 4.4). The amount of CO_2 were injected and aged, with a measurement of the viscosity in the rheometer right after the 24 hours of aging (1 day after CO_2 exposure in Figure 4.4) and three days later (4 days after CO_2 exposure in Figure 4.4). Throughout those 5 days of stability testing, the viscosity over time displays no changes, retaining its viscosity under elevated temperature levels and the exposure to the PA-WAG levels of CO_2.

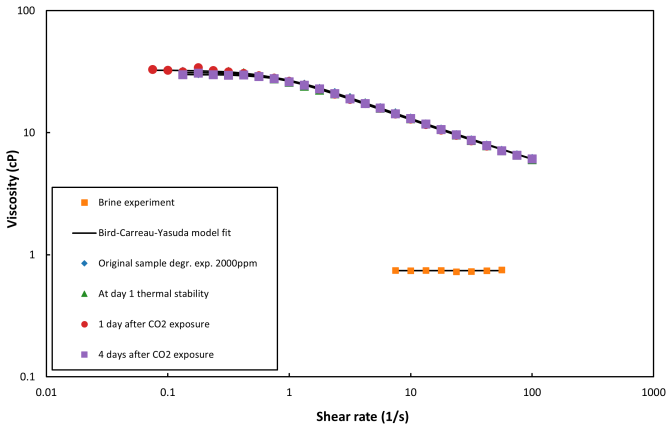

Figure 4.4: The stability of the polymer solution (2000 ppm SAV-10XV) at first only 40 °C for a day, after which it is exposed to CO_2 levels corresponding to the second cycle during the PA-WAG injection and aged for 24 hours. The viscosity is measured right after those 24 hours of aging and then again after an additional 3 days. The rheology over time displays no changes, retaining its viscosity under elevated temperature levels and the exposure to CO_2.

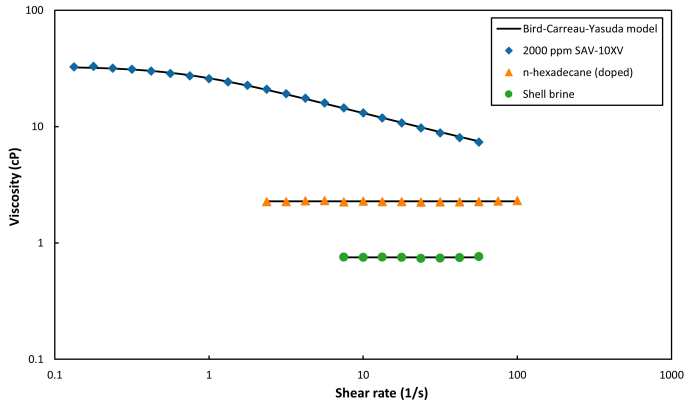

Figure 4.5: Rheometer results for the 2000 ppm SAV-10XV, n-hexadecane (doped) and Shell brine, with their respective Bird-Carreau-Yasuda model fit.

Besides the 2000 ppm SAV-10XV, also the brine (Shell brine, see Table 3.3) and the doped n-hexadecane are subjected to the rheometer in order to retrieve their viscosity at the temperature of 40 °C. The rheological data from those measurements is presented in figure Figure 4.5, along with their model fit using the Bird-Carreau-Yasuda model (subsection 3.4.2). The Newtonian plateau of the 2000 ppm SAV-10XV polymer solution is captured at the low shear rates, giving a η_0 of 32.8 $\pm$ 0.2 cP and the onset of the

shear thinning ($\dot{\gamma}_{crit}$) at 0.7 s^{-1}. The Shell brine shows the Newtonian, independent of shear rate, behaviour, displaying a viscosity of 0.74 $\pm$ 0.02 cP that also gives the η_∞ for the polymer solution. Lastly, the doped n-hexadecane illustrates its Newtonian behaviour with a viscosity of 2.27 $\pm$ 0.02 cP.

4.3. Core-flood experiments

This section presents and discusses the results from the performed core-flooding experiments. Overall saturation of the core was retrieved from volumetric material balance and recovered fluids, as the saturation (especially in three-phase systems) from CT-images was found to have a larger offset and is also affected by any effect of oil swelling due to CO_2 dissolution. This oil swelling, or fluid swelling in general when CO_2 dissolves into it, is ruled out from the fluids recovered after the backpressure at atmospheric conditions without an closed off environment. Without the elevated pressure, the CO_2 leaves the fluids up to a point that in does not have any visible effect on the fluids levels in the used collector vials (see Appendix H. The S_o profiles are therefor used to only visualize the changes over the core during the injections. The displayed pore volumes (PV) are all on reservoir conditions. The main results of the core-flood experiments are summarized in Table 4.1.

Table 4.1: The main results from the core-flood experiments carried out in this study. BT_x relates to the breakthrough time of the relevant phase.

	BT_w (PV)	BT_g (PV)	k^e_{ro}	k^e_{rp}/k^e_{rw}	S_{oi}	S_{or}	RF % OIIP
PF+CO_2	0.58$\pm$0.03	0.51$\pm$0.03	0.57$\pm$0.04	-	0.79$\pm$0.03	0.30$\pm$0.02	61.5$\pm$3.1
PF+CO_2 (rep.)	0.57$\pm$0.03	0.51$\pm$0.03	0.58$\pm$0.04	-	0.75$\pm$0.03	0.27$\pm$0.03	63.9$\pm$3.1
CO_2 +PF	0.32$\pm$0.03	0.42$\pm$0.03	0.53$\pm$0.04	-	0.70$\pm$0.03	0.19$\pm$0.03	72.4$\pm$3.1
WAG	0.22$\pm$0.03	0.27$\pm$0.03	0.52$\pm$0.04	0.22$\pm$0.03	0.78$\pm$0.03	0.19$\pm$0.03	75.8$\pm$3.1
PA-WAG (Bent.)	0.51$\pm$0.03	0.35$\pm$0.03	0.54$\pm$0.04	-	0.78$\pm$0.03	0.11$\pm$0.03	85.5$\pm$3.1
PA-WAG (Ind.)	0.22$\pm$0.03	0.10$\pm$0.03	0.73$\pm$0.04	- $\pm$ 0.005	0.50$\pm$0.04	0.12$\pm$0.03	75.5$\pm$4.1

4.3.1. Primary Drainage

In all of the core-flood experiments, the preparatory step primary drainage was performed before moving into any of the recovery injection schemes. During primary drainage, the oil phase applicable for the given experiment is injected into the core to reach S_{wc} and consequently S_{oi}, at a flow rate of 0.5 cm^3/min. The results in terms of total pressure drop profile, CT images and the associated saturation profile of one re-presentable primary drainage stage from the six experiments is presented and discussed in this section. The results of the primary drainage stages from all experiments can be found in Appendix F.

Pressure drop

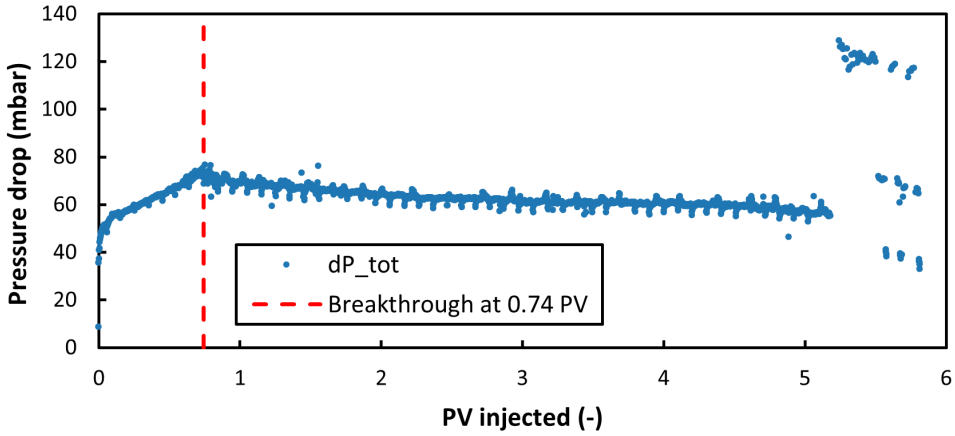

Figure 4.6: Total pressure drop profile for the primary drainage stage before PA-WAG in Bentheimer sandstone, experiment 5. After 5 PV, the injection flow rate was increased to 2.5 cm^3/min to initiate the bump flood for the oil phase and further reduce the water saturation towards S_{wc}. At the end, a relative permeability measurement for the oil was carried out. The breakthrough time of the oil phase was found at 0.74 $\pm$ 0.03.

Figure 4.6 illustrates the total pressure drop profile for the primary drainage stage of the PA-WAG experiment in Bentheimer sandstone (exp. 5), that is re-presentable for the core-flood experiments performed in this core type and oleic phase, namely n-hexadecane (see Table 3.2 for the dopants and the properties of the oil). A resolute increase in pressure drop can be recognized when the oil gets into contact with the core, which is due to the displacement of the less viscose brine (0.75 $\pm$ 0.02 cP) by the more viscose oil (2.26 $\pm$ 0.02 cP) and indicating the capillary entry pressure of approximately 40 $\pm$ 3 mbar for all the Bentheimer sandstone experiments. With the oil phase front further propagating through the rest of the core, the pressure drop displays a steadily increase until the breakthrough of oil at the producing side of the core can be seen at 0.74 $\pm$ 0.03 PV (Table 4.2 for the rest of the breakthrough times), reaching a maximum value for this steadily increase of approximately 78 $\pm$ 3 mbar for all experiments in Bentheimer sandstone. After breakthrough of the oil, the pressure drop starts fluctuating rather than forming a steady profile, with a general decreasing trend until an overall stable pressure drop trend is reached, indicating oil flow through the core at, or near, S_{wc}. The fluctuating, unstable flow can be explained by some of the remaining displaced phase, in this case water, is being mobilized and produced at the outlet, using a alternation on the one dimensional Darcy equation (Equation 3.1):

$$\Delta P = u_{total}(\frac{\eta_o}{k_{ro}k} + \frac{\eta_w}{k_{rw}k})L \tag{4.1}$$

, where u_{total} is the superficial velocity, η the viscosity of oil and water, k_r the relative permeability of the phases, k the absolute permeability and L the length of the core. If only the displacing fluid flows, in this case oil, the terms of the displacing fluid (water) are discarded, which leads to lower pressure drop values.

After the stabilized pressure drop at roughly 5 PV of oil injected into the core, the bump flood was performed to ensure the production of all movable water from the core and reaching the S_{oi}, and with that the S_{wc}, condition for the given experiments. The bump flood can be recognized by the sharp and large increase in pressure drop at approximately 5 PV, when a higher flow rate of 2.5 cm^3/min is applied. After a short while at this elevated flow rate until stable trend was reached, the flow rate was varied between from 0.5 to 1.25 and 2.5 cm^3/min and back (if needed multiple times) to create a stable permeability test in order to determine the endpoint relative permeability, k^e_{ro}, of the oil phase in the Bentheimer sandstone core. The breakthrough times, S_{oi} and S_{wc}, oil initially in place (OIIP) and k^e_{ro} of all the experiments are presented in Table 4.2 below, which are all in line with values found by

Janssen (2020) [20], reporting a study that also used Bentheimer sandstone cores and equally doped n-hexadecane oil for the core-flood experiments.

Table 4.2: Results in terms of breakthrough times and relative endpoint permeabilities for the primary drainage stage for the experiments with a Bentheimer sandstone core.

Experiment	Breakthrough (PV)	S_{oi}	S_{wc}	OIIP (mL)	k^e_{ro}
PF + CO_2	0.74 $\pm$ 0.03	0.79 $\pm$ 0.03	0.21 $\pm$ 0.03	34.3 $\pm$ 1.3	0.57 $\pm$ 0.04
PF+CO_2 (rep.)	0.75 $\pm$ 0.03	0.75 $\pm$ 0.03	0.25 $\pm$ 0.03	33.2 $\pm$ 1.3	0.58 $\pm$ 0.04
CO_2 + PF	0.72 $\pm$ 0.03	0.70 $\pm$ 0.03	0.30 $\pm$ 0.03	29.0 $\pm$ 1.3	0.53 $\pm$ 0.04
WAG	0.70 $\pm$ 0.03	0.78 $\pm$ 0.03	0.22 $\pm$ 0.03	32.1 $\pm$ 1.3	0.52 $\pm$ 0.04
PA-WAG (Benth.)	0.74 $\pm$ 0.03	0.78 $\pm$ 0.03	0.22 $\pm$ 0.03	33.0 $\pm$ 1.3	0.54 $\pm$ 0.04

Oil saturation profile supported with CT-imaging

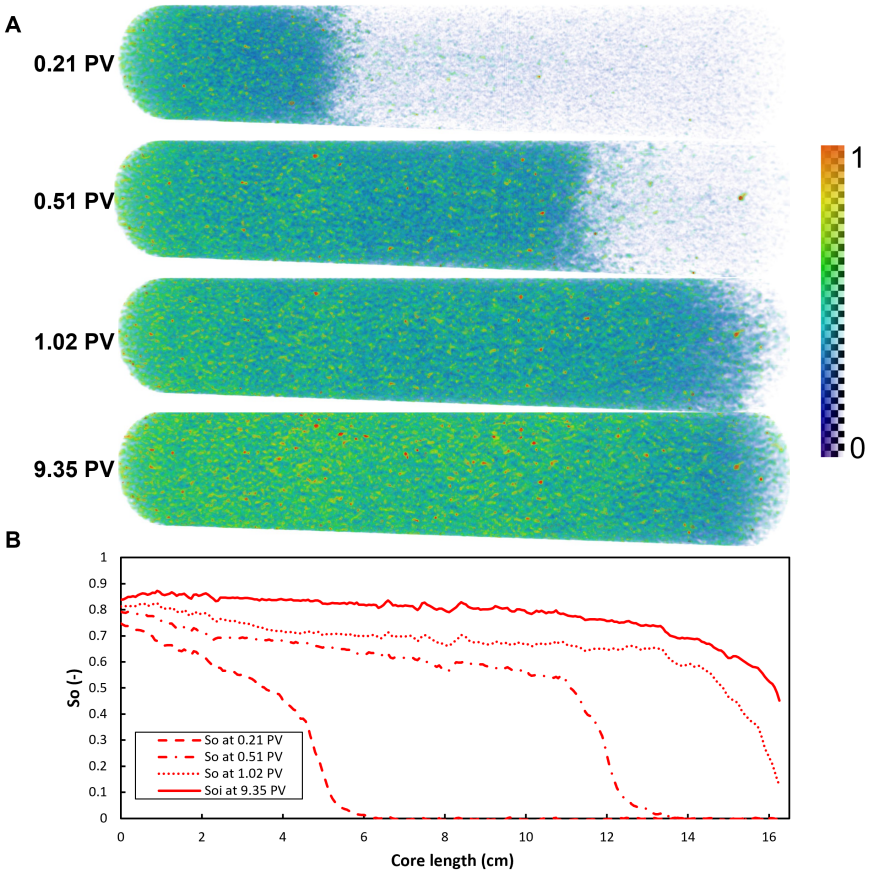

Figure 4.7: Displacement profile of the oil during primary drainage during PA-WAG in Bentheimer experiment (exp. 5) with (A) CT images and (B) oil saturation profile. P=0 refers to the start of the oil injection. (A) The oil phase (blue/green to yellow/orange) is being injected from the left side into the core, displacing the brine (light blue/white). As the amount of injected PV of oil increases, the S_o increases accordingly, visible by the overall increase of the higher saturation indicating colour yellow. (B) Profile of S_o presenting the primary drainage injection phase at different moment in terms of PV of oil injected. The oil front can be traced back to the piston like displacement visible in the CT-images above. As the number of PV injected increase, the average S_o increases accordingly until the S_{oi} is reached.

During the primary drainage of the core, the goal is to saturate the core with oil and increase the oil saturation across the core until S_{wc} is reached. This increase of oil saturation is visualized by the aid of

CT-scans, from which S_o is calculated for the two-phase system using Equation 3.8. This development of S_o along the core is visualized in Figure 4.7B, with the supporting CT-images in Figure 4.7A. During the primary drainage, the oil (blue/green to yellow/orange) injected from the left into the horizontally orientated Bentheimer sandstone core displaced the brine (light blue/white) in a piston-like, Buckley-Leverett displacement (see Figure 4.7A). This so called shock front can be traced across the S_o profile at approximately the same saturation level, before increasing which happens after the breakthrough of the oil phase.

At the end of the primary drainage, a lower S_o can be seen at the outlet (right side of the core, see Figure 4.7A&B), referring to a accumulation of brine as a result of the capillary end effect. Brine, as the wetting phase, accumulates near the outlet section of the core in order to satisfy the zero capillary pressure condition for this outlet boundary [16].

The S_{oi} is given for this experiment at 9.35 PV of the oil phase injected into the core. Due to a malfunction of the CT-scanner, the experiment was required to be lifted over the weekend to be able to continue. In order to do so, the injection flow rate was decreased to 0.01 cm^3/min. Saturation from before the weekend and after the weekend were compared, with no relevant changes in S_o as a result of the significant amount of around 3.5 PV more being injected over the weekend.

4.3.2. Polymer flooding followed by CO_2 flooding

The experiment on recovering oil from a Bentheimer core by using polymer flooding as a secondary mode and CO_2 as a tertiary mode was performed twice. During the first experiment, a higher injection rate of 2 cm^3/min instead of the 0.5 cm^3/min was implied during the polymer flood around 2 PV of polymer injected. This caused a sudden increase in pressure drop, along with the production of emulsion (see Figure 4.8. Due to the implied higher flow rate and the formation of emulsion, it was decided to repeat the experiment, in order to check the reproduce-ability. The repeated experiment (PF+CO_2 rep) is presented in this section. The first experiment can be seen in Appendix G.

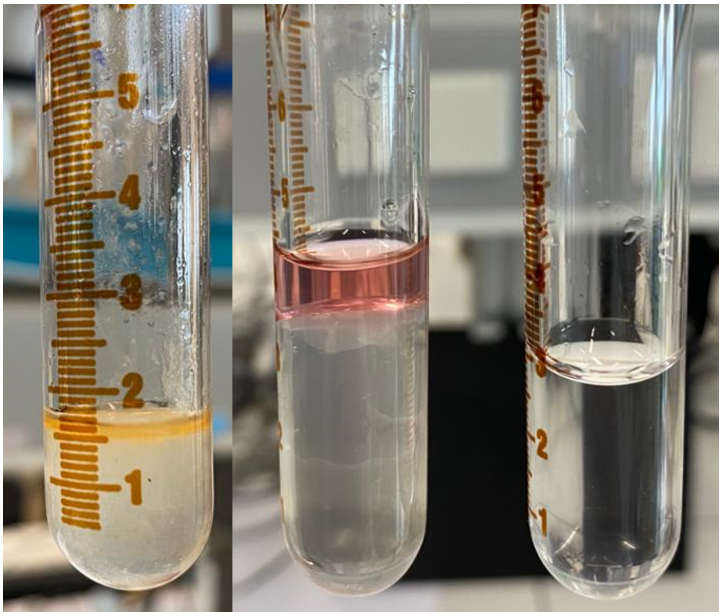

Figure 4.8: Emulsion formation seen during polymer flooding and at the beginning of CO_2 flood that followed. The left most image shows the heavier emulsion recovered from the core, the middle is some lighter emulsion and the right images is a clear recovered fluid from the core to form the contrast and check with the other two images.

Pressure drop

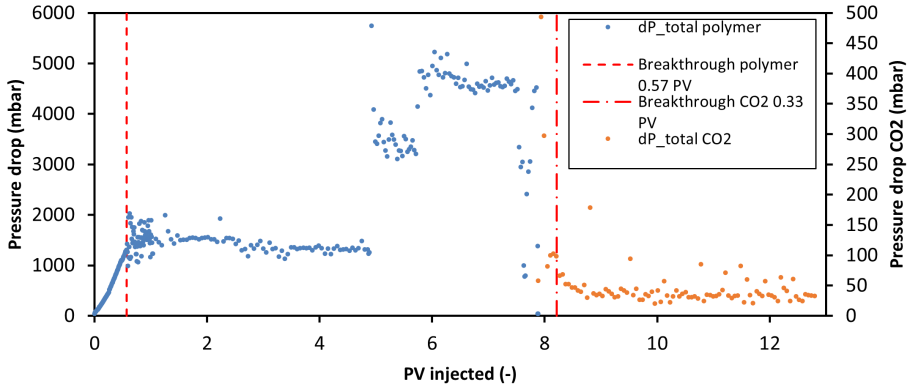

Figure 4.9: Pressure drop during both polymer flooding and CO_2 flooding for experiment 2 (PF+CO_2 rep.). Breakthrough of the polymer is achieved at 0.57 $\pm$ 0.03 PV. After approximately 5 PV of polymer injected, the flow rate is first increased to 1 cm^3/min and later to 1.5 cm^3/min until stabilization of the pressure drop. This was done to check the formation of emulsion would occur again with a higher flow rate and repeat experiment 1. CO_2 flooding was initiated after polymer flooding, with breakthrough after 0.33 $\pm$ 0.03 PV.

The pressure drop profile for the repetition experiment for polymer flooding followed by CO_2 flooding is given in Figure 4.9. When flooding the core with the polymer solution at a flow rate of 0.5 cm^3/min, a steady increase in pressure drop to 1300 $\pm$ 10 mbar can be seen until breakthrough of the polymer occurs at 0.57 $\pm$ 0.03 PV. This is much higher than previously seen with the primary drainage, due to the much higher viscosity of the polymer compared to the oil. At and slightly after breakthrough of the polymer, light emulsion was visible in the recovered fluids. The characteristically fluctuations (as discussed with Equation 4.1) in pressure drop can be seen when breakthrough has occurred due to production of different fluid phases. During these fluctuations, the overall trend of the pressure drop slightly increases to 1500 $\pm$ 10 mbar, after which the pressure drop slowly decreases until reaching it's steady state pressure drop at 1300 $\pm$ 10 mbar. Then, the flow rate is first increased to 1 cm^3/min and later to 1.5 cm^3/min until stabilization of the pressure drop. This higher flow rate was implemented to repeat the previous experiment and reproduce emulsions under higher flow rates. Right when the higher flow rates where applied, emulsions were again seen in the recovered fluids. After stabilization of the pressure drop at the injection rate of 1.5 cm^3/min, the relative permeability test was executed, varying flow rates between 0.5, 1 and 1.25 cm^3/min. A relative permeability for the polymer, k_{rp}, of 0.034 $\pm$ 0.005 was found, with which the mobility ratio from Equation 2.1 of the displacement could be determined. The very low mobility ratio, due to the low relative permeability of the polymer and it's high viscosity with respect to the n-hexadecane, indicates very favourable displacement.

CO_2 flooding was initiated after the relative permeability test of the polymer. The breakthrough of CO_2 occurred at 0.33 $\pm$ 0.03 PV injected, with pressure dropping quickly afterwards and displaying the characteristic fluctuation in pressure for producing different fluid phases at the outlet. This decrease went to the steady state value of approximately 32 $\pm$ 3 mbar. After the backpressure of the system, CO_2 is very clearly coming out of solution due to pressure release. During CO_2 flooding, light emulsion continued to appear in the recovered fluids. In Table 4.3, the main results for the experiments 1 and 2 retrieved from the pressure data can be seen.

Table 4.3: Results from pressure data for the experiments using polymer flooding and CO_2 flooding as a secondary and tertiary recovery mode, respectively.

	Breakthrough polymer (PV)	Breakthrough CO_2 (PV)	k^e_{rg}	M
PF+CO_2	0.58 $\pm$ 0.03	0.58 $\pm$ 0.03	-	0.010 $\pm$ 0.002
PF+CO_2 rep.	0.57 $\pm$ 0.03	0.33 $\pm$ 0.03	-	0.011 $\pm$ 0.002

Oil saturation profile supported with CT-imaging

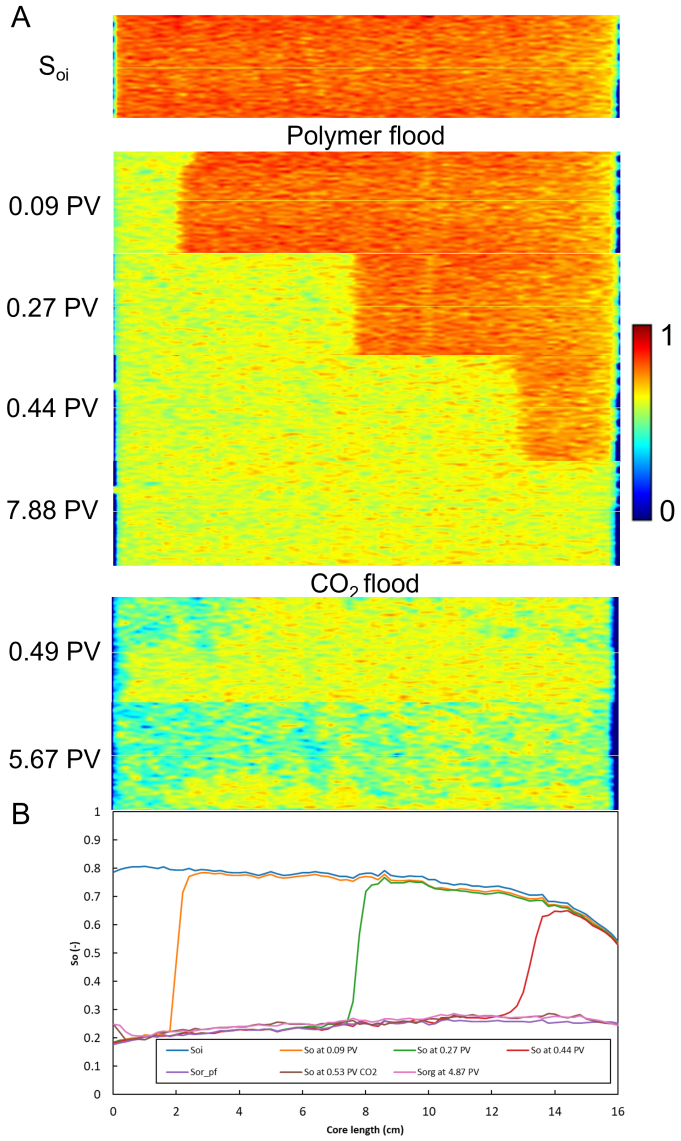

Figure 4.10: P=O refers to the start of the polymer flooding. (A) The CT-images taken during the course of experiment 2 with the S_{oi} from primary drainage on top, followed by polymer flooding as a secondary recovery mode and CO_2 flooding as a tertiary. The breakthrough of polymer is found at 0.57 $\pm$ 0.03 PV. CO_2 shows clear segregation with an early breakthrough due to this bypass at 0.33 $\pm$ 0.03 PV. At the end, a section of the bottom of the core remains unswept by CO_2. (B) S_o profile across the core during the scans presented in A.

The displacement of oil by the polymer in Figure 4.10 shows a very sharp, stable, piston like front, indicating favourable displacement, which is in line with the earlier found very low mobility ratio between the used polymer and the oil. This sharp shock front is also visible in the S_o profile below the CT-images. The breakthrough of the polymer at 0.57 $\pm$ 0.03 PV is slightly after the scan of 0.44 $\pm$ 0.03 PV. During the first three scans, the capillary end effect stays apparent. After 7.88 $\pm$ 0.03 PV, the S_{orp} of 0.31 $\pm$ 0.03 is reached.

When injecting CO_2 in the core as a tertiary mode, a clear segregation is visible. The CO_2 appears to mostly bypass the polymer over the top with an early breakthrough at 0.33 $\pm$ 0.03 PV, due to the contrast in density and viscosity between the CO_2 and polymer. Over the course of 5.67 $\pm$ 0.03 PV, the S_{org} of 0.27 $\pm$ 0.03 is reached. The CT-image at S_{org} shows that a small part of the bottom of the core remains unswept by the CO_2. The found S_o from CT-images during CO_2 flooding showed an increase

in S_o, with a maximum of 7% at the end of CO_2 flooding, while oil was recovered during this injection. This indicates oil swelling by the dissolution of CO_2 into the oil, as an increase by recovering remaining oil from the inlet cap was ruled out with CT-data. Dissolution of the CO_2 into the oil, as well as in the aqueous phase that is also present in the core, happens in all other experiments as well, only there this is not visible in S_o as saturation and recovery levels are to high in those cases for it to show in the S_o profile.

Oil recovery factor

Figure 4.11 shows the recovery factor of experiment 2, along with both oil and water cut. 96% of the oil recovered by polymer flooding is done before breakthrough, with an total recovery factor after full injection of 58.6 $\pm$ 3.0%. With CO_2 as a tertiary mode, the incremental recovery was low, with 5.3%. All the recovery by CO_2 is done after breakthrough. Phase cuts during CO_2 injection indicates that after breakthrough, mostly CO_2 itself is being recovered from the core. At the end of CO_2 flooding, a total recovery of 63.9 $\pm$ 3.1% was established.

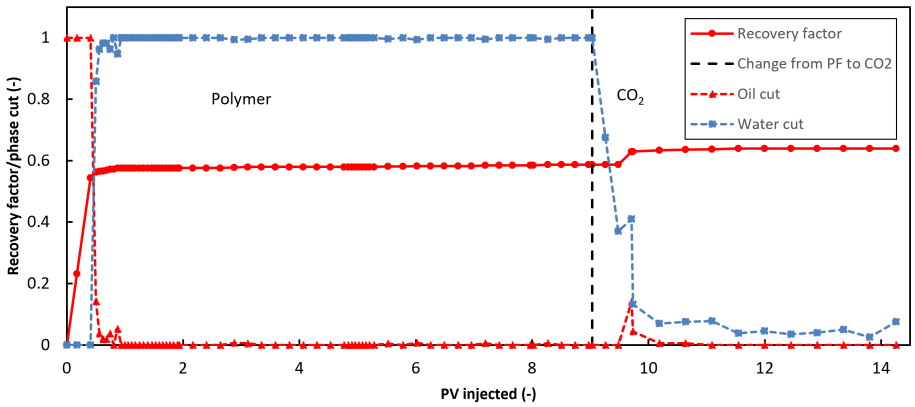

Figure 4.11: Recovery factor profile along with the oil and phase cuts during both the secondary and tertiary recovery modes of polymer and CO_2 flooding. A recovery of 58.6 $\pm$ 3% during polymer injection is achieved, with an incremental recovery of 5.3 % to a total recovery of 63.9 $\pm$ 3% with CO_2 flooding.

4.3.3. CO_2 flooding followed by polymer flooding

Pressure drop

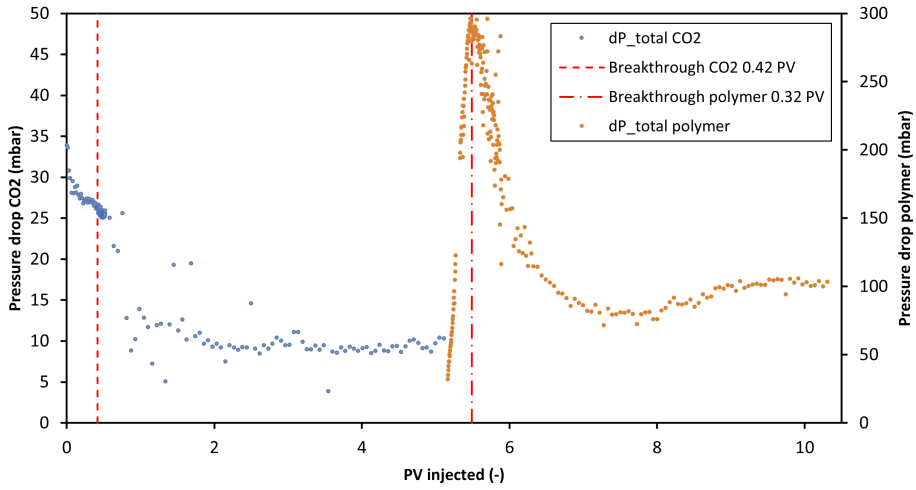

Figure 4.12: Total pressure drop profile over the course of the third experiment with CO_2 flooding as secondary recovery mode and polymer as tertiary. Breakthrough of CO_2 occurred at 0.42 PV. After roughly 5 PV of CO_2, the polymer flood is initiated. The breakthrough of polymer was achieved 0.32 $\pm$ 0.03 PV.

In Figure 4.12, the pressure drop profile for the experiment with CO_2 as a secondary recovery mode and polymer as a tertiary is presented. A decreasing trend is visible from the start of injection, due to the very rapid breakthrough of CO_2 through the first two individual differential sectors of the core (4 differential pressure transducers for monitoring the core, see Figure 3.4). The pressure decreased from the initial capillary entry pressure of 37 $\pm$ 3 mbar to 26 $\pm$ 3 mbar at breakthrough. This breakthrough of CO_2 occurs at 0.42 $\pm$ 0.03 PV. Shortly after the breakthrough, the pressure drop sharply declines and starts to show the distinctive fluctuations of the co-production of different fluid phases. The general decreasing trend after breakthrough flattens towards the steady-state pressure of 10 $\pm$ 3 mbar.

When switching to polymer flooding, a sharp increase in pressure drop is observed to a maximum of 292 $\pm$ 3 mbar at the breakthrough of the polymer at 0.32 $\pm$ 0.03 PV. After the breakthrough of polymer, the pressure drop starts decreasing swiftly, rather than showing a gradual decreasing trend with fluctuations from co-producing different fluid phases as is the case when polymer was used as a secondary recovery mode in Figure 4.9. The decline continued until the lowest point of this trend was reached at 80 $\pm$ 3 mbar at roughly 7.2 $\pm$ 0.03 cumulative PV injected, after which it started to increase again to reach the steady-state pressure drop of 100 $\pm$ 3 mbar at the end of polymer injection. The sharp decrease in pressure drop resulted from the fast breakthrough of polymer via the CO_2 saturated top section of the core, leaving some part of the core relatively unswept by the polymer at this stage. The increase towards steady-state pressure indicated polymer filled the whole core more evenly. No relative permeabilities were recovered for the two different phases and no emulsions were recovered during the complete injection of both CO_2 and polymer.

Table 4.4: The main results from the pressure drop data for the CO_2 flooding followed by polymer flooding experiment.

Breakthrough aqueous phase (PV)	Breakthrough CO_2 (PV)
0.32 $\pm$ 0.03	0.42 $\pm$ 0.03

Oil saturation profile supported with CT-imaging

Figure 4.13 illustrates the S_o and the CT-images from which the S_o was derived. During CO_2 injection, clear gravity segregation occurs throughout the core due to the difference in densities between oil and CO_2. The CO_2 only sweeping the upper part of the core right from the beginning of injection results in an quick breakthrough of CO_2 after 0.42 $\pm$ 0.03 PV injected. During this stage of the injection, the S_o profile from Figure 4.13B indicates a higher S_o at the second half of the core at 0.15 and 0.25 PV, indicating the forwardly displaced oil from the first half of the core. CO_2 did not reach this part of the core, hence the increase of S_o by oil swelling is ruled out. After breakthrough, the CO_2 starts to sweep more of the bottom part of the core, but leaves a section unswept at the end of full injection. This resulted in a S_{org} of 0.43 $\pm$ 0.03.

After CO_2 flooding, polymer flooding was initiated. Just before breakthrough of the polymer at 0.32 $\pm$ 0.03 PV, the polymer is seen to have swept $\frac{3}{5}$ of the oil over the width of the core, but leaving the last $\frac{2}{5}$ relatively unswept, especially the bottom part. The sweeping of the polymer is translated into a large decrease in S_o visible in the first half of the core in Figure 4.13B. Over full injection of the polymer phase, the core is visibly quite evenly swept and an S_{or} of 0.19 $\pm$ 0.03 was reached.

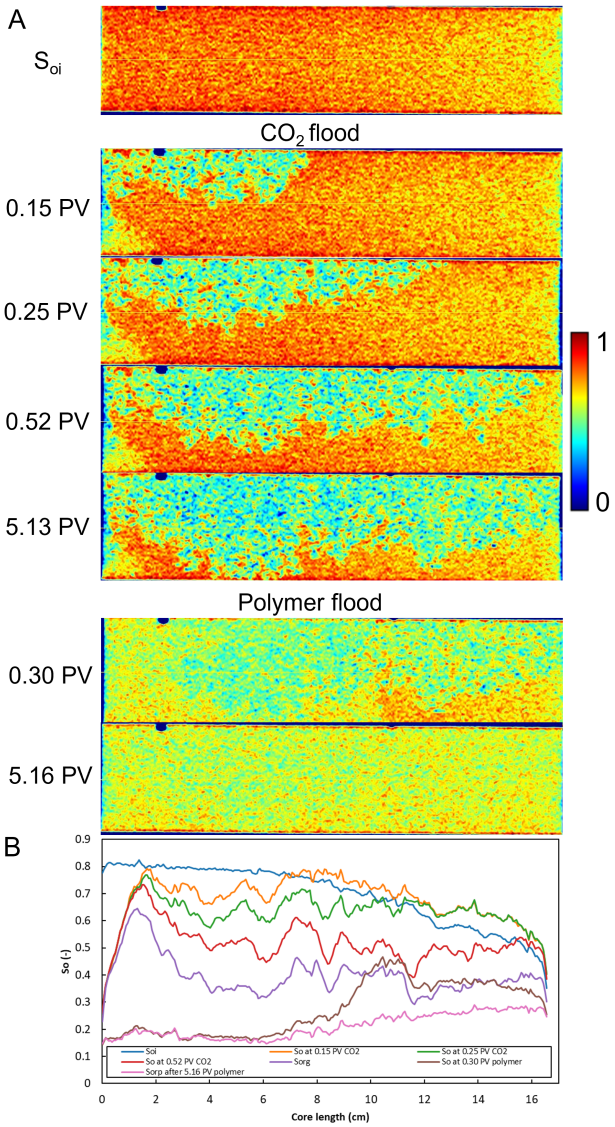

Figure 4.13: (A) CT-images taken during the injection of the different fluid phases from which S_o is determined. The S_oi scan is presented on top, followed by CO_2 flooding and polymer injection images. During CO_2, clear gravity segregation is visible between the gaseous and oleic phase. Breakthrough of CO_2 occurred at 0.42 $\pm$ 0.03 PV. At the end of CO_2 injection, a section at the bottom of the core remains unswept. Polymer is then injected as tertiary recovery mode. (B) S_o profile during the whole of the secondary and tertiary injection modes.

Oil recovery factor

The recovery of the experiment with CO_2 followed by polymer flooding, along with the oil and water cut, are presented in Figure 4.14. Before the breakthrough of CO_2, around 26 $\pm$ 3% of the OIIP is recovered. This translates to 68% of the oil that is recovered by CO_2 injection in total. With the remaining approximate 4.9 PV of CO_2 injected, a total recovery factor by CO_2 of 0.39 $\pm$ 0.03 is established.

After CO_2 injection, polymer flooding is initiated as tertiary recovery. A large incremental recovery by polymer flooding of 33.6% can be seen, from which 96% is recovered before or slightly after breakthrough of the polymer phase. A total recovery with polymer flooding after CO_2 of 72.4 $\pm$ 3.2% was reached. The large incremental recovery by the polymer is due to two main reasons. Firstly, the CO_2 left part of the core unswept and recoverable by the polymer, that is less subjective to gravity segregation because of the smaller difference in density with the oil phase. Secondly, the injection of CO_2 at immiscible conditions results in dissolution of the CO_2 in the phases present in the core at that time, namely polymer and the remaining oil. The dissolving CO_2 into the n-hexadecane results in swelling of the oil. By this swelling, the oil is more easily swept from the pores by the polymer, but also the

viscosity of the oil is decreased. This decrease is oil viscosity will results in a even more favourable mobility ratio between the highly viscose polymer and the now less viscose oil.

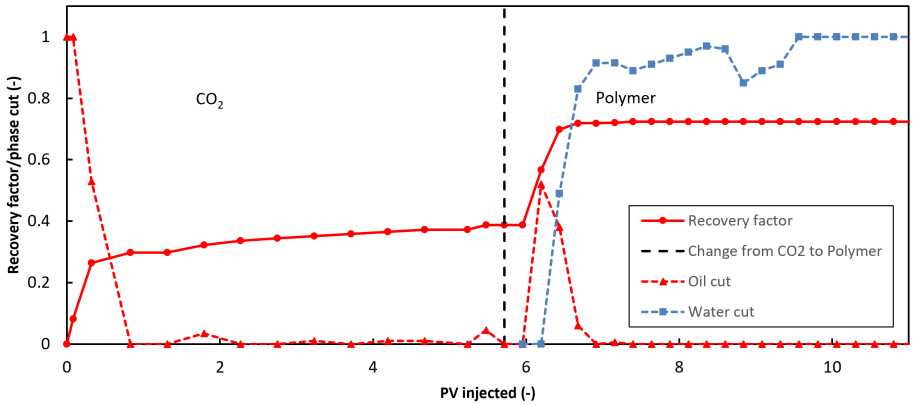

Figure 4.14: Representation of the recovery factor over the course of the experiment using CO_2 and polymer flooding as a respective secondary and tertiary recovery. With CO_2 flooding, a recovery of 38.8 $\pm$ 3.1% is recovered. With polymer as a tertiary mode, an incremental recovery of 33.6% is established. This results in a total recovery for the complete experiment of 72.4 $\pm$ 3.2%.

4.3.4. WAG vs PA-WAG

The sweep efficiency improvement of the water alternating gas injection by the addition of specially designed polymer is one of the main objectives within this study. In this section, the results of the performed WAG core-flood experiment are side by side compared to the PA-WAG core flood experiment, to highlight the differences between the two injection schemes. The CT-scans are visualized with Avizo, and the CT-data is retrieved from the scan via ImageJ processing.

Pressure drop

Figure 4.15 presents the total pressure drop profile during both the WAG and PA-WAG injection for oil recovery from Bentheimer sandstone cores. The cycles start with the injection of the aqueous phase slug (brine for WAG and polymer for PA-WAG) at 2 cm^3/min, followed by the injection of the CO_2 slug at 0.5 cm^3/min. Both experiments show a similar pressure drop profile due to there similarity in injection scheme. The polymer slug injection of the first cycle of PA-WAG is comparable to the pressure drop profile from experiment PF+CO_2 rep., visible in Figure F.1. Evaluating the dP at the same injected PV into the core, the pressure drop at the end of the polymer slug for PA-WAG of 841 $\pm$ 5 mbar is four times higher than for the PF+CO_2 rep. experiment, in line with the 1D Darcy's law (Equation 3.1) for injecting the polymer slug at a 4 times higher injection rate for the PA-WAG experiment. Due to the difference in viscosity of the phases, the PA-WAG experiment shows a higher pressure drop during the injection of the polymer slugs, compared to the brine slugs during WAG injection. The shift to CO_2 for the first cycle means a pressure drop from 127 $\pm$ 3 to 50 $\pm$ 5 mbar for the WAG injection and 841 $\pm$ 5 to 80 $\pm$ 5 mbar for the PA-WAG injection and determined with CT-images, alongside the pressure data, the breakthrough for CO_2 during the two experiments was found at 0.27 $\pm$ 0.03 PV and 0.35 $\pm$ 0.03 PV of injected CO_2 (0.50 $\pm$ 0.03 PV and 0.57 $\pm$ 0.03 PV in total), respectively. This indicates that the polymer used in the PA-WAG injection slightly delayed the CO_2 breakthrough over the WAG injection, using cores with comparable properties (Table 3.4).

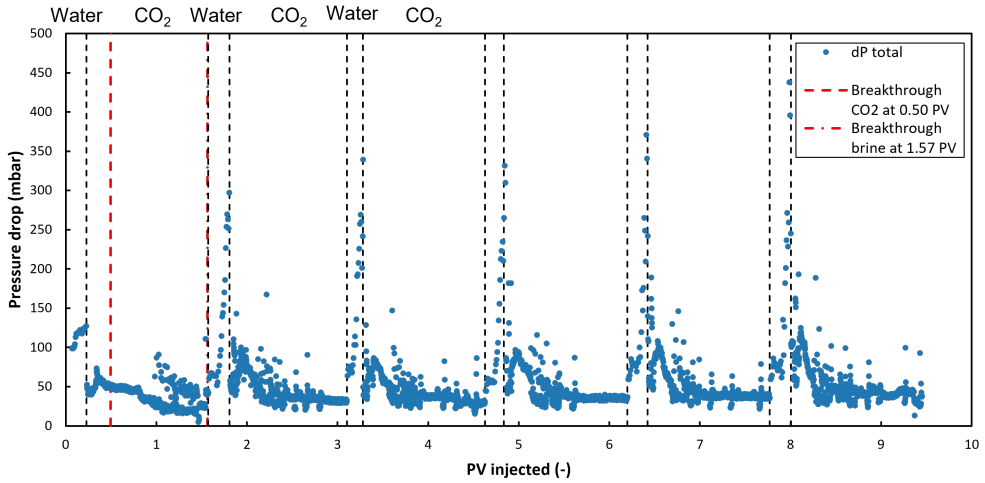

(a)

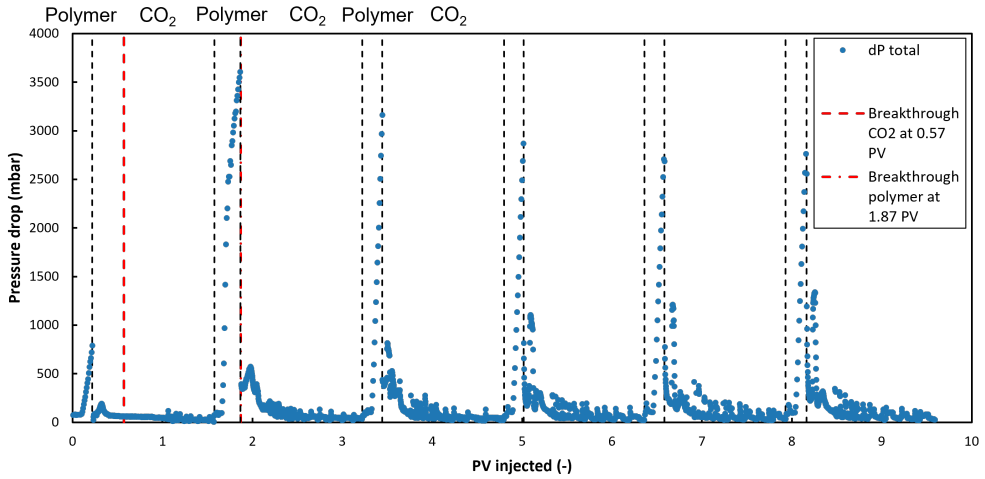

(b)

Figure 4.15: (a) WAG pressure profile, illustrating the characteristic pressure drop behaviour of injecting a WAG-scheme with different slug sizes and injection rates for the aqueous (0.22 PV at 2 cm^3/min) and CO_2 phase (1.3 PV at 0.5 cm^3/min). CO_2 breakthrough occurred at 0.27 $\pm$ 0.03 PV of only CO_2 injected and 0.50 $\pm$ 0.03 PV in total injected PV. The brine breakthrough occurred at 0.22 $\pm$ 0.03 PV of brine injected and 1.57 $\pm$ 0.03 PV in total. The first three cycles of slugs are indicated above the graphs. (b) PA-WAG pressure profile, illustrating the characteristic pressure drop behaviour of injecting a PA-WAG-scheme with different slug sizes and injection rates for the polymer (0.22 PV at 2 cm^3/min) and CO_2 phase (1.3 PV at 0.5 cm^3/min). CO_2 breakthrough occurred at 0.35 $\pm$ 0.03 PV of only CO_2 injected and 0.57 $\pm$ 0.03 PV in total injected PV. The polymer breakthrough was established at 0.51 $\pm$ 0.03 PV of brine injected and 1.87 $\pm$ 0.03 PV in total. The first three cycles of slugs are indicated above the graphs.

As the second, or any other, slug of the aqueous phase is being injected, which is accompanied by the change from CO_2 injection to either brine or polymer injection, a sharp increase in pressure drop can be observed. Following the studies of Janssen (2020) [20] and Shahverdi and Sohrabi (2016) [47], this distinct increase is presumably due to the combination of an increase in injection rate and advancement of S_{gt}, a trapped (non-moveable) gas saturation. By considering the one dimensional Darcy's law for multi-phase flow, it can be explained [6]:

$$\Delta P = u_{total}\left(\frac{f_o \eta_o}{k_{ro} k} + \frac{f_w \eta_w}{k_{rw} k} + \frac{f_g \eta_g}{k_{rg} k}\right) L \tag{4.2}$$

, where ΔP, u_{total}, f_x, η_o, k_{ra}, k and L are representing the pressure drop, total superficial velocity, fractional flow phase x, viscosity phase x, relative permeability phase x, absolute permeability and core length, respectively. The subscripts refer to the three different phases oil, brine or polymer and gas, present at that time in the system. The increased u_{total} by a factor of 4, accompanying the switch

from gas to aqueous phase, cannot be solely responsible for the increase from 25 $\pm$ 5 to 297 $\pm$ 5 mbar for WAG and 30 $\pm$ 5 to 3605 $\pm$ 10 mbar for PA-WAG. Injecting the aqueous phase results in an increase in S_w and a decrease in S_o, inflicting changes in $\frac{\eta_o}{k_{ro}k}$ and $\frac{\eta_w}{k_{rw}k}$. The increase in S_w entails an amplified k_{rw}, while it decreased the S_o only slightly, as minimal amounts of oil are recovered during the second brine and polymer slugs based on the effluent analysis. This small decline in S_o implies a minor decrease in k_{ro}. The changes in both k_{rw} and k_{ro} result in larger decrease of $\frac{\eta_w}{k_{rw}k}$ than the increase of $\frac{\eta_o}{k_{ro}k}$. To be in agreement with the observed increased pressure drop following the change from CO_2 to the aqueous phase, $\frac{\eta_g}{k_{rg}k}$ must increase accordingly, requiring a decline in k_{rg} by the reduction of the free movable gas saturation S_{gf} due to both the production of CO_2 and formation of S_{gt}. The brine and polymer breakthroughs are found at 1.57 and 1.87 cumulative PV (0.22 and 0.51 PV in terms of the aqueous phase by itself), having a significant delay of aqueous phase breakthrough between WAG and PA-WAG injections by a whole injection slug due the addition of polymer.

For the second CO_2 slug, the overall steady trend of the pressure drop was slightly increased, most probably due to the presence of S_{gt} and enlarged S_w, from 25 $\pm$ 3 to 35 $\pm$ 5 mbar for the WAG injection and 30 $\pm$ 5 to 45 $\pm$ 5 mbar for the PA-WAG injection. This steady-state pressure drop remained for the following cycles approximately the same for the gas slug.

After full injection of either the WAG or PA-WAG scheme, the CO_2 injection was continued with a bump flood to reach both S_{wc} and S_{or}, so that the relative endpoint permeability (k^e_{rg}) of CO_2 can be determined. Thereafter, the brine or polymer bump flood was executed to determine the k^e_{rp} or k^e_{rw} as well. No success was encountered by the determination of either the k^e_{rg} as the k^e_{rp}. The results from the pressure drop data can be seen in Table 4.5.

Table 4.5: The main results from the pressure drop data for the WAG and PA-WAG experiment.

	Breakthrough aqueous phase (PV)	Breakthrough CO_2 (PV)	k^e_{rw}/k^e_{rp}
WAG	0.22 $\pm$ 0.03	0.27 $\pm$ 0.03	0.22 $\pm$ 0.02
PA-WAG	0.51 $\pm$ 0.03	0.35 $\pm$ 0.03	-

Oil saturation profile supported with CT-imaging

The saturation profiles, along with the corresponding CT-images taken during the injection, of both the WAG and PA-WAG can be found in Figure 4.16 and Figure 4.17, respectively. The two show a very similar profile of saturation throughout the CT-scans. During injection of the first brine and polymer slug, the displacement front is stable with a good sweep of the past section of the core. The front of the brine slug at the end of the slug injection at 0.23 $\pm$ 0.03 PV shows a slight segregation due to the density difference between oil and brine. The bottom part of the front is lightly in front of the top section. This is not the case for the first polymer slug at 0.22 $\pm$ 0.03 PV. The formation of an oil bank can be seen in front of the brine and polymer during the whole injection of the first cycle in the retrieved S_o profile of Figure 4.16B' and Figure 4.17B'. With injection of CO_2 during the first cycle, a clear segregation with the much less dense CO_2 than the phases already in the core is visible. The CO_2 bypasses most of the brine and polymer present in the first half of the core and displaces the oil at the top of the core in the second half beyond the displacement front from the aqueous slugs. In the CO_2 slug for the first cycle of the WAG, the gas is visibly accumulated at the inlet of the core, while with the CO_2 slug for the first cycle of the PA-WAG, the CO_2 is more spread out throughout the polymer occupied section of the core. The CO_2 at 0.26 $\pm$ 0.03 PV for both the WAG and PA-WAG forms a small oil bank at the end of the core, seen in Figure 4.16B' and Figure 4.17B', before the S_o declines sharply due to the capillary end effect. At the end of the full first CO_2 slug, in both the WAG and PA-WAG, a potion of the the bottom section of the core remains relatively unswept by both brine or polymer and CO_2. The first cycles in the two experiment reached a $S_{or,cycle1}$ of 29.7 $\pm$ 3.1% for WAG and 28.9 $\pm$ 3.1% for PA-WAG, retrieved from volumetric material balance.

Injecting the second cycle for WAG and PA-WAG, starting with brine and polymer slug, the main impact for both experiment can be seen by the displacement of the oil which was occupying the center bottom part of the core after the first cycle. In both the CT-images and the S_o profiles (C and C' parts of the illustration Figure 4.16 and Figure 4.17), this oil is displaced and an oil bank is formed towards the end of the core for the injection at 0.11 $\pm$ 0.03 PV in both experiments. At the end of the aqueous phase injection for both experiments, some of this accumulation of oil at the end of the core, mostly in the

bottom section, is still present. Switching to CO_2 for injection, the S_o remains unchanged in the first half of the core throughout the full slug injection. From the CT-images, there is a change in overall saturation of the core, as the images do not represent a single phase. As in the first cycle, the CO_2 appears to be more evenly spread out over the core in the PA-WAG experiment than for the WAG, were it is more accumulated at the top and end sections of the core. This results in a larger unswept area by the CO_2 during the second cycle of the WAG than for the second cycle of the PA-WAG, which shows a visible lower overall core fluid saturation in the CT-images of Figure 4.17C and S_o in Figure 4.17C'. Most of the difference between the WAG and PA-WAG experiment in terms of sweep efficiency and achieved S_{or} is established during this second cycle. The $S_{or,cycle2}$ reached in WAG and PA-WAG after cycle two of injection are 22.5 $\pm$ 3.1% and 14.1 $\pm$ 3.1%, respectively.

Over the course of the remaining four cycles of injection for WAG and PA-WAG, only small decreases in S_o are visible, mainly at the beginning and end section of the core (see Figure 4.16D' and Figure 4.17D'). The overall fluid saturation displayed in the CT-images has decreased in either of the experiments, with most noticeable the bottom center section of the core. With the full WAG and PA-WAG complete, the S_{or} achieved for the experiments are 22.5 $\pm$ 3.1% and 11.3 $\pm$ 3.1%, respectively.

Oil recovery factor

The recovery factor development over the course of both the WAG and PA-WAG experiments, along with their corresponding oil and water cuts, are presented in figures 4.18a and 4.18b. The oil recovered during the first cycle is highly comparable between the two experiments, reaching a recovery factor of 0.62 $\pm$ 0.03 for the WAG and 0.63 $\pm$ 0.03 for the PA-WAG injection, which translate to 81% and 73% of the total recovery. Most of this recovery is achieved after the CO_2 breakthrough in both experiments. The main difference between WAG and PA-WAG injections in terms of sweep efficiency and recovery, as mentioned in section Table 4.3.4, is established in the second cycle. Where the WAG injection recovery factor increased to 0.71 $\pm$ 0.03, the PA-WAG was able to increase the recovery factor to 0.82 $\pm$ 0.03. These increases resulted in achieving 94% and 96% of total recovery for WAG and PA-WAG, respectively. In both experiments, the bulk of this recovery occurred with the breakthrough of the aqueous phase, which was at the start of the injection of the second brine slug for WAG and at the end of the injection of the second polymer slug for PA-WAG. In the remaining four cycles, minimal amounts of oil where recovered, which was also displayed in terms of saturation in Table 4.3.4. Noticeable for cycles 2 to 6 for both the WAG and PA-WAG, is that the produced oil coincides with the production of the aqueous phase. This aqueous phase production is for polymer, just like the breakthrough, in each cycle slightly delayed compared to the brine in the WAG. In the PA-WAG experiment, emulsions were recovered from the production of polymer in the fourth cycle and onward to the end of production. With the full WAG and PA-WAG recovery injection schemes, respective total recovery factors of 0.76 $\pm$ 0.03 and 0.85 $\pm$ 0.03 were achieved.

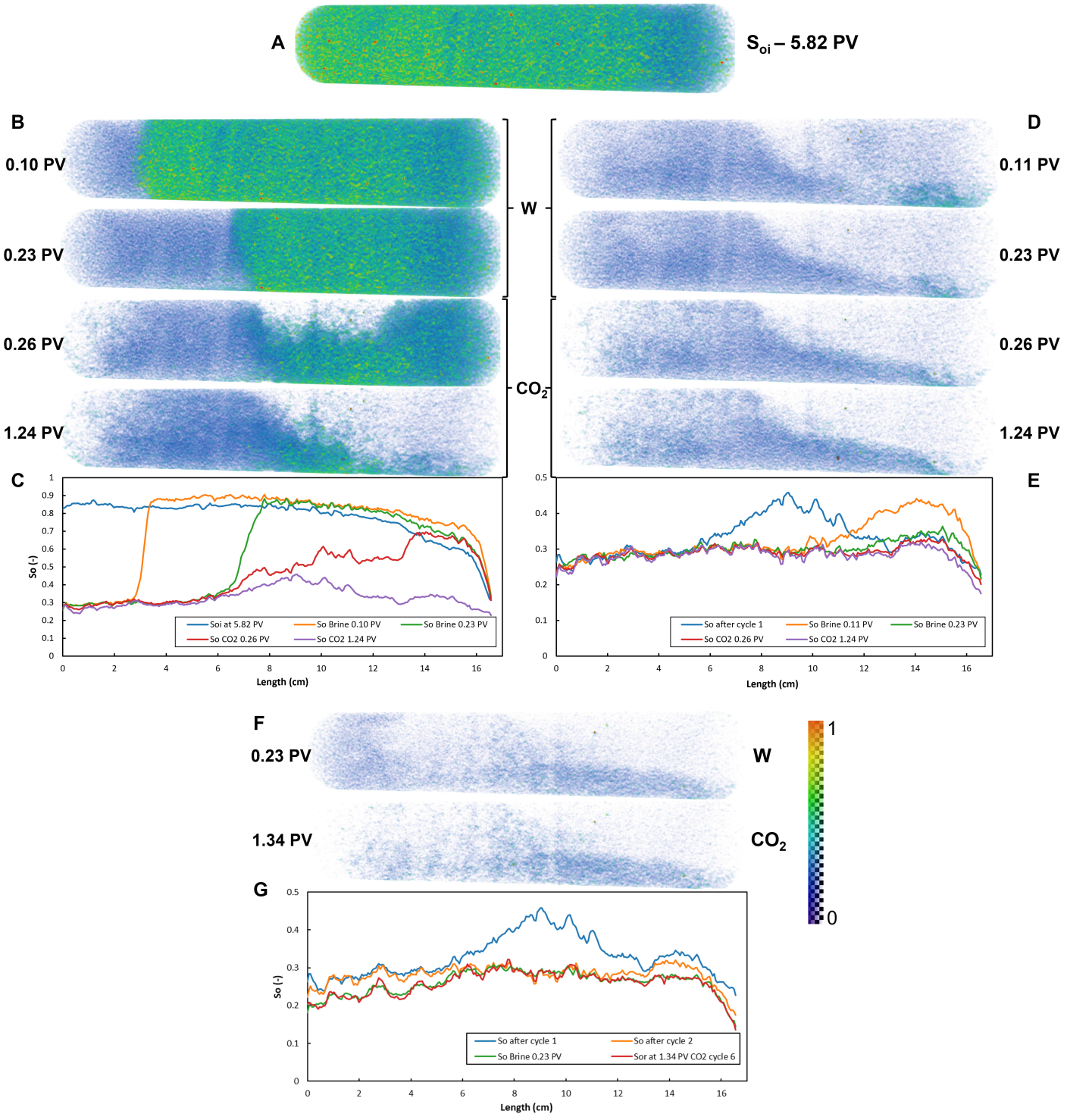

Figure 4.16: For all CT-images: oil phase (blue/green to yellow/orange), brine (light blue/white), CO_2 (white). P=O refers to the start of injection of the presented cycle.(A) S_{oi} of 77.6 $\pm$ 3.1% after 5.82 $\pm$ 0.03 PV of primary drainage. (B) First WAG cycle CT-images, with the brine injection in the first two images and the CO_2 in the second two. Both brine and CO_2 are injected from the left and oil is produced at the right side of the core. The brine displacement of the oil shows a stable front, whereas the CO_2 shows clear gravity segregation by flowing over the top of the brine slug and displacing the oil in the second half of the core, leaving a large part of the bottom and middle section of the core unswept by CO_2. (C) S_o profile over the course of the first WAG cycle, matching the presented scans above. $S_{or,cycle1} = 29.7 \pm 3.1\%$. (D) Second WAG cycle CT-images, same order in scans presented as the first cycle. Small changes in saturation for mainly the second half of the core during full brine slug injection and the beginning of the core during CO_2 slug injection. A large part of the bottom of the core remains by CO_2. (E) S_o profile over the course of the second WAG cycle, matching the presented scans above. $S_{or,cycle2} = 22.5 \pm 3.1\%$. (F) Full WAG injection scheme completed with cycle 6. A small part of the bottom of the core remains unswept. (G) During the course of cycle 3 till the full WAG, only a 3.8% decrease in S_o, resulting in a S_{or} of 18.7 $\pm$ 3.1% for the full WAG.

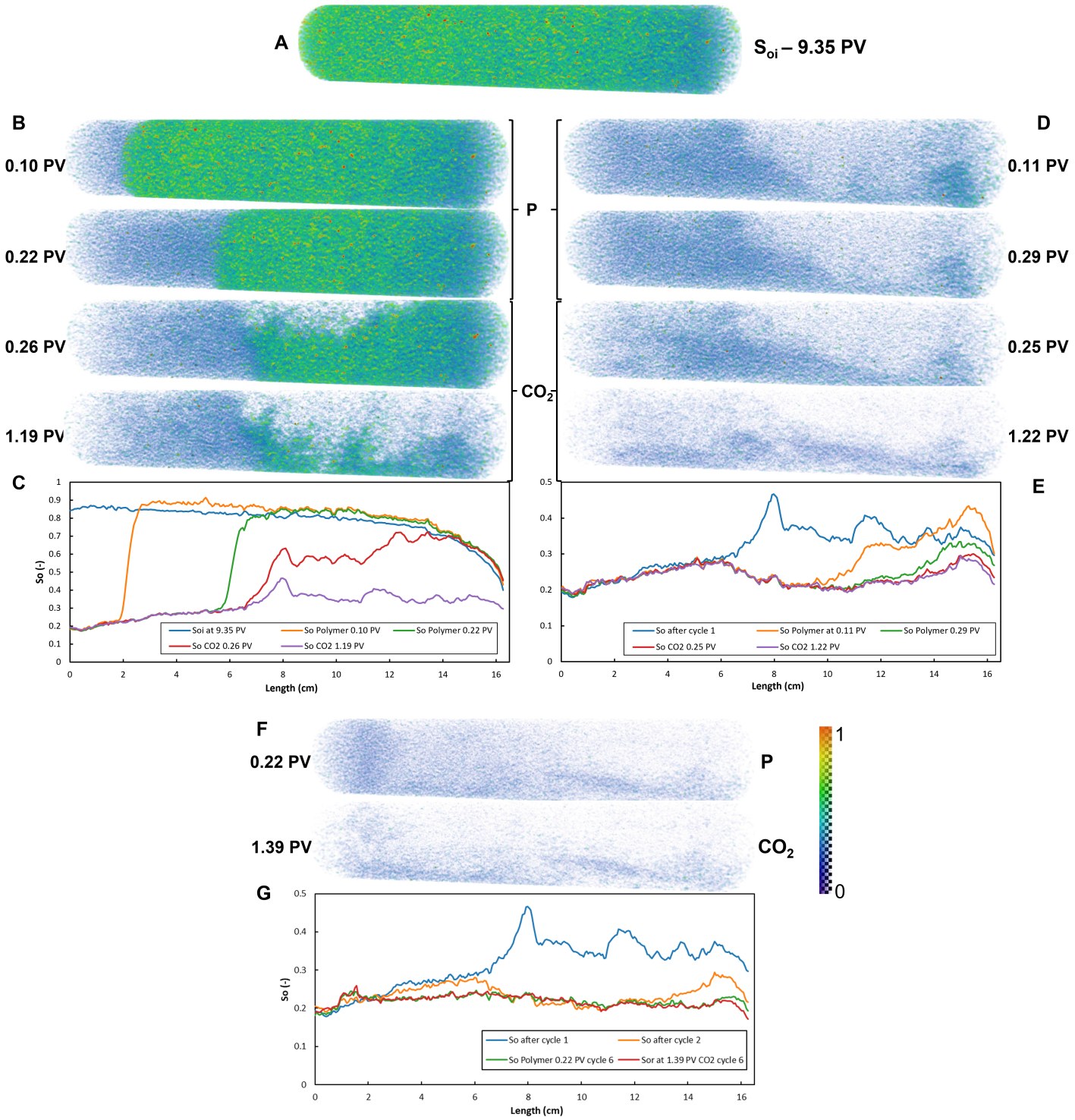

Figure 4.17: For all CT-images: oil phase (blue/green to yellow/orange), brine (light blue/white), CO_2 (white). (A) S_{oi} of 78.1 $\pm$ 3.1% after 9.35 $\pm$ 0.03 PV of primary drainage. P=O refers to the start of injection of the presented cycle. (B) First PA-WAG cycle CT-images, with the polymer slug injection in the first two images and the CO_2 in the second two. Both polymer and CO_2 are injected from the left and oil is produced at the right side of the core. The polymer displacement of the oil shows a stable front, whereas the CO_2 shows clear gravity segregation by flowing over the top of the polymer slug and displacing the oil in the second half of the core, leaving a large part of the bottom and middle section of the core unswept by CO_2. (C) S_o profile during the first PA-WAG cycle, matching the presented scans above. $S_{or,cycle1} = 28.9 \pm 3.1\%$. (D) Second PA-WAG cycle CT-images, same order in scans presented as the first cycle. Small changes in saturation for mainly the second half of the core during full polymer slug injection are noticeable. After CO_2 injection, a small section of the bottom of the core remains unswept. (D) S_o profile over the course of the second cycle, corresponding to the CT-images. $S_{or,cycle2} = 14.1 \pm 3.1\%$. (E) Full PA-WAG injection scheme completed with cycle 6. Most of the core appears to be swept, with only a small section of bottom part of the core unswept (very first section has a slightly higher saturation due to the remaining polymer). (F) With cycle 3 to the full PA-WAG, only a 2.8% decrease in S_o, resulting in a S_{or} of 11.3 $\pm$ 3.1% for the full PA-WAG.

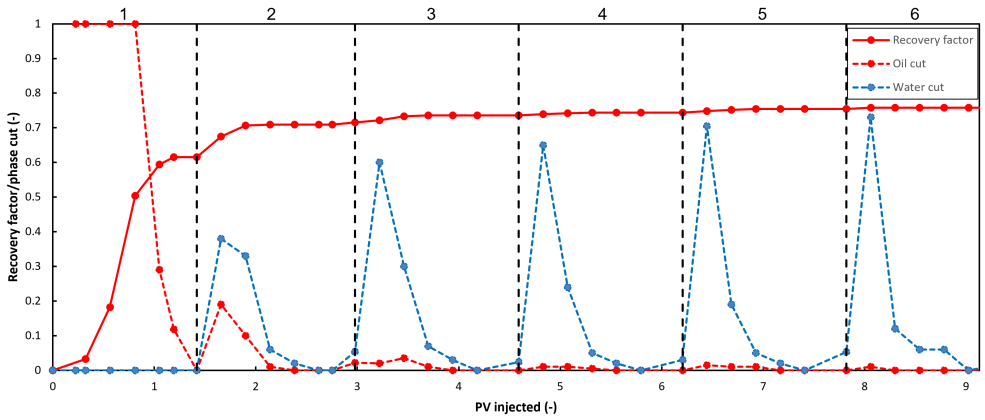

(a)

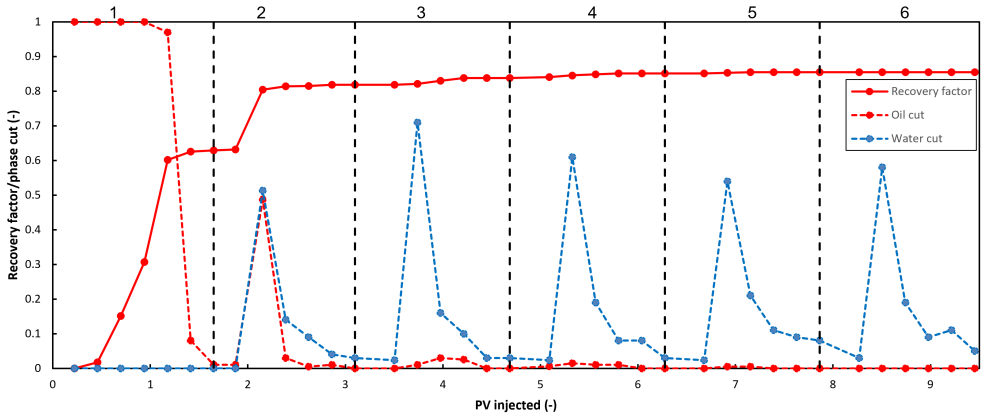

(b)

Figure 4.18: (a) Recovery factor achieved by WAG injection, with the corresponding oil and water cut. A total recovery of 75.8 $\pm$ 3.1% of the OIIP is established over the course of six cycles of brine and CO_2 slugs, from which 94% was recovered in the first two cycles. The cycles are numbered above the graph. (b) Recovery factor achieved by PA-WAG injection, with the corresponding oil and water cut. A total recovery of 85.5 $\pm$ 3.1% of the OIIP is established over the course of six cycles of polymer and CO_2 slugs, from which 96% was recovered in the first two cycles. The cycles are numbered above the graph.

4.3.5. Core-flood at reservoir conditions in Indiana limestone

Primary drainage

Table 4.6: Main results of the primary drainage for the Indiana limestone core with crude oil prior to the PA-WAG recovery injection.

Breakhthrough (PV)	S_{oi}	S_{wc}	OIIP (mL)	k^e_{ro}
0.43 $\pm$ 0.03	0.50 $\pm$ 0.03	0.50 $\pm$ 0.03	18.1 $\pm$ 1.3	0.73 $\pm$ 0.05

The primary drainage for the experiment performed with an Indiana limestone is slightly different than stated in subsection 4.3.1. In this experiment, the oleic phase and core type were altered to a crude oil in combination with an Indiana limestone core. The pressure data results and saturation profile with accompanying CT-scan will be shortly presented below, starting with the pressure drop data. The results can be found in Table 4.6.

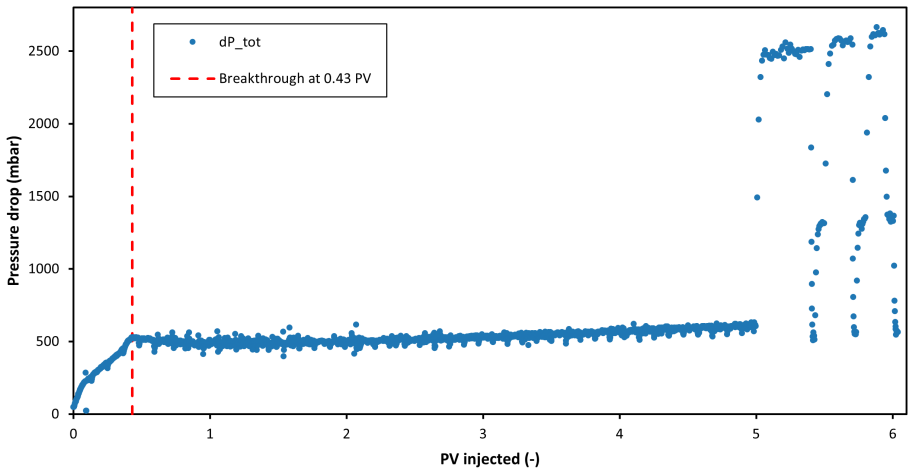

Figure 4.19: Pressure drop profile for the primary drainage, using a crude oil for the saturation of an Indiana limestone core. Breakthrough occurred at 0.43 $\pm$ 0.03 PV, to which the pressure increased from the capillary entry pressure drop of 50 $\pm$ 3 mbar to 529 $\pm$ 5mbar.

In Figure 4.19, the pressure drop profile for the primary drainage is presented. The profile is that of a simple displacement of water by oil, as was the profile shown in subsection 4.3.1. With the use of the crude oil, that has a higher viscosity compared to the previously used n-hexadecane (6.96 $\pm$ 0.03 cP and 2.26 $\pm$ 0.02 cP, respectively), and the Indiana limestone core, with a lower permeability (0.24 $\pm$ 0.009 D and 2.66 $\pm$ 0.10 D, respectively). From the capillary entry pressure drop of 50 $\pm$ 3 mbar, the pressure steadily increased to a pressure drop at the breakthrough at 0.43 $\pm$ 0.03 PV of 529 $\pm$ 5 mbar. After the breakthrough, the pressure drop first decreased and started fluctuating slightly, after which it increased steadily once more. At approximately 5 PV injected of the crude oil, the steady-state pressure was not reached. However, the bump flood was executed for almost 1 PV, followed by two relative endpoint permeability tests for the oil. The general results from the primary drainage can be found in Table 4.6.

Figure 4.20 illustrates the saturation developments just before and during primary drainage with crude oil in Indiana limestone. The Indiana limestone core caries more heterogeneity with it than the previously used Bentheimer sandstone, already visible in the illustrations of the dry and wet core (wet core is a brine saturated core, see Appendix I). The more dense, probably less permeable sections, are detectable by there high intensity colors, which remain the same during the primary drainage. The core scan before breakthrough of the oil shows the almost piston like behaviour of the oil displacing the water in the core, also visualized with the S_o plot in Figure 4.20B. Noticeable is that the S_{oi} from the CT-scan is visible lower than previously achieved in the Bentheimer experiments. This is in line with the lower saturation retrieved from the volumetric balance. Lastly, the capillary end effect is much less apparent. The capillary end effect is the holdup of preferentially the wetting phase at the outlet of a porous medium [50]. The wettability of the Indiana limestone is less water-wet than the Bentheimer sandstone, displaying a smaller capillary end effect were the wetting phase (water) is hold up at the outlet.

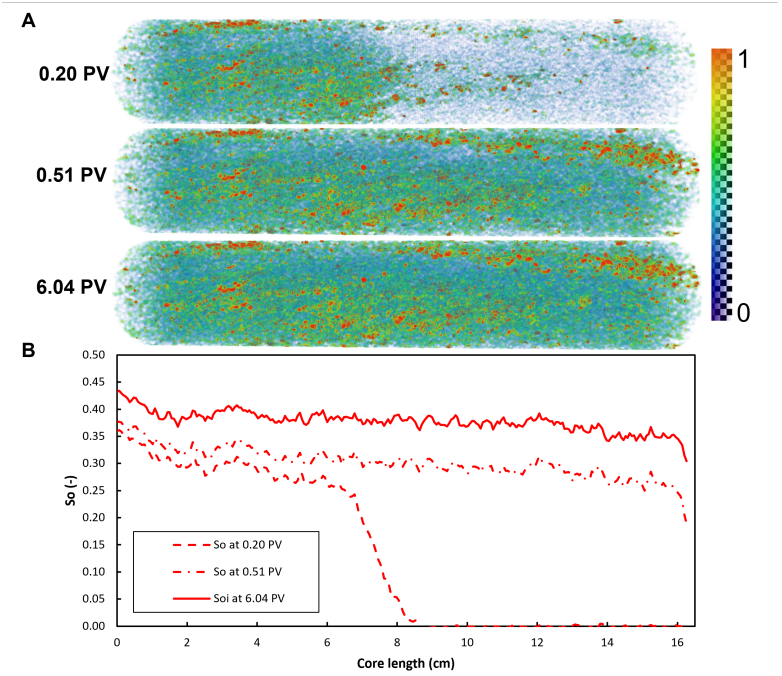

Figure 4.20: Displacement profile of the oil during primary drainage with crude oil with (A) CT images and (B) oil saturation profile. PV=0 refers to the start of oil injection. (A) The oil phase (blue/green to yellow/orange) is being injected from the left side into the core, displacing the brine (light blue/white). With increasing PV injected, the S_o increases likewise towards S_{oi}. (B) Profile of S_o presenting the primary drainage injection phase at different moment in terms of PV of oil injected. The oil front can be traced back to the piston like displacement visible in the CT-images above. As the number of PV injected increase, the average S_o increases accordingly until the S_{oi} is reached.

Pressure drop

Figure 4.21 presents the total pressure drop profile during the PA-WAG injection for oil recovery from the Indiana limestone core. The cycles of the PA-WAG started with the injection of the polymer slug at 2 cm^3/min, followed by the injection of the CO_2 slug at 0.5 cm^3/min. This cycle of the aqueous phase followed by the gaseous phase was repeated six times to complete the full injection scheme. During the injection of the first polymer slug, the pressure drop increased from the capillary entry pressure of 2250 $\pm$ 10 mbar to a minimum of 6950 $\pm$ 10 mbar. This is due to the fact that the upper limit of the differential pressure transducer for the largest, middle section of the core was reached. Estimations on the maximum reached pressure drop would be roughly 11 times higher, following the 1D Darcy's law (Equation 4.1), than what was reached during the PA-WAG experiment in Bentheimer sandstone (subsection 4.3.4), as the permeability of the Indiana limestone core is roughly 11 times lower than for the Bentheimer sandstone core (Table 3.4). Switching to CO_2 injection for the first cycle, the pressure drop sharply declined to 492 $\pm$ 5 mbar. The breakthrough of the CO_2 was recorded shortly after the switch at 0.10 $\pm$ 0.03 PV of solely CO_2 injected (0.32 $\pm$ 0.03 of cumulative injected volumes). The breakthrough was accompanied with the maximum pressured drop reached with CO_2 in the first cycle, namely 2140 $\pm$ 10 mbar. This breakthrough of CO_2 was confirmed by CT-scan data from the core outlet. After breakthrough, the pressure drop decreased and reached the steady-state pressure trend of 185 $\pm$ 30 mbar just before the start of the second cycle with the second polymer slug. During the final stages of the injection of the first CO_2 slug, the breakthrough of the polymer was established at 1.35 PV (0.22 PV of only polymer was injected at this stage).

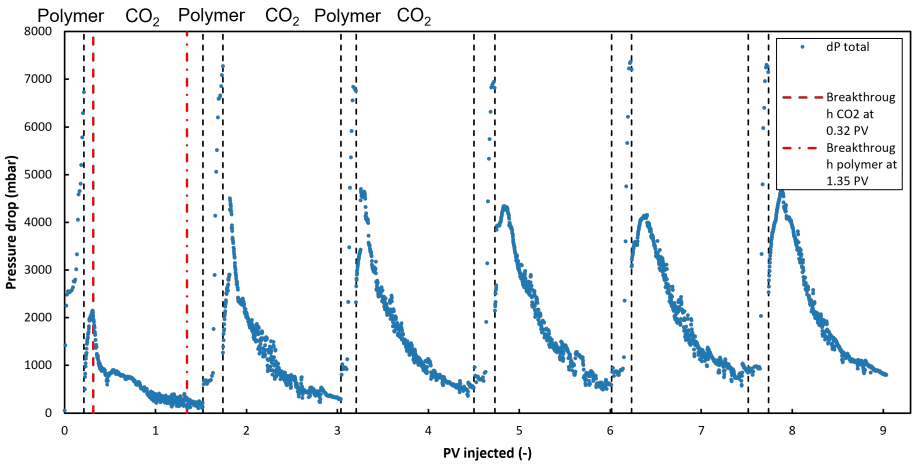

Figure 4.21: PA-WAG pressure profile in Indiana limestone, illustrating the characteristic pressure drop behaviour of injecting a PA-WAG-scheme with different slug sizes and injection rates for the polymer (0.22 PV at 2 cm^3/min) and CO_2 phase (1.3 PV at 0.5 cm^3/min). CO_2 breakthrough occurred at 0.10 $\pm$ 0.03 PV of only CO_2 injected and 0.32 $\pm$ 0.03 PV in total injected PV. At several occasions, the differential pressure transducers reached the upper limit, therefore no correct pressure drop measurement results can be interpreted from during those small peaks. The polymer breakthrough was established at 0.22 $\pm$ 0.03 PV of polymer injected and 1.35 $\pm$ 0.03 PV in total.

With the injection of the second polymer slug for the next cycle of the PA-WAG, the pressure drop profile followed the same trend as for cycle one and the second cycle of the PA-WAG experiment in Bentheimer sandstone (subsection 4.3.4): a lower capillary entry pressure, from which a sharp increase in pressure drop developed until a higher maximum than for the previous cycle was reached, following the same explanation with Equation 4.2. To be noted, in this cycle, both the differential pressure transducers for the first and second section of the core reached their upper limit. With the switch back to CO_2, again an abrupt decline in pressure drop occurred with a successive sharp increase. This profile of the second cycle is repeated in the subsequent cycles. A general decreasing trend of the maximum pressure drop reached at the beginning of the CO_2 slug injection is visible, in contradiction with the PA-WAG in Bentheimer, where a general increasing trend was observed. For the steady-state pressure drop, a general increase over the cycles from 185 $\pm$ 30 mbar to 797 $\pm$ 10 mbar, in agreement with the previous PA-WAG experiment and most probably due to the presence of S_{gt} and an enlarged S_w. The overall trend for the maximum pressure drop the polymer slug reached can not be stated, as likewise one or more differential pressure transducer reached their upper limits in those cycles. The results from the pressure drop data can be seen in Table 4.5.

Table 4.7: The main results from the pressure drop data for the PA-WAG recovery on a Indiana limestone core at reservoir conditions.

Breakthrough aqueous phase (PV)	Breakthrough CO_2 (PV)
0.22 $\pm$ 0.03	0.10 $\pm$ 0.03

Oil saturation profile supported with CT-imaging

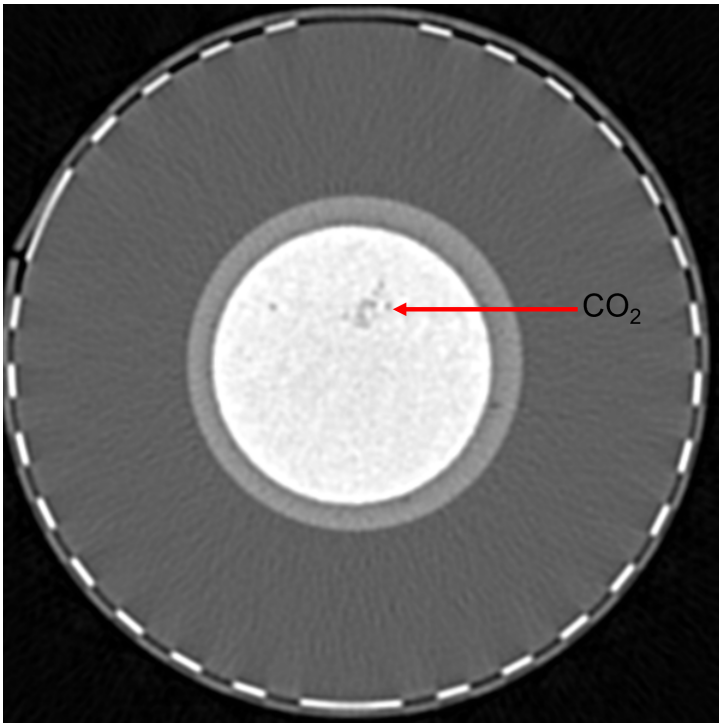

Figure 4.22: Advanced fingering of CO_2 through the core at the early stages of CO_2 injection of the first cycle at 0.05 $\pm$ 0.03, just before breakthrough at 0.10 $\pm$ 0.03, at approximately 1 cm before the outlet of the core.

The CT-scans with the corresponding S_o profiles over the course of the PA-WAG injection for oil recovery from the Indiana limestone core are presented in Figure 4.24. Due to the 80 kV scans exceeding the upper HU limit of the CT-scanner and without the option to recover the scan on an extended HU scale, the S_o for this experiment was not computed with the three-phase system equations from Equation 3.5.4. Based solely on the the changes in HU readings between from the 140 kV scan of the concerned scan during the PA-WAG cycles and the S_{oi}, it was achieved to still approach the S_o with the use of percentage wise calibration using the changes in HU and S_o from previous experiments. These achieved S_o profiles are merely to give a global insight into the changes in saturation along the core during the injection steps. For the first cycle, the produced approximations of the S_o during the presented scans are in line with the expectations derived from the WAG and PA-WAG experiment from Table 4.3.4 and the visual representation of the displacement in the scans. For the second cycle and final cycle, only the start and end S_o approximations are used, as the intermediate profiles failed to give a re-presentable insight Second aspect to be noted: during the scan at 0.22 PV polymer injection first cycle (Figure 4.24B), the scanner had only retrieved half of the core with scanning. There was no possibility to recover the full scan.

During the injection of the first polymer, the displacement front of the polymer and the oil is visible and fairly stable. In the scans of Figure 4.24B, it can be seen that after the first polymer slug, some sections of the more heterogeneous limestone are better swept than others leaving sections with a higher remaining saturation. These sections were also already present in the wet scan, making their content presumably not oil. With the switch to CO_2 flooding for the first cycle, the polymer front has slightly advanced in the scan 0.05 $\pm$ 0.03 PV (just before breakthrough at 0.10 $\pm$ 0.03 PV). This advancement is also visible in the corresponding S_o profile of Figure 4.24B'. Besides this displacement of oil, no other striking change in oil displacement is noticeable in either the scans or S_o profile in Figure 4.24B & B', respectively, only that the overall saturation is slightly lower for the first half of the core which was previously only occupied with polymer. Individual slices of the CT-scans made clear that the CO_2 already fingered a long way through higher permeable sections of the core to $\pm$ 1 cm before the outlet at this stage of injection (see Figure 4.22). At the end of the first cycle, the CO_2 also displaced the still present at the later part of the core at the early stages of the CO_2 slug injection and overall S_o is further

decreased, resulting in a $S_{or,cycle1}$ of 23.5 $\pm$ 4.1%.

The second cycle polymer slug injection shows not a noticeable change in S_o on the scans from Figure 4.24C. The start of the CO_2 injection shows the lowering of the saturation, mostly at the top half of the core, and over the course of the full injection of the CO_2 slug, most of the core's overall saturation has been lowered. Nevertheless, small patches of higher saturation remain scattered across the core, put as earlier mentioned most probable not containing amounts of oil. The S_o profile in Figure 4.24C' indicates a fairly constant decrease of saturation over the length of the core. At this stage of the recovery, a $S_{or,cycle2}$ of 18.5 $\pm$ 3.6% is achieved.

Over the course of the remaining four cycles of PA-WAG injection, only minimal decline in S_o reduction is visible and a slightly higher S_o at the beginning of the core remains fairly untouched since the second cycle. An additional lowering of the S_o of only 6.2% was achieved through those four cycles, resulting in a S_{or} of 12.3 $\pm$ 4.1%. Some small patches of high saturation do however still remain, and seemingly untouched from the beginning of the PA-WAG injection.

Oil recovery factor

In Figure 4.23, the recovery factor development over the course of the PA-WAG injection for the coreflood experiment at reservoir conditions and using an Indiana limestone core. The recovery during the first cycle is comparable to the WAG and PA-WAG experiments performed on a Bentheimer sandstone core (Figure 4.3.4), but slightly lower. Where the WAG and PA-WAG on a Bentheimer core achieved over the first cycle 83 and 73% of their total recovery, the PA-WAG injection on the Indiana limestone core established 70% of the total recovery. This translates to a recovery factor of 0.53 $\pm$ 0.04 after cycle one. The second cycle of the PA-WAG results in a 10% incremental increase in recovery factor to 0.63 $\pm$ 0.04, which translates to 83.5% of the total recovery. The produced volumes of oil from the second cycle onward are always just before or coinciding with the production of polymer. The production of polymer is very comparable to the aqueous phase cut in the PA-WAG experiment conducted in Bentheimer sandstone (Figure 4.18b). After polymer is also produced from the outlet, emulsions were also found in the effluent.

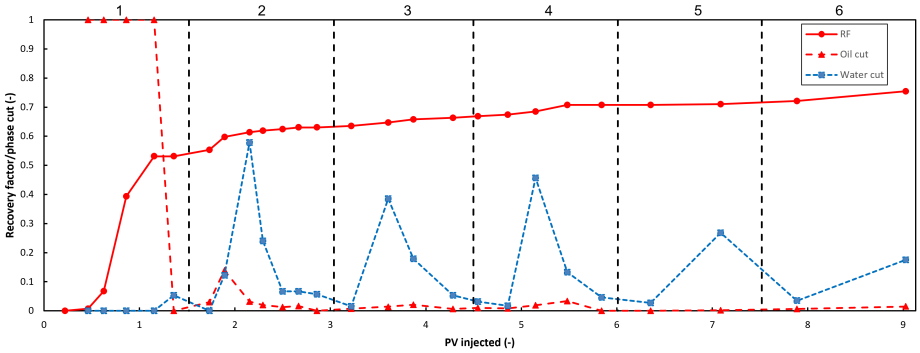

Figure 4.23: Representation of the recovery factor over the course of the experiment PA-WAG flooding in and Indiana limestone core saturated with crude oil. A total recovery over the full six cycles of 75.5 $\pm$ 4.1% of the OIIP is achieved. 83.6% of this total recovery is recovered over the course of the first two cycles.

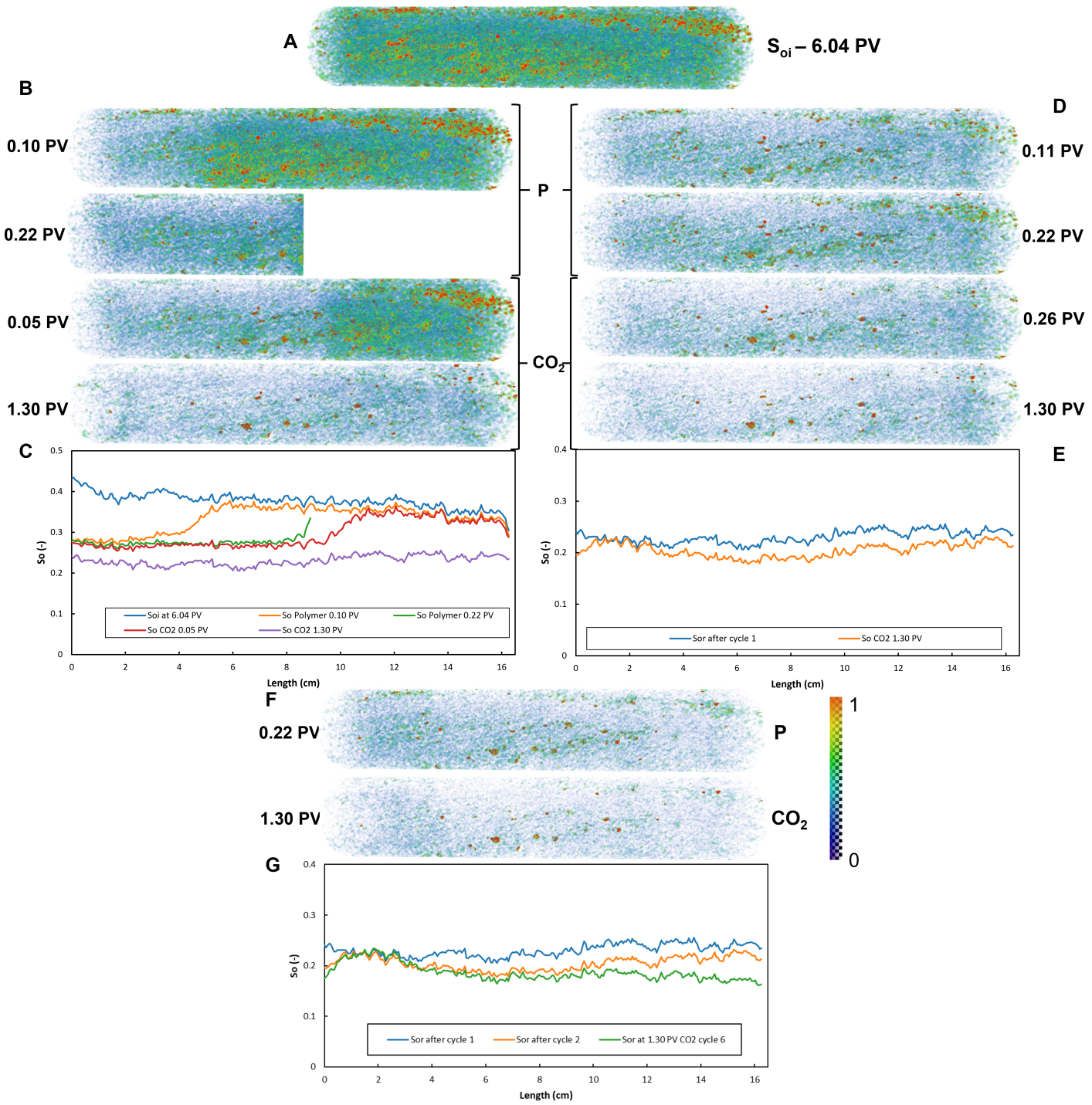

Figure 4.24: For all CT-images: oil phase (blue/green to yellow/orange), brine (light blue/white), CO_2 (white). P=0 refers to the start of the presented cycle of the PA-WAG. (A) S_{oi} of 50.2 $\pm$ 3.1% after 6.04 $\pm$ 0.03 PV of primary drainage. (B) First PA-WAG cycle CT-images, with the polymer slug injection in the first two images and the CO_2 in the second two. Both polymer and CO_2 are injected from the left and oil is produced at the right side of the core. The heterogeneity of the core is visible in terms of the spread in S_o. The polymer front shows a fairly stable front, but leaves some areas with higher intensities unswept. Only half of the 0.22 PV scan is available. The CO_2 slug slightly advances the polymer front and over total injection, lowers the overall S_o. (C) S_o profile during the first PA-WAG cycle, matching the presented scans above. $S_{or,cycle1} = 23.5 \pm 4.1\%$. (D) Second PA-WAG cycle CT-images, same order in scans presented as the first cycle. No real changes visible during polymer slug injection. After CO_2 injection, the overall saturation of the core is visible lower. Some small patches of higher intensity remain untouched. (E) S_o profile over the course of the second cycle, corresponding to the CT-images. Only the end of the cycles S_o profile is presented. $S_{or,cycle2} = 18.5 \pm 4.1\%$. (F) Full PA-WAG injection scheme completed with cycle 6. Most of the core appears to be swept. Small bump of oil remains at the start of the core and some small patches of high saturation still untouched. (G) Remaining four cycles only decrease S_o with 6.2%, resulting in a S_{or} of 12.3 $\pm$ 4.1% for the full PA-WAG.

4.4. General discussion

In this section, the results from the performed experiments are in detail discussed with respect to the research questions and objectives stated in section 1.3. The core-flood experiments will be discussed towards displacement and recovery improvements from PA-WAG over WAG, after which the polymer and CO_2 interaction is addressed from the polymer degradation experiment.

4.4.1. Core-flood experiments

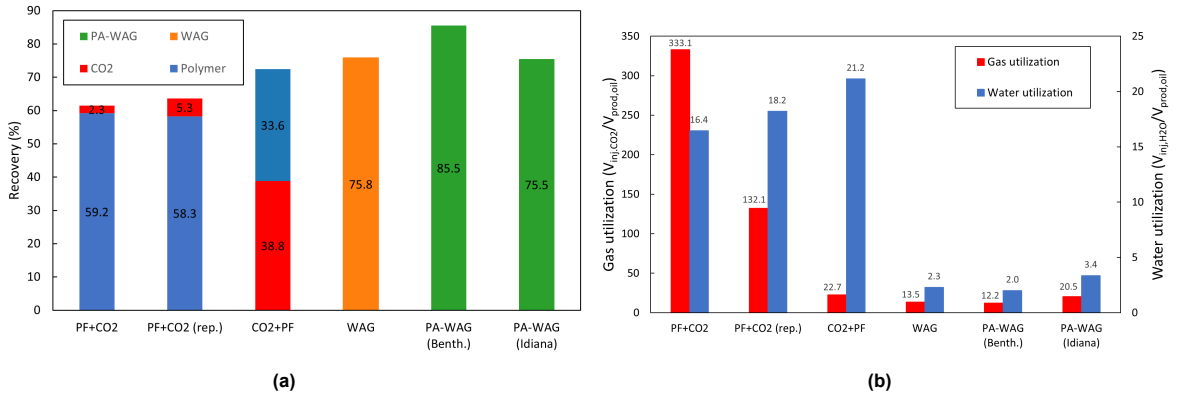

Figure 4.25: (a) Comparison of the recovery factors of the six core-flood experiments carried out in this research showing the increasing trend of total recovery towards the PA-WAG method.Comparison of the utilization factors for the six different core-flood experiments carried out in this study. (b) The utilization factor is defined as the volume of the displacing phase injected over the volume of oil produced.

Figure 4.25a gives an overview of the recovery factors from the production during the different stages of injection for the six performed core-flood experiments. This displays the increase in recovery of the OIIP, using firstly polymer as a secondary recovery and CO_2 as a tertiary recovery, then CO_2 as secondary and polymer as tertiary and lastly WAG and PA-WAG methods. Using CO_2 after polymer flooding as a tertiary recovery method, the incremental recovery is very limited, resulting in very high utilization factors (utilization = $\frac{V_{cum.inj.phase}}{V_{cum.prod.oil}}$). The large volumes of polymer required to recover the high amounts of oil in during secondary recovery result in considerable high utilization for the aqueous phase. Switching the two injection methods, the polymer establishes a high incremental recovery, due to the higher levels of OIP (oil in place) remaining in the core and the effect of CO_2 dissolution in the oil from the secondary recovery injection (subsection 4.3.3). The levels of recovery with polymer are however lower for the tertiary injection than when used as secondary, resulting in a higher utilization factor in this experiment. Going forward with the WAG injection, slight increase in total recovery is established over the experiment using secondary CO_2 flooding and tertiary polymer flooding. The injection uses the sweep efficiency from both phases since the beginning stages of the recovery. With this injection, the utilization factor of both CO_2 and aqueous phase have dropped considerably, especially in the usage of the aqueous phase with respect to previous two experiments. By the addition of polymer to this aqueous phase, the oil recovery was increased by almost 10% over the WAG experiment, while reducing the utilization of the two injected phases slightly. Both the WAG and PA-WAG experiment in Bentheimer sandstone started with similar initial conditions, having both a permeability of 2.7 $\pm$ 0.1 Darcy and S_{oi} of 0.78 $\pm$ 0.03. With Figure 4.26, the recovery of the WAG and PA-WAG experiment in Bentheimer sandstone are discussed side by side.

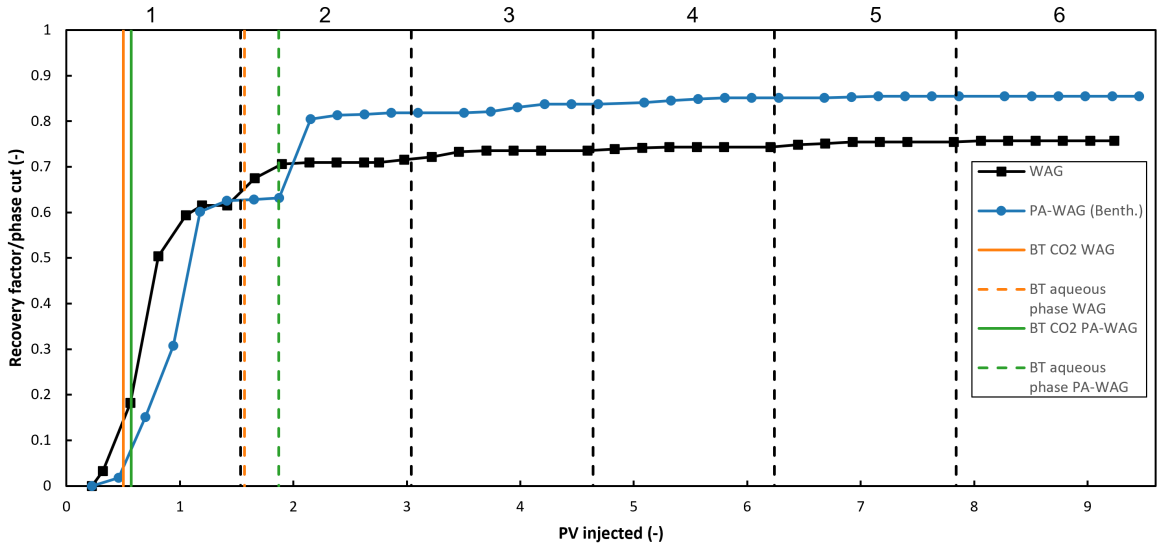

Figure 4.26: Recovery factor development during the six cycles, numbered above the graph, of the WAG and PA-WAG injection on Bentheimer sandstone cores. The comparison of breakthrough times in terms of PV with respect to the impact in recovery can be seen as well in the graph.

The polymer addition with using the PA-WAG over the WAG method was to establish better mobility control, reduce gravity segregation and viscous fingering, thereby improving the sweep efficiency and ultimately the oil recovery [30, 32, 64, 63]. According to studies, the viscous fingering is the unstable displacement of a more viscous fluid by an injected, less viscous fluid [10]. Comparing theoretically the WAG and PA-WAG injection, the difference in viscosity between polymer and CO_2 is much larger than brine and CO_2. This implies that CO_2 is more prone to viscous fingering during PA-WAG injection than during WAG injection. But with the addition of the polymer going from WAG to PA-WAG injection in this study, the breakthrough of both the aqueous phase and CO_2 were delayed, suggesting that the PA-WAG suffered less from viscous fingering of either the CO_2 and the aqueous phase. The increased viscosity of the aqueous phase created a more favourable displacement of the oil phase, by lowering the mobility ratio. With the delay of the aqueous phase, the delay of the oil breakthrough in the second cycle is delayed. This indicates the improved sweep efficiency obtained by the addition of the polymer to the water to increase the viscosity. The improved sweep efficiency is also clearly illustrated by the CT-scans performed during both the WAG and PA-WAG. During the injection of the first CO_2 slug, the polymer front stayed stationary at the position in the core it reached with the polymer slug injection at the start of cycle 1. The brine front during WAG injection however, did not remain stationary and infiltrated the last section of the core. This led to the early breakthrough of brine at the end of the first cycle, while the polymer caused the delay in breakthrough up to the end of the second polymer slug injection by remaining a stationary front during CO_2 injection (see Appendix M for the visualisation of the individual dP sections). Evaluating the visualized displacement in figures 4.16 and 4.17, the PA-WAG recovery injection seems less subjective to gravity segregation. These improvements in viscous fingering, gravity segregation and breakthrough delay of the PA-WAG over the WAG experiment result in a better sweep efficiency and the ultimately higher recovery achieved with the addition of the polymer to the aqueous phase. From Figure 4.26, it can be seen that the recovery increase after the initial recovery from the first cycle is directly related to the breakthrough of the aqueous phase, where the PA-WAG has the edge over the WAG experiment in terms of the incremental recovery from cycle 2. The delay of the breakthrough, as earlier mentioned, resulted in a better sweep of the core after the starting cycle and this effect is clearly visible in the increase in oil recovered at and right after this breakthrough. Comparing the recoveries and percentage of their total final recovery (% RF) of both experiments in terms of achieved per cycle, the big gain of PA-WAG over WAG is illustrated (Table 4.8). Both reach 93.6% and 95.7% of their total recovery by the second cycle, while the first cycle resulted in the virtually the same recovery factors of 0.62 ± 0.03 and 0.63 ± 0.03, respectively. In economically aspects, with two cycles of injection, the PA-WAG reaches already 96% of the recovery, translating

81.8 $\pm$ 3.1% of the OIIP recovered. This is achieved with utilization factors for polymer and CO_2 of only 0.70 and 4.16 (0.82 and 4.21 for WAG), respectively, compared to the ultimate utilization of 2.0 and 12.2 (2.3 and 13.5 for WAG). The reduction of both the utilization factors will result in more financially beneficial explorations. The decrease of the CO_2 utilization is especially important for the profitability of offshore projects and regions with limited CO_2 supply, where costs are high for the capture, transport and on-site storage of the CO_2 while maintaining appropriate purity [33].

Table 4.8: The recovery factor progression compared per cycle between the WAG and PA-WAG experiment in Bentheimer sandstone, as well as the % of total recovery (% RF).

	Cycle 1		Cycle 2		Cycle 3		Cycle 4		Cycle 5		Cycle 6		Error
	RF	% RF	RF	% RF	RF	% RF	RF	% RF	RF	% RF	RF	% RF	
WAG	0.62	81.3	0.71	93.6	0.74	97.1	0.74	98.1	0.75	99.6	0.76	100.0	0.03
PA-WAG (Bent.)	0.63	73.6	0.82	95.7	0.84	98.0	0.85	99.6	0.85	100.0	0.85	100.0	0.03

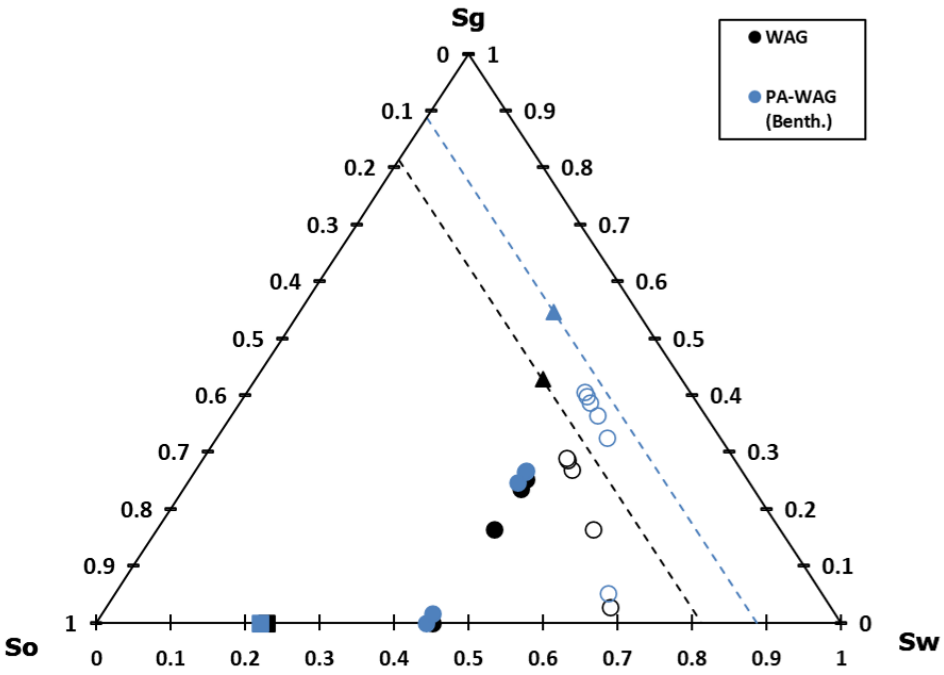

Figure 4.27: The saturation path presented as ternary saturation diagram for the WAG and PA-WAG experiment in Bentheimer sandstone. The three-phase saturation of the core were averaged over the entire core length by volumetric material balance calculations. The closed squares indicate the S_{oi} conditions for both experiments. The closed and open circles represent the first and second cycle of injection for WAG and Pa-WAG, respectively. The closed triangles give the achieved S_or, also represented by the corresponding dashed lines.

Via volumetric material balance calculations, the saturation paths are presented as averaged phase saturation over the entirety of the core and used to discuss in more detail the displacement of oil during WAG and PA-WAG injections. With the WAG injection method, and therefore also in the PA-WAG injection, the aqueous phase is used to increase S_w in the core in order to lower the relative permeability to CO_2. The process gives a better mobility control of CO_2, with the potential to reduce viscous fingering, early breakthrough and increase sweep efficiency [33, 32, 47, 20, 1, 54]. By the water injection before the gas injection, amounts of mobile gas are trapped and become immobile. This trapped, non-wetting gas does not contribute to the mobility of the newly injected gas in subsequent injected cycles, and right before the gas injection, water injection as the wetting phase increases the amounts of trapped gas and therefore further reducing the mobility of the in-situ gas. The reduction of the overall gas mobility improves the volumetric sweep efficiency of the CO_2 injected. This increase in trapped gas can be derived from the increased S_g after CO_2 injection of the cycle, increase in remaining S_g over the

course of more cycles (see Figure 4.27) and the pressure drop spikes presented in subsection 4.3.4 [47, 20].

Besides the reduction of the CO_2 mobility with increased S_w by the injection of the aqueous phase during WAG and PA-WAG, the gravity segregation by the density difference between the aqueous phase and the oil phase and between CO_2 and oil is used to improve vertical sweep efficiency. The CO_2, with the lighter density than oil displaces the attic oil at the top of the core and the denser aqueous phase displacing the basement oil at the bottom of the core. This gravity segregation improves the vertical sweep efficiency, which are controlled by viscous and gravity forces. These contribution forces can be given as the viscous/gravity dimensionless number [1]:

$$R_{v/g} = (\frac{\nu\eta_o}{k_o g\Delta\rho}(\frac{L}{h}) \tag{4.3}$$

, where ν is the Darcy velocity, η_o is the oil viscosity, L is the core length, k_o is the effective oil permeability, g denotes the gravitational acceleration, $\Delta\rho$ is the density difference between the fluids, and h represents the height of displacement zone. By the injection of both CO_2 and aqueous phase, displacement height h is increased. This lowers the ratio of viscous to gravitational forces, leading to a improved vertical sweep efficiency and corresponding increase in recovery [1].

The addition of polymer to the aqueous phase also increases the viscosity significantly of the wetting-phase. Besides the above stated improved vertical sweep due to the benefits regarding gravity segregation, the increase in η_w in PA-WAG over WAG results in a lowered mobility ratio (Equation 2.1) for the former over the later, causing a more favourable displacement with the aqueous phase.

In the ternary saturation diagram from Figure 4.27, it can be seen that the initial injection of brine and polymer in the first cycle (closed circles) increase the S_w towards virtually the same level. The followed CO_2 slug of the first cycle then increases likewise the S_g levels in the cores to the approximate same levels, while remaining at a constant S_w and achieving the same $S_{or}, cycle1$. The before mentioned edge of PA-WAG over WAG in terms of recovery, mostly noticeable in the second cycle, can also be traced back to the saturation path. With the brine and polymer slugs of the second cycle, the S_w is increased significantly with a remaining S_g in terms of dissolved CO_2 in either the aqueous or oleic phase or S_{gt}. With the second CO_2 slug, the S_g is increased significantly in both cases. But the early breakthrough by the more mobile gas in the WAG experiment causes a lower S_g to be achieved at the end of the second injected cycle, compared to the PA-WAG experiment, while both experiments follow roughly the same path to the remaining S_w at the end of the cycle and therefore a higher recovery of oil with the PA-WAG recovery injection.

After all the experiments performed on Bentheimer sandstone, were the difference in performance between WAG and PA-WAG is clearly highlighted, the PA-WAG method was used for the recovery of crude oil from and Indiana limestone. This core bears much more heterogeneity than the Bentheimer cores, in addition to a much lower permeability (235 mD instead of 1.9 to 2.7 D) and the used crude is much more viscous than the previously used n-hexadecane (6.96 $\pm$ 0.03 cP compared to 2.26 $\pm$ 0.02 cP).

The saturation paths of both PA-WAG experiments are compared and discussed in and using saturation ternary diagram in Figure 4.28. The saturation paths for both experiments are quite comparable, but the Indiana limestone reached only a 50.2 $\pm$ 3.6% s_{oi}, compared to the 78.1 $\pm$ 3.1% for the Bentheimer experiment. Noticeable is that the S_g during the Indiana limestone experiment stays considerably low compared to the other PA-WAG injection, with final S_g of 0.23 compared to 0.41. The breakthrough during the Indiana limestone experiment was as well considerably earlier, implying very mobile CO_2 which mostly bypassed the oil via more permeable sections of the core or via gravity override. In terms of recovery, the PA-WAG injection for the experiment carried out on Indiana limestone was very effective, reaching a total recovery of 75.5 $\pm$ 3.6%. This is achieved with relatively low utilization factors for both CO_2 and polymer. At the end of recovery, both experiment reach almost similar S_{or}. The recovery progression in terms of % of the total recovery, along side the standard recovery factor of the OIIP, is given in Table 4.9. By comparing the second cycle again, the PA-WAG in Indiana limestone only reached 83.6% of the total recovery, indicating that more oil is recovered in the later cycles.

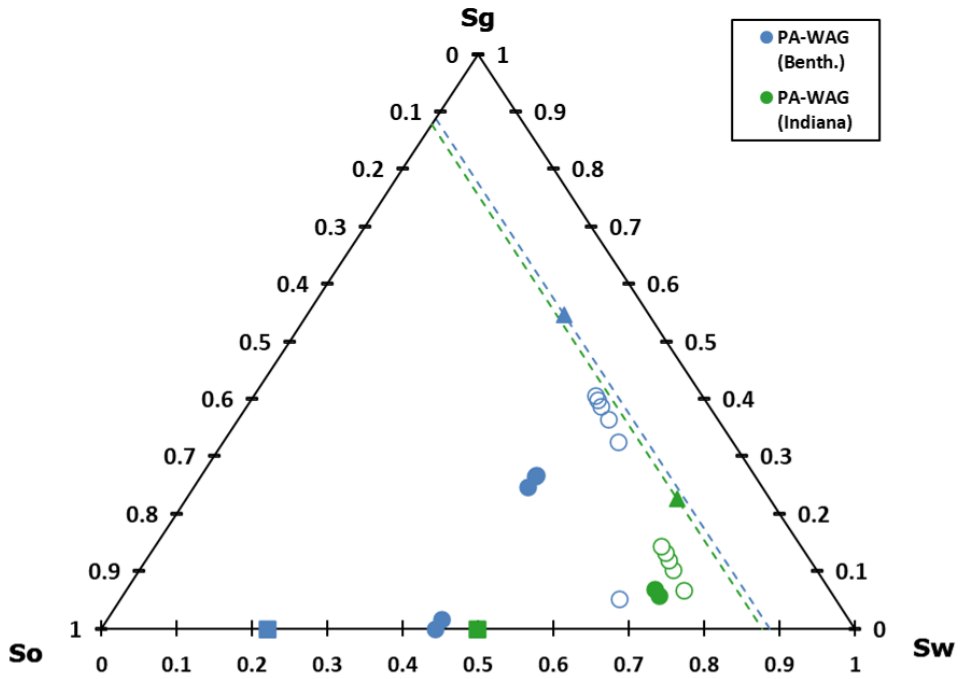

Figure 4.28: The saturation path presented as ternary saturation diagram for the PA-WAG experiments performed on both Bentheimer sandstone and Indiana limestone. The three-phase saturation of the core were averaged over the entire core length by volumetric material balance calculations. The closed squares indicate the S_{oi} conditions for both experiments. The closed and open circles represent the first and second cycle of injection for WAG and Pa-WAG, respectively. The closed triangles give the achieved S_or, also represented by the corresponding dashed lines.

Carbonate rocks host more than 60% of the world's oil reserves. Those reservoirs are mostly oil-wet and display typically recoveries lower than 40%. In oil-wet conditions, the oil sticks to the surface of the reservoir rock and therefore releases this oil less easy from the pore spaces than water-wet systems [4]. Originally, Indiana limestone is water-wet [62]. With aging the Indiana limestone cores in the S_{oi} state, the core becomes more oil-wet over time. In the case of the performed experiment in this study, the core was not aged and is therefore presumably still in water-wet state. Besides not aging the core in contact with the oil phase, the study from Xie et al.(2018)[61] showed that the pH in oil/brine/carbonate systems has a strong effect on the contact angle, indicating that the pH is likely to be a strong controlling factor for the wettability. They found that low pH systems (pH=3) in the presence of Na_2SO_4 and $CaCL_2$ displayed slightly more water-wet systems, while the contact again increased drastically with increasing pH, becoming with that a strongly oil-wet system. With the injection of CO_2, the pH will drop due to formation of carbonic acid (see subsection 2.2.3) and the pH can decrease to levels around 4. This presumably water-wet system for the Indiana limestone during the experiment is probably a high contributor to the considerable recovery achieved with this core-flood.

Table 4.9: The recovery factor progression compared per cycle for the PA-WAG experiment on Indiana limestone using crude oil, as well as the % of total recovery (% RF).

Cycle 1		Cycle 2		Cycle 3		Cycle 4		Cycle 5		Cycle 6		Error
RF	% of RF	RF	% of RF	RF	% of RF	RF	% of RF	RF	% of RF	RF	% of RF	
0.53	70.4	0.63	83.6	0.67	88.7	0.71	93.8	0.72	95.6	0.75	100.0	0.04

4.4.2. CO_2 effects on SAV10-XV polymer

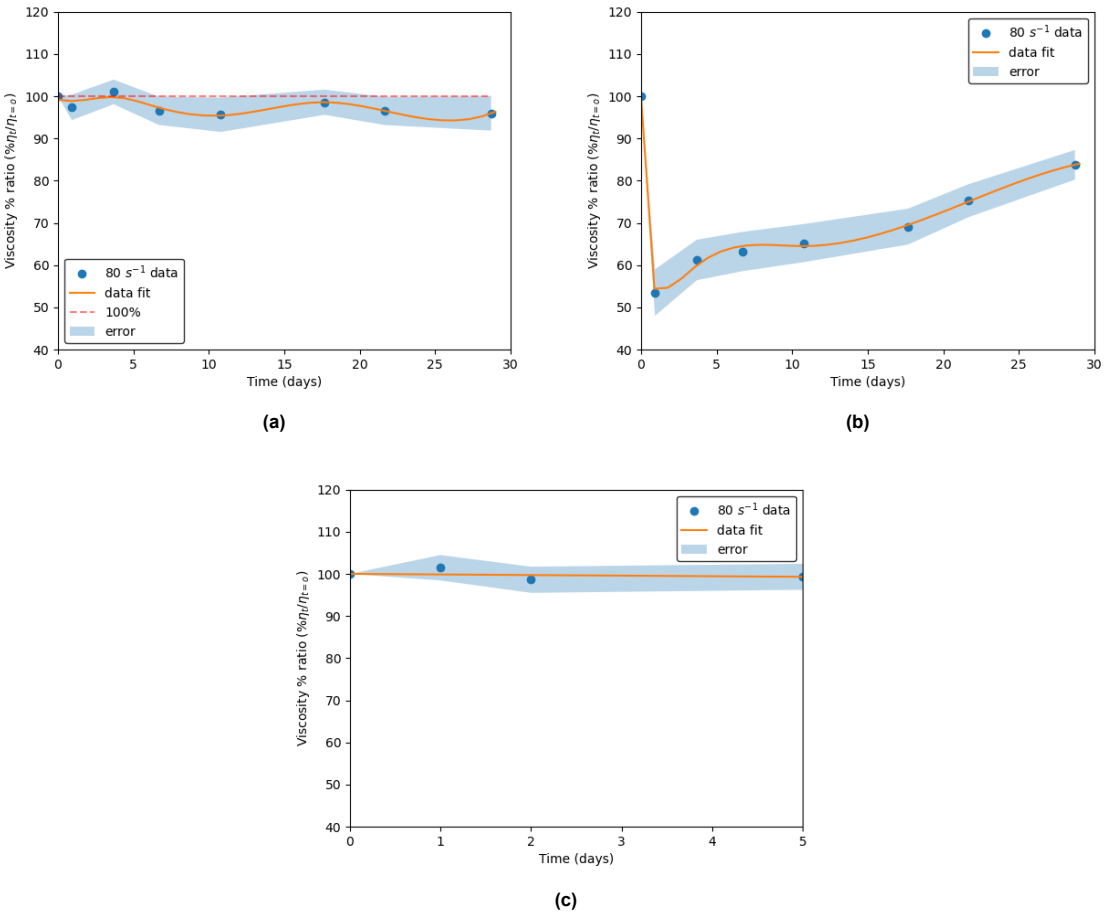

Figure 4.29: Rheometer results at fixed shear rate of 80 s^{-1} for (a) thermal stability for 29 days, (b) stability in presence of CO_2 full saturation for 29 days and (c) stability in presence of CO_2 at PA-WAG injection conditions for 5 days.

In figures 4.29a, 4.29b and 4.29c, the data from the rheometer at the fixed shear rate of 80 s^{-1} is expressed as a percentage of the initial apparent viscosity of the polymer solution (without CO_2). This is done to better acknowledge the changes in the apparent viscosity during the thermal stability experiment (Figure 4.3a), the stability in the presence of CO_2 (Figure 4.3b) and the short term stability test at PA-WAG CO_2 levels (Figure 4.29c). Therefore, the viscosity % ratio ($\eta^{\%}$) is defined as a function of the viscosity of the polymer solution at 80 s^{-1} at any given time during aging (η_t) and the original viscosity of the polymer solution at 80 s^{-1} ($\eta_{t=0}$):

$$\eta^{\%} = 100 * \frac{\eta_t}{\eta_{t=0}} \tag{4.4}$$

80 s^{-1} represents the flow rate used during PA-WAG injection for the polymer. During experiments with polymer flooding as a stand alone flooding technique, either secondary of tertiary mode, the flow is represented at 60 s^{-1}. Appendix J provides the comparison between the viscosity developments at both shear rates. The 80 s^{-1} data points from the rheometer are fitted a best fit model and are presented in figures 4.29a, 4.29b and 4.29c along with their corresponding error margins. The thermal stability experiment over the course of 29 days of injection stayed roughly at the original apparent viscosity, represented by the 100% line in Figure 4.29a, which falls within the error margins of measured apparent viscosity at 80 s^{-1}.

In the presence of CO_2, a rapid decline occurred after the start of the aging process, dropping towards 53.5 $\pm$ 4.5% of the original value of the polymer solution. Since the only difference between

the thermal stability sample and the CO_2 stability sample is the addition of CO_2, the loss in apparent viscosity can be placed under the consequence of the presence of CO_2. The dissolved CO_2 caused the formation of carbonic acid (subsection 2.2.3), decreasing the pH of the fluid towards 4.4 $\pm$ 0.1. With normal HPAM polymer solutions, the acid environment influences the viscosity of the polymer by the neutralization of the charges on the polymer backbone, due to the transformation of the ionic carboxylate groups into non-ionic carboxylic acid groups [54]. But the AMPS modified HPAM SAV-10XV is reported to have excellent viscosity retention with lowered pH (see subsection 2.3.3)[23] and also when this lowered pH is caused by the dissolution of CO_2 (see subsection 2.3.4) [54], especially with the very mildly elevated temperature of 40 °C. Comparing the results with the work of Tovar, Barrufet, and Schechter (2014) [54] (see subsection 2.3.4), the results from Figure 4.29b show a rather different trend for the start of aging. Where Tovar, Barrufet, and Schechter (2014) [54] (aging performed at 50 °C and atmospheric pressure) showed an initial increase of 30% after one day for the PAM-ATBS polymer in the presence of CO_2, followed by a decrease to $\pm$ 64%, the aging experiment performed in this study from Figure 4.29b (40 °C and 15 bar, however measured at atmospheric in the rheometer) presented an initial decrease of 46% after one day. The overall trend in terms of viscosity and pH development represents more the trends of the results presented by Tovar, Barrufet, and Schechter (2014) [54] on HPAM aging in the presence of CO_2, with an initial significant decrease in viscosity and pH, followed by a recovery in viscosity and finally a decrease in viscosity and an increase in pH at the end of testing (see Figure 4.1). Their aging test however stretched over a period of 328 days, whereas the aging experiment from this study only spanned 29 days. It suggests that, within this short period of time, the ATBS modified HPAM polymer SAV-10XV was able to restore the viscosity that was initially lost due to the carbonic acid decreased pH by the hydrolysis of the amide groups. These hydrolysis reaction kinetics can increase under acid conditions [54, 29]. At low pH, neighbouring protonated acrylate elements catalyze further hydrolysis [29]. This hydrolysis resulted in a retention of 83.8 $\pm$ 3.5% at the end of 29 days of aging, which was only achieved after roughly 35 days of aging by Tovar, Barrufet, and Schechter (2014) [54]. The increase of the pH at the end of aging (see Figure 4.1) suggest the evolution of the ammonium ion due to the hydrolysis of the amid groups, which causes the restoration of the apparent viscosity reported in the rheometer data (see figures 4.3b and 4.29b [54]. The apparent viscosity however, correlated from the measured dP over the capillary (Figure 4.2), does not show this recovery in apparent viscosity from day $\pm$ day 4 onward.

After the initial increase, the decrease and followed recovery of apparent viscosity for the PAM-ATBS polymer from the study of Tovar, Barrufet, and Schechter (2014) [54] shows similar values as the ones presented in Figure 4.29b. The aging however is on a shorter time scale (lowest viscosity reached after 1 day instead of approximately 18 and 83.8 $\pm$ 3.5% reached after 29 days instead of $\pm$ 35). This suggest that at the higher pressure and shear rate the aging test is performed, the time frame of the impact of CO_2 presence on the polymer's viscosity is shortened in comparison with the results reported by Tovar, Barrufet, and Schechter (2014) [54]. The initial increase they reported either did not occur or was not captured during the performed aging test in this study. Another cause can be presumed to be in the high levels of CO_2 injected and the aging under pressure during the aging experiment performed in this study. The CO_2 injection was executed until concentrations (0.295 mol/L) that maximized the dissolution of CO_2 into the polymer under the system pressure of 15 bar, in which the polymer was also aged. Tovar, Barrufet, and Schechter (2014) [54] however only aged the polymer in a CO_2 filled environment under atmospheric pressure, which will limited the amount of CO_2 able to dissolve in the polymer significantly.

For the core-flood experiments performed, the total time CO_2 was in contact with the polymer never exceeded 12 hours. Most of the CO_2 and polymer are much less time into contact over the course of the PA-WAG cycles, with in mind that the significant decrease in viscosity was measured after 1 full day, however this was in the experimental case where the polymer was fully saturated with dissolved CO_2. During the experiment with PA-WAG injection in Bentheimer sandstone, the concentration of CO_2 compared to the polymer are estimated to be a factor 11 smaller (0.027 compared to 0.295 mol/L). The stability of the polymer at these molar concentrations of CO_2 was tested and the fixed 80 s^{-1} shear rate data are presented in Figure 4.29c. These much lower amounts of CO_2 dissolving into the polymer resulted in no apparent changes in the viscosity of the polymer, retaining 100% of the original apparent viscosity after 4 days of aging in presence of CO_2.

5
Conclusions and recommendations

The experimental study reported in this thesis provides insights on the performance and displacement mechanisms of the specially designed SAV-10XV for enhancing oil recovery in the form of the polymer assisted water alternating gas injection. This chapter presents the conclusions drawn from this research, followed by the recommendations for future research.

5.0.1. Conclusions

In order to examine the effectiveness of the polymer assisted water alternating gas performance with the use of the ATBS(AMPS)-modified HPAM polymer SAV-10XV in combination with carbon dioxide as an enhanced oil recovery (EOR) technique, an experimental study was followed. This research was conducted at reservoir conditions of 40 $\pm$ 1 °C and 20 bar (15 bar in stability tests) backpressure. The stability of the polymer in combination with CO_2 was studied, in the form of an aging experiment running of approximately one months time, in order to specify the effects of CO_2 on the polymers viscosity retention. With the use of a capillary viscometer and rheometer measurements, this effect was assessed. A series of core-flood experiments at reservoir conditions were performed, with the assistance of a medical CT scanner capable of analysing three phase flow systems by scanning at dual energy levels. During these core-floods, the displacement profiles and efficiencies, along with their performance in terms of recovery, of the different flooding techniques were investigated. The results were used to assess the performance of the SAV-10XV polymer solution in the PA-WAG injection. These experiments included the use of interchanging polymer flooding and CO_2 flooding as secondary and tertiary recovery modes, WAG and PA-WAG injections for the recovery of non-polarised n-hexadecane oil from a Bentheimer sandstone. Lastly, the PA-WAG injection was applied to recover crude oil from a carbonate core, simulation reservoir conditions. The following conclusions can be drawn from this experimental research:

- By applying the different flooding techniques, the achieved recovery factors were calculated to be 61.5 $\pm$ 0.3, 63.9 $\pm$ 0.3, 72.4 $\pm$ 0.3, 75.8 $\pm$ 0.3, 85.5 $\pm$ 0.3 and 75.5 $\pm$ 0.4 of the OIIP for PF+CO_2, PF+CO_2 rep., CO_2 +PF, WAG, PA-WAG and PA-WAG in carbonate with crude oil.
- The PA-WAG injection method for enhancing the oil recovery outperformed the WAG injection in terms of ultimate recovery and displacement efficiency. The addition of the ATBS-modified HPAM polymer SAV-10XV to the brine leaded to:

  1. a reduction of the CO_2 mobility;
  2. more favourable mobility ratio by the highly viscous polymer and decreased gas mobility;
  3. decrease of viscous gingering and gravity override;
  4. delay of both CO_2 and water breakthrough.

  The improvements by the PA-WAG in terms of displacement and sweep efficiency resulted in an $\pm$ 10% incremental recovery over the WAG injection.
- The PA-WAG injection succeeded in lowering the utilization of both CO_2 and water, while significantly improving recoveries. This has great economical potential for oil recovery, especially due to the fact already 96% and 84% (Bentheimer and Indiana experiments, respectively) was recovered by only two injection cycles.
- In contact with CO_2 at fully saturated conditions, the polymer shows viscosity loss due to the acid formation as a consequence of CO_2 dissolution in water. Over time, via the hydrolysis of the polymer, which is catalysed by the acid pH values of the solution by carbonic acid, the polymer

was able to recover from the initial loss to 53.5 $\pm$ 5.5% of the initial viscosity at 80 s^{-1} towards 83.8 $\pm$ 3.5% after 29 days of aging. At lower CO_2 molar concentrations, representing the PA-WAG injection, the polymer shows good stability. It showed no decrease in viscosity with the exposure to the amounts of CO_2, retaining 100% of the initial viscosity after 4 days of aging.

The obtained results are consistent with the hypotheses, found in section 1.3. The polymer is affected by CO_2 at a multistage manner of decreasing and increasing, but at PA-WAG conditions, the impact on the viscosity is minimal. Secondly, an improved recovery and sweep efficiency was achieved with the addition of polymer to the water, creating a polymer assisted water alternating gas EOR injection method.

5.0.2. Recommendations

This thesis provides answers to questions posed at the start of this research and developments along the process, contributing to a better understanding of the effectiveness of the SAV-10XV polymer used in the PA-WAG method for oil recovery. However, some limitations were encountered during the study and several aspects arose that still need some further attention to fill the knowledge gaps. First, the limitations in this study are presented:

- At the start of the experimental core-flood work, a higher flow rate than intended was applied during polymer flooding. This led to the formation of emulsion, which was anticipated before the experiment. The emulsions returned in several latter experiments, which raised some question regarding the effect on the polymer and oil viscosity, polymer retention and sweep efficiency.
- Some doubts about the measured relative permeabilities of CO_2 and polymer during PA-WAG and WAG remain, limiting the possibilities to draw conclusions with numbers on the relative permeabilities of the phases during this injection.
- With the experiment using crude oil in Indiana limestone, the maximum value of the CT scanner was reached during most of the 80 kV scans during dual energy scanning. This was followed by an ineffec- tive transfer tot extended files. Without this 80 kV data, the three phase systems calculations could not be performed properly and therefore, saturation profile analyses was limited for this experiment.
- The aging experiment in the presence of CO_2 was performed for 29 days. A limiting factor here was the lack of a larger transfer vessel, now only capable of holding 2 L maximum. In ideal cases, a longer stability test was more desirable. After the initial stability experiment with fully CO_2 saturated polymer, a new glove bag was used for the preparation of the polymer under oxygen free conditions. This glove bag however showed less quality of material and was not able to hold the vacuum environment applied to it when containing the mixing set-up. Following stability tests were therefore limited to only the addition of the oxygen scavenger to the polymer.

Based on the insights provided by this research, the following recommendations are made for future research to consider:

- Use the experimental data in modelling work. This will allow to test under variable conditions in shorter time periods.
- For future PA-WAG injections, it is advised to use an inlet cap without a shared line for the two phases. In this way, the the phases have their own, direct core inlet without displacing any other fluid present in the line after switch. The difficulty of the PA-WAG injection (and WAG as well) will drop considerable, without the addition of incorporating the lag from the lines being filled with different phases, while injecting at changed flow rates every slug and also switching from fluid phase injected and planning scans without much time in between.
- Performing an analysis of the optimal slug size, as the slug size used in this study is retrieved from the study of Janssen (2020) [20], which was optimised for the WAG injection.
- In Indiana limestone, only a PA-WAG injection method for the recovery of the crude oil from a not oil aged carbonate core was executed in this study. For comparisons, it is advised to also perform a WAG injection alongside the PA-WAG and perform both also under aged in crude oil conditions for the Indiana limestone core.

- It is advised to perform interfacial tension (IFT) measurements. The IFT's can give an insight on the spreading coefficient of the three-phase system during PA-WAG and WAG injections. The spreading coefficient would help to better understand the oil recovery mechanisms and potentials
- Performing the PA-WAG experiment under gravity stable conditions. This will eliminate the gravity segregation. In the TU Delft reservoir engineering laboratory, this would mean the core-flood is executed without the aid of CT-scanning.
- Using different set-up or materials to ensure the oxygen free environment needed for preparing the polymer for stability testing. The newly order glove bag proved to be of insufficient quality in order to proceed with preparations and the method of using a glove bag showed to be very unpractical to work with due to the limited moving space the bag allows.
- Implementing the polymer on CO_2 and hydrogen storage studies, as the polymer has shown very promising results in terms of oil recovery and displacement efficiency improvements with the use of CO_2 . In that way, the polymer and the research can contribute to other challenging but necessary research in the future.

References

[1] Shokufe Afzali, Nima Rezaei, and Sohrab Zendehboudi. “A comprehensive review on Enhanced Oil Recovery by Water Alternating Gas (WAG) injection”. In: *Fuel* 227 (2018), pp. 218–246. DOI: https://doi.org/10.1016/j.fuel.2018.04.015.

[2] Saeed Akbari et al. “Assessment of Polyacrylamide Based Co-Polymers Enhanced by Functional Group Modifications with Regards to Salinity and Hardness”. In: *Polymers* 9 (2017). DOI: 10.3390/polym9120647.

[3] bp. *bp Energy Outlook 2022 edition*. 2022. URL: https://www.bp.com/content/dam/bp/business-sites/en/global/corporate/pdfs/energy-economics/energy-outlook/bp-energy-outlook-2022.pdf.

[4] P.V. Brady. “Why Oil Sticks to Limestone”. In: *Journal of Colloid and Interface Sciences* (Nov. 2011). URL: https://www.osti.gov/servlets/purl/1426917.

[5] *Prediction of Xanthan Rheology in Porous Media*. Vol. All Days. SPE Annual Technical Conference and Exhibition. SPE-18089-MS. Oct. 1988. DOI: 10.2118/18089-MS. URL: https://doi.org/10.2118/18089-MS.

[6] Henry Darcy. *Les fontaines publiques de la ville de Dijon : exposition et application des principes à suivre et des formules à employer dans les questions de distribution d’eau*. Paris: Victor Dalmont, 1856.

[7] Zhenhao Duan et al. “An improved model for the calculation of CO2 solubility in aqueous solutions containing Na+, K+, Ca2+, Mg2+, Cl−, and SO42−”. In: *Marine Chemistry* 98.2 (2006), pp. 131–139. ISSN: 0304-4203. DOI: https://doi.org/10.1016/j.marchem.2005.09.001. URL: https://www.sciencedirect.com/science/article/pii/S0304420305001118.

[8] M.K. Emera and Hemanta Sarma. “A Genetic Algorithm-Based Model to Predict CO-Oil Physical Properties for Dead and Live Oil”. In: *Journal of Canadian Petroleum Technology* 47 (Jan. 2006). DOI: 10.2118/2006-197.

[9] Sherif Fakher and Abdulmohsin Imqam. “A data analysis of immiscible carbon dioxide injection applications for enhanced oil recovery based on an updated database”. In: *SN Applied Sciences* 2 (2020). DOI: 10.1007/s42452-020-2242-1.

[10] John R. Fanchi. “Chapter 6 - Fluid Properties and Model Initialization”. In: *Principles of Applied Reservoir Simulation (Fourth Edition)*. Ed. by John R. Fanchi. Fourth Edition. Gulf Professional Publishing, 2018, pp. 101–120. ISBN: 978-0-12-815563-9. DOI: https://doi.org/10.1016/B978-0-12-815563-9.00006-9. URL: https://www.sciencedirect.com/science/article/pii/B9780128155639000069.

[11] R. Farajzadeh, A. Andrianov, and P. L. J. Zitha. “Investigation of Immiscible and Miscible Foam for Enhancing Oil Recovery”. In: *Industrial & Engineering Chemistry Research* 49.4 (2010), pp. 1910–1919. DOI: 10.1021/ie901109d. URL: https://doi.org/10.1021/ie901109d.

[12] SNF Floerger. *Petroleum Geology | Petroleum Systems | EOR 101*. 2015. URL: https://www.snf.com/wp-content/uploads/2019/12/Petroleum-Geology-Petroleum-Systems-EOR-101-EN.pdf (visited on 11/23/2021).

[13] Marina Freire-Gormaly et al. “Pore Structure Characterization of Indiana Limestone and Pink Dolomite from Pore Network Reconstructions”. In: *Oil & Gas Science and Technology* 71 (Jan. 2015). DOI: 10.2516/ogst/2015004.

[14] Bisweswar Ghosh, Abdullah Al-Hamairi, and Soo Jin. “Carbonated water injection: an efficient EOR approach. A review of fundamentals and prospects”. In: *Journal of Petroleum Exploration and Production Technology* 10 (2019). DOI: 10.1007/s13202-019-0738-2.

[15] Reid B. Grigg and Ucok W.R. Siagian. “Understanding and Exploiting Four-Phase Flow in Low-Temperature CO2 Floods”. In: vol. All Days. 1998. DOI: 10.2118/39790-MS.

[16] *A Theoretical and Experimental Study of the Steady State Capillary End Effect*. Vol. All Days. SPE Annual Technical Conference and Exhibition. Oct. 1956.

[17] Sameer Al-Hajri et al. “An Overview on Polymer Retention in Porous Media”. In: *Energies* 11 (2018). ISSN: 1996-1073. DOI: 10.3390/en11102751.

[18] S.J.T. Hangx. *Behaviour of the CO2-H2O system and preliminary mineralisation model and experiments*. Utrecht University, 2005.

[19] IEA. *Oil demand by scenario, 2010-2030*. 2021. URL: https://www.iea.org/data-and-statistics/charts/oil-demand-by-scenario-2010-2030 (visited on 08/22/2022).

[20] Martijn T. Janssen. “Investigation on foam-assisted chemical flooding for enhanced oil recovery: An experimental and mechanistic simulation study”. In: (2020). DOI: 10.4233/uuid:f98bca0e-5ee8-4fd3-8a60-d0e624e525d6.

[21] Martijn T. Janssen, Fardin Azimi, and Pacelli L. Zitha. “Immiscible Nitrogen Flooding in Bentheimer Sandstones: Comparing Gas Injection Schemes for Enhanced Oil Recovery”. In: SPE Improved Oil Recovery Conference Day 4 Tue, April 17, 2018 (2018). DOI: 10.2118/190285-MS.

[22] S.A. Jones et al. “Effect of surfactant concentration on foam: From coreflood experiments to implicit-texture foam-model parameters”. In: *Journal of Industrial and Engineering Chemistry* 37 (2016), pp. 268–276. ISSN: 1226-086X. DOI: https://doi.org/10.1016/j.jiec.2016.03.041. URL: https://www.sciencedirect.com/science/article/pii/S1226086X16300569.

[23] S. Jouenne. “Polymer flooding in high temperature, high salinity conditions: Selection of polymer type and polymer chemistry, thermal stability”. In: *Journal of Petroleum Science and Engineering* 195 (2020), p. 107545. DOI: https://doi.org/10.1016/j.petrol.2020.107545.

[24] Sunil Kumar and Ajay Mandal. “A comprehensive review on chemically enhanced water alternating gas/CO2 (CEWAG) injection for enhanced oil recovery”. In: *Journal of Petroleum Science and Engineering* 157 (2017), pp. 696–715. ISSN: 0920-4105. DOI: https://doi.org/10.1016/j.petrol.2017.07.066.

[25] Laurent Laboureur, Mario Ollero, and David Touboul. “Lipidomics by Supercritical Fluid Chromatography”. In: *International Journal of Molecular Sciences* 16 (June 2015). DOI: 10.3390/ijms160613868.

[26] L. W. Lake. *Enhanced oil recovery / Larry W. Lake*. Prentice Hall Englewood Cliffs, N.J, 1989. ISBN: 0132816016.

[27] Yeonkyeong Lee et al. “Oil recovery by low-salinity polymer flooding in carbonate oil reservoirs”. In: *Journal of Petroleum Science and Engineering* 181 (2019), p. 106211. ISSN: 0920-4105. DOI: https://doi.org/10.1016/j.petrol.2019.106211.

[28] Hao Lei et al. “Oil Recovery Performance and CO2 Storage Potential of CO2 Water-Alternating-Gas Injection after Continuous CO2 Injection in a Multilayer Formation”. In: *Energy & Fuels* 30.11 (2016), pp. 8922–8931. DOI: 10.1021/acs.energyfuels.6b01307.

[29] *Selection and Screening of Polymers for Enhanced-Oil Recovery*. Vol. All Days. SPE Improved Oil Recovery Conference. Apr. 2008.

[30] *Using Polymer Alternating Gas to Maximize CO2 Flooding Performance*. Vol. Day 2 Tue, June 10, 2014. SPE Trinidad and Tobago Section Energy Resources Conference. 2014. DOI: 10.2118/SPE-169942-MS.

[31] Weirong Li and David Schechter. “Using Polymer Alternating Gas to Maximize CO2 Flooding Performance”. In: *Trinidad and Tobago Energy Resources Conference, SPETT 2014 - Future Assets: Acquisition, Maintenance and Reliability* (2014), SPE-169942–MS. DOI: 10.2118/169942-MS.

[32] Weirong Li et al. “Polymer-Alternating-Gas Simulation—A Case Study”. In: SPE EOR Conference at Oil and Gas West Asia All Days (2014). DOI: 10.2118/169734-MS.

[33] Osama Massarweh and Ahmad S. Abushaikha. “A review of recent developments in CO2 mobility control in enhanced oil recovery”. In: *Petroleum* (2021). ISSN: 2405-6561. DOI: https://doi.org/10.1016/j.petlm.2021.05.002.

[34] O.M. Mathiassen. *CO2 as Injection Gas for Enhanced Oil Recovery and Estimation of the Potential on the Norwegian Continental Shelf*. Norwegian University of Science and Technology, 2003.

[35] F. Mees et al. “Applications of X-Ray Computed Tomography in the Geosciences”. In: *Geological Society, London, UK. Special Publications 15* 215 (Jan. 2003). DOI: 10.1144/GSL.SP.2003.215.

[36] Fanbao Meng et al. “The Effect of Stress on Limestone Permeability and Effective Stress Behavior of Damaged Samples”. In: *Journal of Geophysical Research: Solid Earth* 124 (2019), pp. 376–399.

[37] M. Mirzaie Yegane. “Effect of nanoparticles and pre-shearing on the performance of water-soluble polymers in porous media”. PhD thesis. 2021.

[38] M.J. Mitchell et al. “A model of carbon dioxide dissolution and mineral carbonation kinetics”. In: 466.2117 (2010), pp. 1265–1290. ISSN: 13645021.

[39] A. Nasr El-hoshoudy and M. Desouky. “Carbon Capture, Utilization and Sequestration”. In: *CO2 Miscible Flooding for Enhanced Oil Recovery*. InTech, 2018. DOI: 10.5772/intechopen.7082.

[40] T.A. Osswald and N. Rudolph. *Polymer rheology - Fundamentals and Applications*. Munich: Hanser, 2015. ISBN: 978-1-56990-517-3.

[41] AE Peksa, KHAA Wolf, and PLJ Zitha. “Bentheimer sandstone revisited for experimental purposes”. In: *Marine and Petroleum Geology* 67 (2015), pp. 701–719. ISSN: 0264-8172. DOI: 10.1016/j.marpetgeo.2015.06.001.

[42] Iván Piñerez Torrijos. “Enhanced oil recovery from Sandstones and Carbonates with ”Smart Water””. PhD thesis. Mar. 2017. DOI: 10.13140/RG.2.2.33863.09121.

[43] Masoud Rashidi. “Physico-Chemistry Characterization of Sulfonated Polyacrylamide Polymers for Use in Polymer Flooding”. In: 2010.

[44] Alexander Rock et al. “On the Role of Polymer Viscoelasticity in Enhanced Oil Recovery: Extensive Laboratory Data and Review”. In: *Polymers* 12 (2020), p. 2276. DOI: 10.3390/polym12102276.

[45] Kiani Sajad, Shirin Alexander, and Andrew Barron. “Nanoparticles, Polymers, and Surfactants as Emerging Platforms in Fluid Flow Transport”. In: (May 2020). DOI: 10.13140/RG.2.2.20954.36809.

[46] T Salih, Safaa Hussain Sahi, and Omar Hameed. “Rheological Evaluation of Polymer (Sav 10) For Polymer Flooding Applications”. In: *Journal of Chemical and Petroleum Engineering* 17 (2016), pp. 37–46.

[47] H.. Shahverdi and M.. Sohrabi. “Relative Permeability Characterization for Water-Alternating-Gas Injection in Oil Reservoirs”. In: *SPE Journal* 21.03 (June 2016), pp. 0799–0808. ISSN: 1086-055X. DOI: 10.2118/166650-PA. URL: https://doi.org/10.2118/166650-PA.

[48] Bakul C. Sharma, William E. Brigham, and Louis M. Castanier. “CT imaging techniques for two-phase and three-phase in-situ saturation measurements”. In: 1997.

[49] Ji-Quan Shi, Ziqiu Xue, and Sevket Durucan. “Supercritical CO2 core flooding and imbibition in Tako sandstone—Influence of sub-core scale heterogeneity”. English. In: *International Journal of Greenhouse Gas Control* 5.1 (2011), pp. 75–87. DOI: 10.1016/j.ijggc.2010.07.003.

[50] Shuaishuai Shi, Hadi Belhaj, and Achinta Bera. “Capillary pressure and relative permeability correlations for transition zones of carbonate reservoirs”. In: *Journal of Petroleum Exploration and Production Technology* 8 (Aug. 2017). DOI: 10.1007/s13202-017-0384-5.

[51] N. Sönnichsen. *Daily demand for crude oil worldwide from 2006 to 2020, with a forecast until 2026*. 2021. URL: https://www.statista.com/statistics/271823/daily-global-crude-oil-demand-since-2006/.

[52] K. S. Sorbie. *Polymer-improved oil recovery / K.S. Sorbie*. Blackie ; CRC Press Glasgow : Boca Raton, Fla, 1991. ISBN: 0849371376 0216926939.

[53] A. Thomas. “Polymer Flooding”. In: *Chemical Enhanced Oil Recovery (cEOR) - a Practical Overview*. InTech, 2016. DOI: 10.5772/64623.

[54] Francisco D. Tovar, Maria A. Barrufet, and David S. Schechter. “Long Term Stability of Acrylamide Based Polymers during Chemically Assisted CO2 WAG EOR”. In: SPE Improved Oil Recovery Conference All Days (2014). DOI: 10.2118/169053-MS.

[55] Pennsylvania State University. *Rheometry - Flow in capillaries, slits and dies driven by pressure (poiseuille devices) capillary rheometer*. URL: https://zeus.plmsc.psu.edu/~manias/MatSE447/14_Rheometry2.pdf.

[56] Mahendra Kumar Verma. “Fundamentals of carbon dioxide-enhanced oil recovery (CO 2 -EOR): a supporting document of the assessment methodology for hydrocarbon recovery using CO 2 -EOR associated with carbon sequestration”. In: 2015.

[57] Lei Wang et al. “Advances in improved/enhanced oil recovery technologies for tight and shale reservoirs”. In: *Fuel* 210 (2017), pp. 425–445. ISSN: 0016-2361. DOI: https://doi.org/10.1016/j.fuel.2017.08.095. URL: https://www.sciencedirect.com/science/article/pii/S0016236117310906.

[58] Xinrong Wang et al. “Miscibility characteristics of the CO2/n-hexadecane system with presence of water component based on the phase equilibrium calculation on the interface region”. In: *Colloids and Surfaces A: Physicochemical and Engineering Aspects* 629 (2021), p. 127463. ISSN: 0927-7757. DOI: https://doi.org/10.1016/j.colsurfa.2021.127463. URL: https://www.sciencedirect.com/science/article/pii/S0927775721013327.

[59] S.L. Wellington and H.J. Vinegar. “X-Ray Computerized Tomography”. In: *Journal of Petroleum Technology* 39.08 (Aug. 1987), pp. 885–898. ISSN: 0149-2136. DOI: 10.2118/16983-PA. URL: https://doi.org/10.2118/16983-PA.

[60] Benjamin Werner. “The Influence of Drilling Fluid Rheology on Cuttings Bed Behavior”. PhD thesis. Jan. 2018. DOI: 10.13140/RG.2.2.19105.30566.

[61] Quan Xie et al. “pH effect on wettability of oil/brine/carbonate system: Implications for low salinity water flooding”. In: *Journal of Petroleum Science and Engineering* 168 (2018), pp. 419–425. ISSN: 0920-4105. DOI: https://doi.org/10.1016/j.petrol.2018.05.015. URL: https://www.sciencedirect.com/science/article/pii/S0920410518304078.

[62] M.J. Blunt Y. Tanino. “Laboratory investigation of capillary trapping under mixed-wet conditions”. In: *WATER RESOURCES RESEARCH* 49 (2013), pp. 4311–4319. DOI: 10.1002/wrcr.20344. URL: https://doi.org/10.1002/wrcr.20344.

[63] Yongzhi Yang et al. “Using Polymer Alternating Gas to Enhance Oil Recovery in Heavy Oil”. In: *IOP Conference Series: Earth and Environmental Science* 113 (2018), p. 012182. DOI: 10.1088/1755-1315/113/1/012182.

[64] Yiping Zhang, Sam S. Huang, and Peng Luo. “Coupling Immiscible CO2 Technology and Polymer Injection to Maximize EOR Performance for Heavy Oils”. In: *Journal of Canadian Petroleum Technology* 49 (2010), pp. 25–33. ISSN: 0021-9487. DOI: 10.2118/137048-PA.

A

Error propagation analysis

Throughout this study, the individual errors are evaluated through the error propagation principals. These propagation of uncertainties in terms of formulas are presented in this appendix, with one example from the study itself.

When multiple variables ($w, x...z$) are measured with their corresponding uncertainties ($\delta w, \delta x...\delta z$) and used to compute a new component q, the individual uncertainties will cause the new uncertainty (δq) of q as follows:

Sum and difference
When q is a function of the sum and difference of variables, $q = w + x - y$, then the uncertainty will be:

$$\delta q = \sqrt{(\delta w)^2 + (\delta x)^2 + (\delta y)^2} \tag{A.1}$$

Product and quotient
If q is a function of the product or quotient of variables, $q = \frac{w*x}{y*z}$, then:

$$\delta q = |q|\sqrt{(\frac{\delta w}{w})^2 + (\frac{\delta x}{x})^2 + (\frac{\delta y}{y})^2 + (\frac{\delta z}{z})^2} \tag{A.2}$$

Exact value
When a computation contains an exact value, $q = Ax$, then the uncertainty will follow as:

$$\delta q = |A|\delta x \tag{A.3}$$

Power
If q is a power function, $q = x^n$, the uncertainty will be:

$$\delta q = |n|\frac{\delta x}{|x|} \tag{A.4}$$

One variable function
If the function only consists out of one variable, $q(x)$, then:

$$\delta q = |\frac{\delta q}{|}\delta x \delta x \tag{A.5}$$

Any function with multiple variables
Lastly, if a function contains multiple variables and is relaying on any of the previous presented functions, then the uncertainty of q will be:

$$\delta q = \sqrt{(\frac{\delta q}{\delta w}\delta w)^2 + ... + (\frac{\delta q}{\delta z}\delta z)^2} \tag{A.6}$$

Example from this study
Here, an example computations from this study can be found, based on the above given principles of error propagation:

$$PV_{injected} = T_{t-1} + \Delta T * u/PV_{core} \tag{A.7}$$

- Previous PV_{inj}: PV_{t-1}, with $\delta T_{t-1} = 0.03(min)$. It start at the timing of the fluid reaching the core, for which an error of 1.5 seconds (= 0.025 min) is uphold;
- Difference in time between this step and the previous: $\Delta T = 0.167(min)$, with $\delta \Delta T = 0.01(min)$;
- The injection rate u, with δu is coming from the accuracy of the Quizix pump, which states an accuracy of $\pm$ 0.1% of the injection rate ($0.5ml/min$ gives $\delta u = 0.0005ml/min$);
- The error on the total pore volume of the core, PV_core, with $\delta PV_{core} = 1.3$;

The individual variables with their error and Equation A.7 lead to the error propagation function of the injected PV:

$$\delta q = \sqrt{(\frac{\delta q}{\delta PV_{t-1}}\delta PV_{t-1})^2 + (\frac{\delta q}{\delta \Delta T}\delta \Delta T)^2 + (\frac{\delta q}{\delta u}\delta u)^2 + (\frac{\delta q}{\delta PV_{core}}\delta PV_{core})^2} \tag{A.8}$$

$$\delta q = \sqrt{(1 * \delta PV_{t-1})^2 + (\frac{u}{PV_{core}}\delta \Delta T)^2 + (\frac{\delta \Delta T}{PV_{core}}\delta u)^2 + (-(\frac{\Delta T}{PV_{core}^2}\delta u) * \delta PV_{core})^2} \tag{A.9}$$

$$\delta q = 3 * 10^{-2} \tag{A.10}$$

B

Dopant analysis core-flood experiments

In order to work with a proper contrast between fluid phases during core flooding experiments, a dopant analysis was carried out to find the right combination between dopant and fluids. The works of Janssen (2020)[20] , Wellington and Vinegar (1987)[59], Farajzadeh, Andrianov, and Zitha (2010)[11] and Shi, Xue, and Durucan (2011)[49] were conducted for insights on dopant concentration in order to retrieve good contrast between oil and aqueous phases during core-floods for recovery purposes. These dopant concentration were tested in the CT-scan at multiple energy levels at single and dual energy. Table B.1 represents the results of this testing, with the mean value and the standard deviation of the measurement.

Besides the research from the 4 different parties mentioned before, the personal experiences and thoughts of Martijn Janssen and Ellen Meijvogel were consulted. This consultation resulted in the advice to dope one of the phases instead of two, as only a large enough contrast is needed instead of the need to dope all. By only doping the oil phase, the possibility of creating a different environment for the polymer solution where it can react with the dopant is avoided. Good contrast between the polymer solution and the oil phase were found by doping the oil with 20 wt% 1-iododecane. The 40 wt% oil doped phase was found to give Hounsfield values outside the maximum range (max is 3071) of the medical CT scanner. Saturated in the core sample, HU reading are even more increased and therefore not a valid option. 10 wt% KI in oil was also a good option, but with dual energy 80kV, the maximum is also reached. 5 wt% NaI gives resuled as well in a contrast that could is large enough for proper distinction between the phase, however the option of a doped oil phase is more preferred. The sodium tungstate dihydrate gives a very cloudy and not homogeneous solution.

Table B.1: Measured values for different doped samples in bulk in Hounsfield units (HU).

type Energy level	Single 80kV		Dual 80kV		Single 140kV		Dual 140kV		Single 100 kV	
	mean	std	mean	std	mean	std	mean	std	mean	std
11,235 wt% sodium *dihydrate (polymer)	1738.8	31.9	1756.1	16.4	1731.2	23	1739.5	12.1	1912.6	24.1
n-Hexadecane + Red O	-279.9	15.3	-278.7	6.5	-243.3	12.4	-243	5.4	-261.2	13.8
10 wt% KI (polymer)	2966.1	53.9	3058.4	15.6	1479.5	28.5	1499	26.4	2195.6	37.5
40 wt% 1-iododecane (oil)	3070.9	0.4	3071	0.2	1980	58.1	2001.6	55.1	3070.4	4.7
Shell brine 3,52 wt%	67	17.7	70.9	7.8	44	13.2	43.4	5.7	54.3	14.7
SAV-10 XV 0,2 wt%	67	16	69.9	8.1	42	12.5	41.8	7.6	54.3	13.8
20 wt% 1-iododecane (oil)	2427.5	59.7	2514.5	34.1	1106.2	31.3	1107.3	25.8	1748.1	42.2
5 wt% NaI (polymer)	1716.2	37.2	1777	20.3	904.3	22.3	912.3	15	1299.5	28.1
Air	-999.7	11.2	-1002.7	5.3	-998	9.7	-998	4.1	-999.7	9.2

C

Vertical scanning exploration

Before the totality of experimental core-floods, the possibility for vertically orientated cores was explored. Janssen(2020)[20], who worked in the same laboratory with the same CT scanner on his experimental study, reported difficulties with vertical orientated core-floods with CT imaging. Following the findings from Mees et al.(2003)[35], the artefacts in vertical scanning occur by the fact that with this orientation, the diagonal X-ray pathways through the scanned object are greater than the pathways from the sides, creating apparent X-shaped artefacts over the retrieved image from the scanned object. These artefacts will change position with every new scan or slice of an individual scan, regardless of the method of scanning (spiral or sequential). This inhibits the method of substracting the artefacts from every image. The lower the energy level of the scan performed, the more excessive the artefacts turn out to be (140 kV the least, 80 kV the most). For the performed exploration study to vertical scanning possibilities, a longer core length of 17 $\pm$ 0.01 cm and a shorter core length of 8.71 $\pm$ 0.01 cm (both 3.8 $\pm$ 0.01 cm in diameter) were used. The shorter core would make the scanned object length and width dimensions more equal to create a smaller difference between the diagonal X-ray pathways and the side way X-ray paths. Both spiral and sequential scanning techniques were used at different energy levels for both the long and short core. The results of this study are presented below in the form of the scanned images and there retrieved HU readings with the standard deviation of these measurements and for comparison the calculated porosity using Equation 3.7. Based on these results, it was decided that vertical scanning with the present medical CT scanner, optimized for horizontal orientated human bodies, was not an reasonable option for the core flood experimental study performed. It suffered from excessive artefacts, whereas the horizontal orientated cores gave very reliable and repeatable results.

Table C.1: HU readings and calculated porosities for the vertically scanned long core of 17 $\pm$ 0.01 cm in wet and dry state, compared to a horizontally scanned 17 $\pm$ 0.01 cm core in spiral mode and the porosity calculated by a water imbibition experiment.

	140 kV		80 kV	
	Mean HU	Std.	Mean HU	Std.
Vertical orientated core spirally scanned				
Dry	1137.9	68.9	990.1	196.8
Wet	1308.7	73.7	1037.4	221.9
Avg. porosity	0.164	0.009	0.044	0.008
Vertical orientated core sequentially scanned				
Dry	1005.8	111.2	1258.0	334.5
Wet	1137.5	123.7	1348.5	346.0
Avg. porosity	0.126	0.004	0.08	0.003
Horizontal orientated core spirally scanned				
Dry	1160.1	63.2	1546.3	96.1
Wet	1393.7	53.0	1782.5	84.4
Avg. porosity	0.224	0.001	0.220	0.002
Imbibition experiment porosity	0.227			

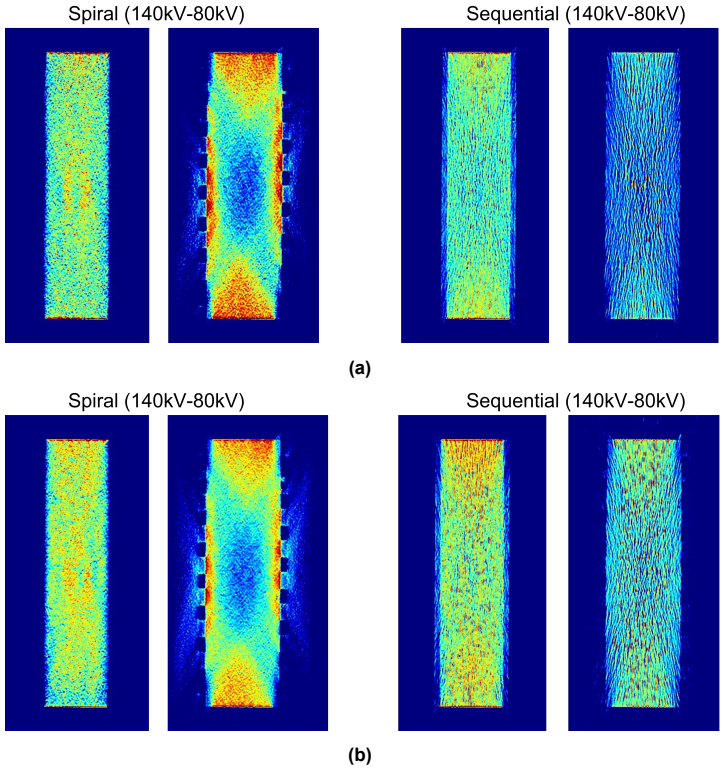

Figure C.1: Vertical scanning performed on the 17 $\pm$ 0.01 cm core in dry (a) and saturated with brine (b) state.

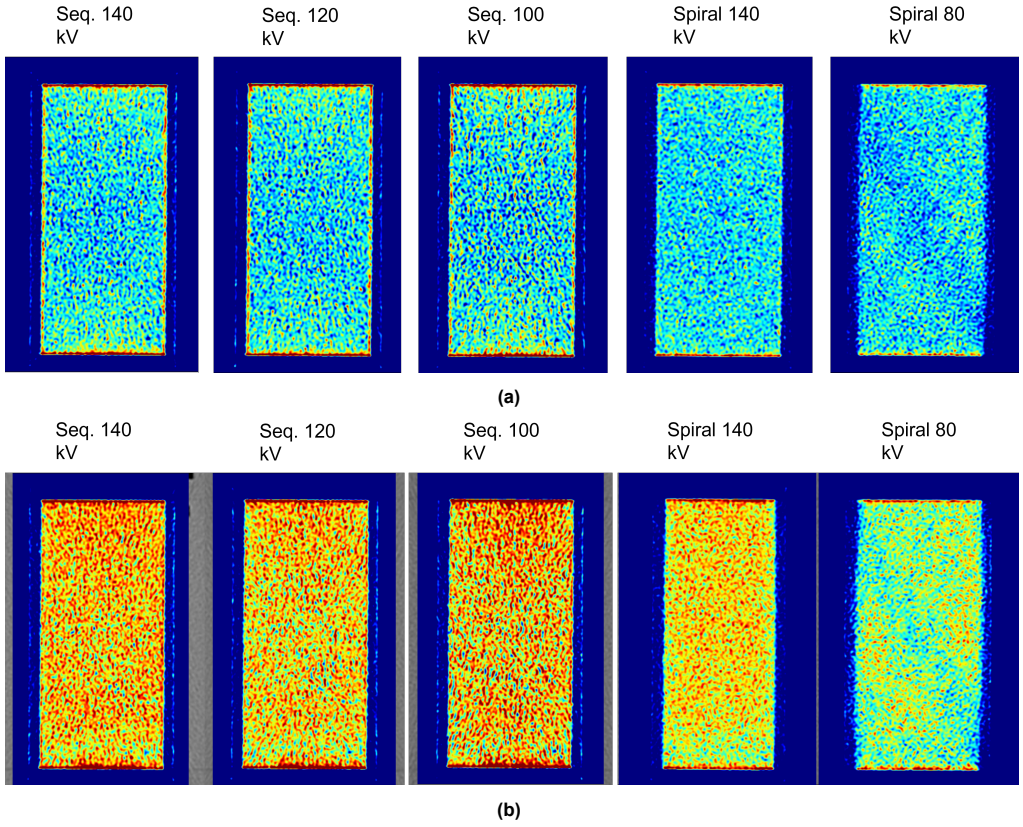

Figure C.2: Vertical scanning performed on the 8.71 $\pm$ 0.01 cm core in dry (a) and saturated with brine (b) state.

Table C.2: HU readings and calculated porosities for the vertically scanned short core of 8.71 $\pm$ 0.01 cm in wet and dry state, compared to a horizontally scanned 17 $\pm$ 0.01 cm core in spiral mode and the porosity calculated by a water imbibition experiment.

	140 kV		80 kV		120 kV		100 kV	
	Mean HU	Std.	Mean HU	Std.	Mean HU	Std.	Mean HU	Std.
Vertical orientated core spirally scanned								
Dry	1119.6	71.0	1495.6	108.2	-	-	-	-
Wet	1303.6	73..8	1646.9	113.1	-	-	-	-
Avg. porosity	0.185	0.003	0.152	0.004	-	-	-	-
Vertical orientated core sequantially scanned								
Dry	1082.3	66.1	-	-	1141.2	70.2	1236.1	80.1
Wet	1253.1	69.9	-	-	1310.5	73.9	1401.0	85.3
Avg. porosity	0.172	0.002	-	-	0.170	0.002	0.166	0.001
Horizontal orientated core spirally scanned								
Dry	1160.1	63.2	1546.3	96.1	-	-	-	-
Wet	1393.7	53.0	1782.5	84.4	-	-	-	-
Avg. porosity	0.224	0.001	0.220	0.002	-	-	-	-
Imbibition experiment porosity	0.227							

D

Mass flow controller conversion

For CO_2 injection throughout the course of all the experiments, a Bronkhorst EL-FLOW mass flow controller is used. In order to implement the desired injection flow rate to the system, a conversion is needed from our desired flow rate of 0.5 cm^3/min (mL/min) of CO_2 , to mLn/min of CH_4 the specific mass flow controller is calibrated for at 150 bars of pressure and 20°C of temperature. The maximum flow rate this mass flow controller can inject with is 25 mln/min of CH_4. Via the Bronkhorst conversion page, the conversion factor of CO_2 to CH_4 is retrieved as 1.056. Along with this conversion factor and the parameters found in Table D.1, the gas law can be used to convert for the desired flow rate input of 9.89 mLn/min:

$$Q_{massflow} = CF \cdot \frac{Q_{CO_2} \cdot P_{res} \cdot T_{normal}}{P_{normal} \cdot T_{res}} \tag{D.1}$$

Table D.1: Mass flow controller conversion parameters.

	Value	Units
CF	1.056	-
Q_{CO_2}	0.50	cm^3/min
P_{res}	20	bar
T_{res}	313.15	K
T_{normal}	293.15	K
P_{normal}	1	bar

E

CT image processing

In the form of two flow charts, the working protocol is described in this section that was followed to retrieve data from the scans performed during the experiments with the aid of the medical CT-scanner and visualize the saturation developments along the core. The ImageJ flow chart describes the workflow in order to retrieve the Hounsfield Unit readings from the representative section of the core over all slices of the scan, both 140 and 80 kV, and the visualization of the orthogonal view along the core used for some experiments. Without applying the Color Balance image adjustment step in ImageJ, the HU measurements from the scan are not affected and stay the original value from the CT scan. The Color Balance adjustment is only for visualization, from which the 140 kV is used in this thesis as it is more representative. This Color Balance setting can be found in Table E.1. The Avizo flow chart represents the work performed in order to visualize the 3D representation of the core for the main results of this experimental study. The Avizo workflow uses the corresponding colors of the different processes from the software itself, for the relevant instructing blocks in the flow chart. The adjusted values for the color scheme can be found in Table E.1.

Table E.1: ImageJ and Avizo color balance/scheme adjusted settings.

	ImageJ	Avizo
MIN	1000	250
MAX	1750	700

ImageJ

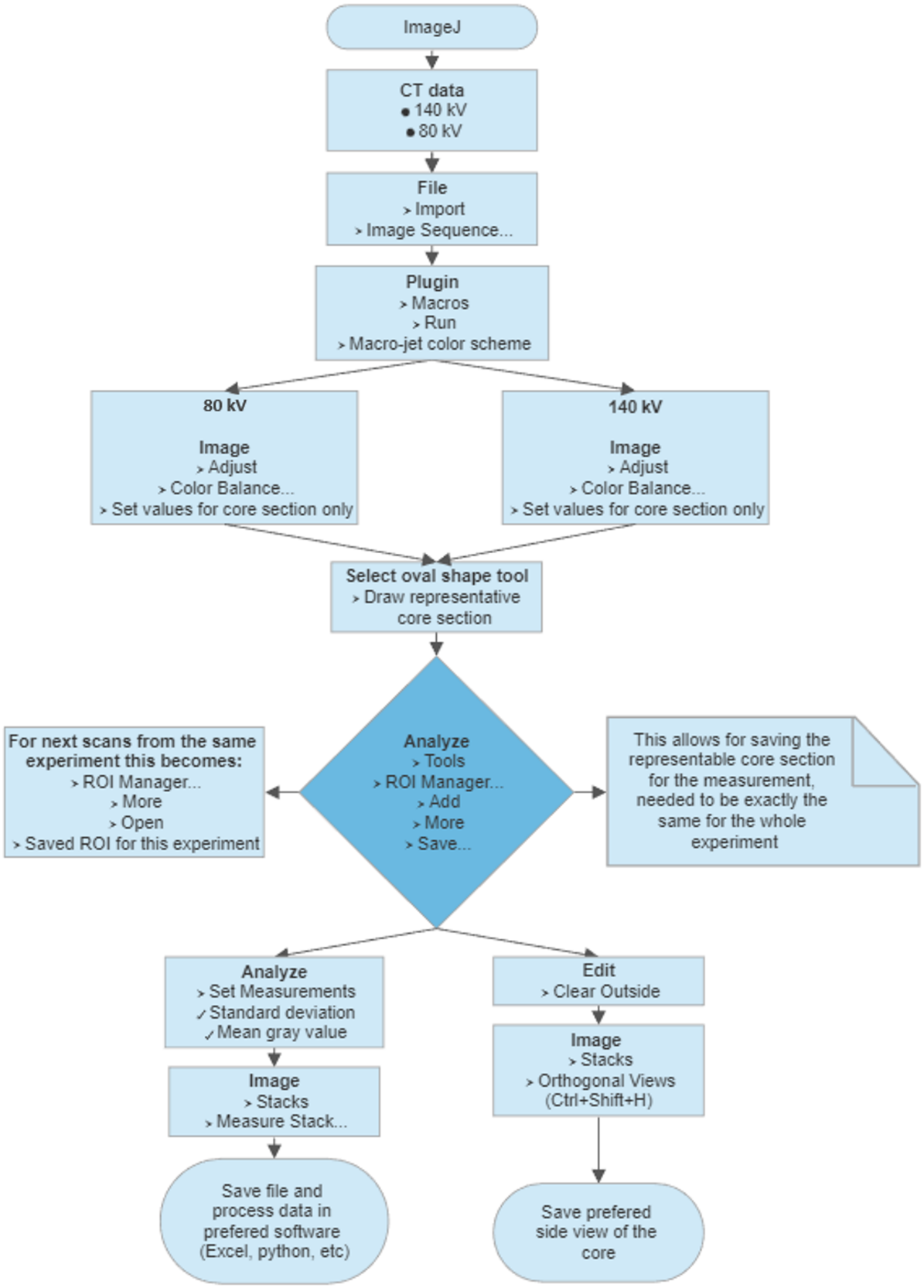

Figure E.1: ImageJ workflow flow chart, describing the process that was used in order to retrieve the data from the CT-scans in order to compute the porosity and saturations throughout the experiments, as well as the way to visualize the orthogonal view along the core to see the saturation profile.

Avizo

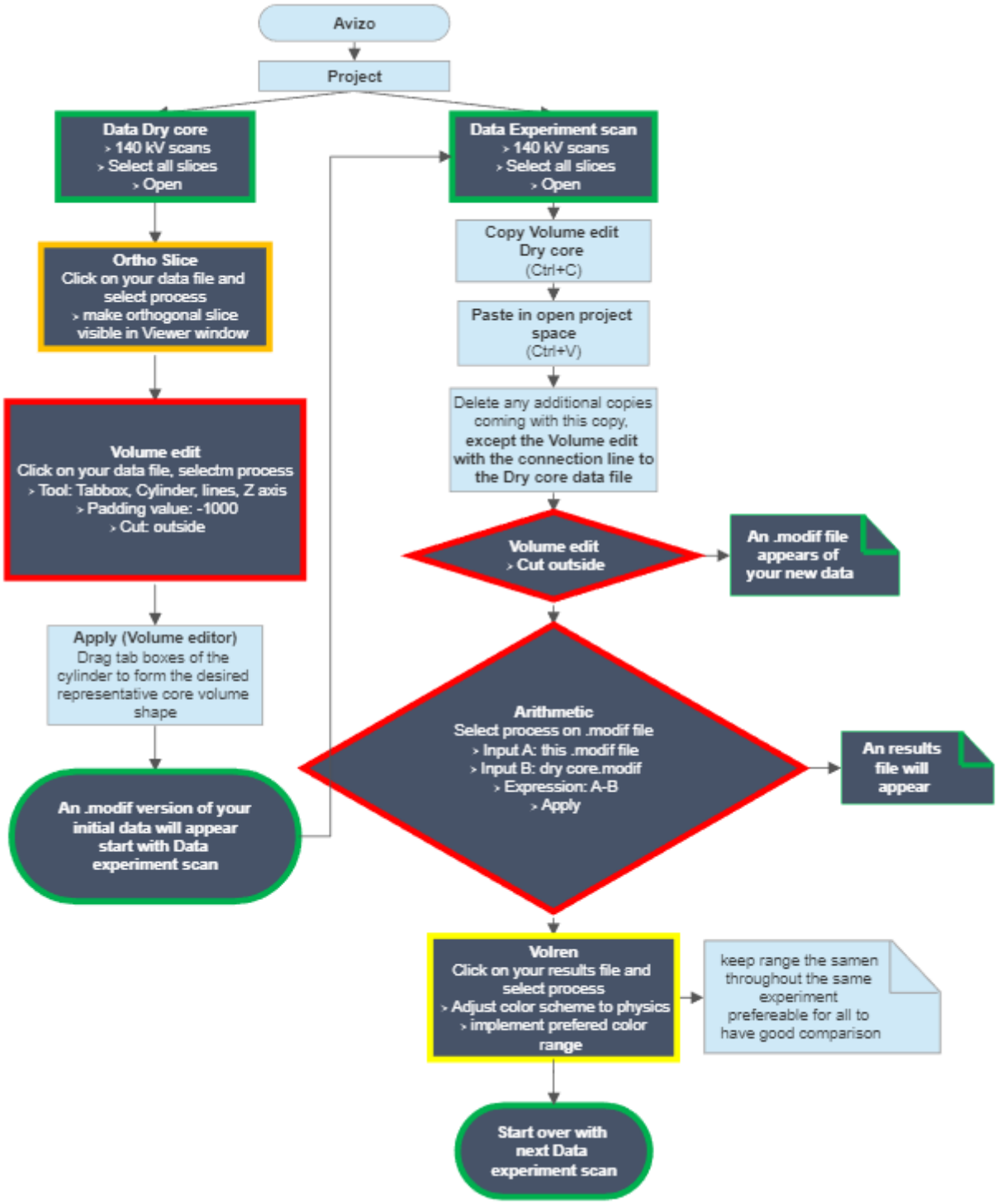

Figure E.2: Avizo workflow flow chart, describing the process followed in order to visualise the CT-scans throughout this study.

F

Primary drainage

Polymer flooding followed by CO_2 flooding: experiment 1

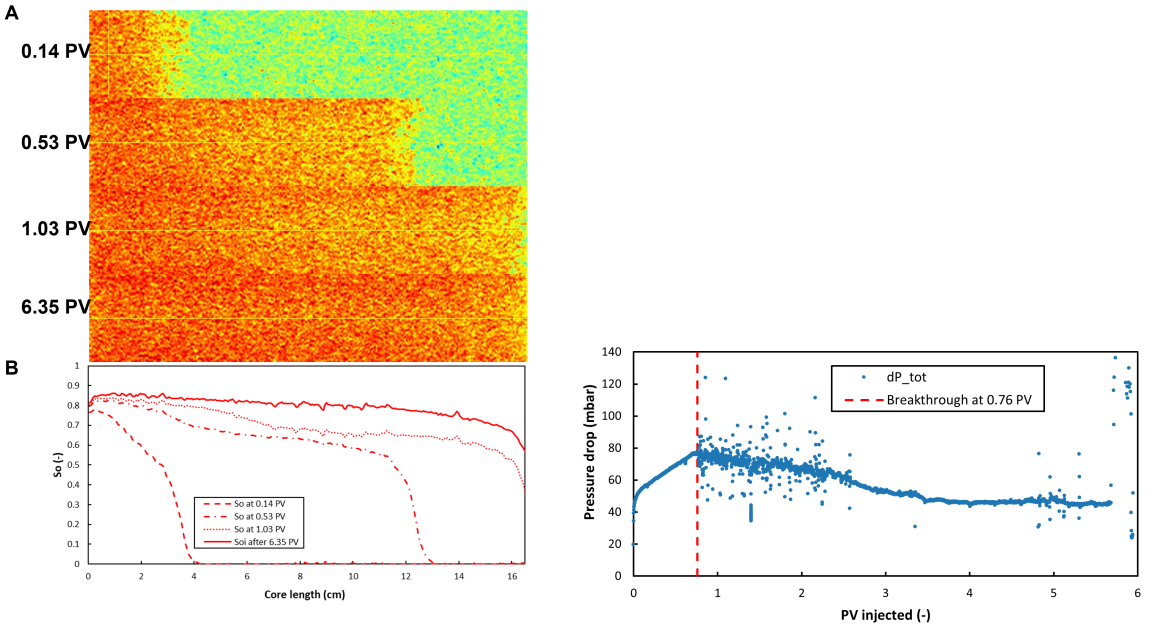

(a) (b)

Figure F.1: (a) Displacement profile of the oil during primary drainage during the given experiment with (A) CT images and (B) oil saturation profile. PV indicates the amounts of oil phase injected during the primary drainage at the times of the performed scan and calculated saturation profile. (A) CT-images made with the medical CT scanner (subsection 3.5.2) and processed with both ImageJ and Avizo (see subsection 3.5.4) to retrieve the average Hounsfield units per slice needed for the S_o calculations and visualisation in 3D respectively. The oil phase (blue/green to yellow/orange) is being injected from the left side into the core, displacing the brine (light blue/white). As the amount of injected PV's of oil increases, the S_o increases accordingly, visible by the overall increase of the higher saturation indicating colour yellow. The propagating front can be traced to the saturation profile in the graphs below. (B) Profile of S_o presenting the primary drainage injection phase at different moment in terms of PV's of oil injected. The oil front can be traced back to the piston like displacement visible in the CT-images above. AS the number of PV's injected increase, the average S_o increases accordingly until the S_{oi} is reached.
(b) Total pressure drop profile for the primary drainage stage before polymer flooding followed by CO_2 flooding in Bentheimer sandstone, experiment 5. The oil injection for the primary drainage is done at 0.5 cm^3/min for approximately 5 pore volumes (PV's). Thereafter, the injection flow rate was increased to 2.5 cm^3/min to initiate the bump flood for the oil phase and further reduce the water saturation towards S_{wc}. After the stabilization of the pressure at the higher flow rate, the injection flow rate was varied from 0.5 to 1.25 and 2.5 cm^3/min to establish a representative, stable, stair shaped pressure drop profile in order to obtain k^e_{ro}. The breakthrough time of the oil phase is given by the red-dotted line.

Polymer flooding followed by CO_2 flooding (repetition): experiment 2

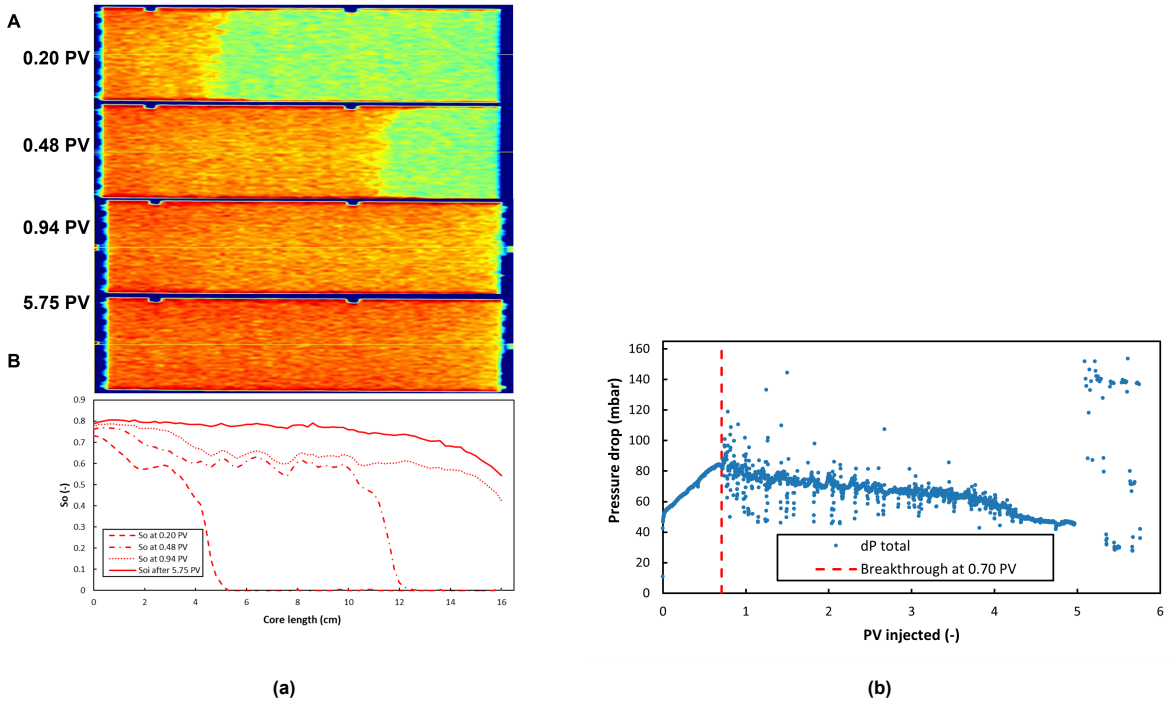

Figure F.2: See caption of Figure F.1

CO_2 flooding followed by polymer flooding: experiment 3

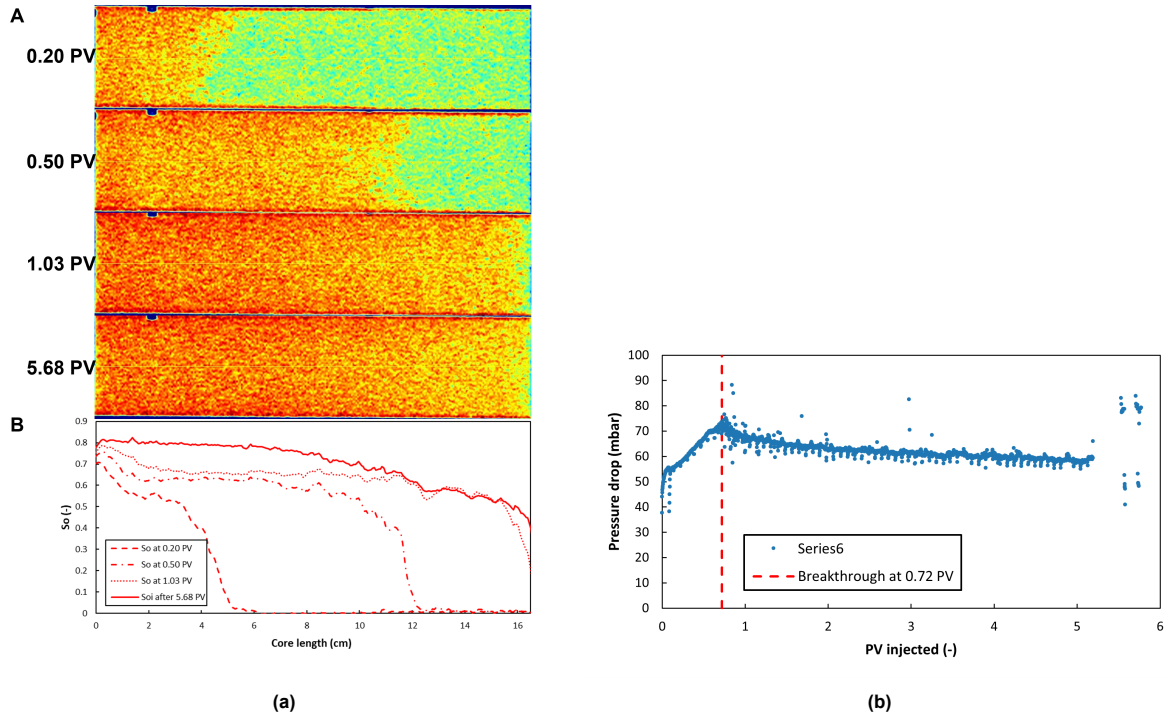

Figure F.3: See caption of Figure F.1

Water Alternating Gas injection: experiment 4

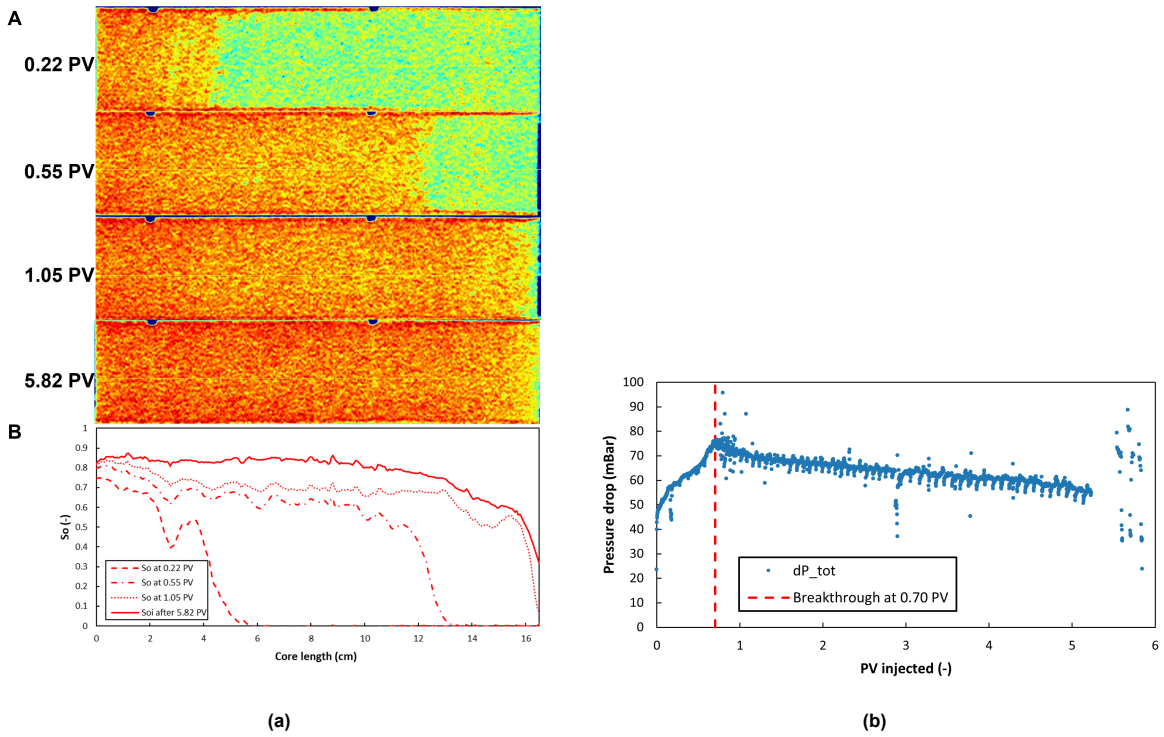

Figure F.4: See caption of Figure F.1

G

Polymer flooding followed by CO_2 flooding

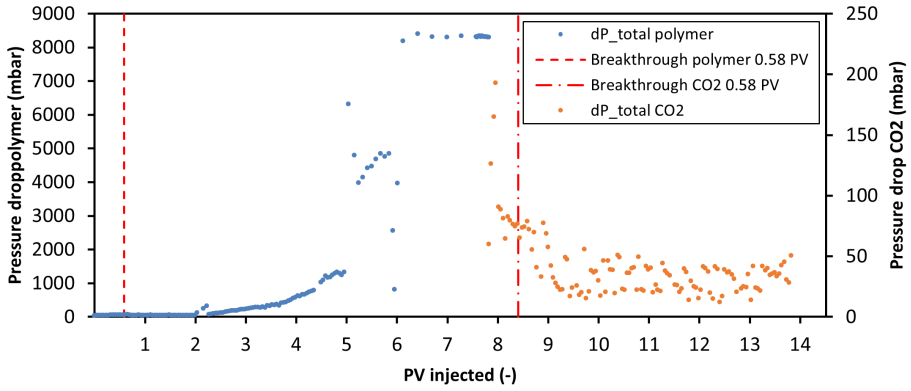

Figure G.1: Pressure drop profile of the polymer flooding and CO_2 flooding for experiment PF+CO_2 (exp. 1), with breakthrough of polymer at 0.58 PV and CO_2 at 0.58 PV as well.

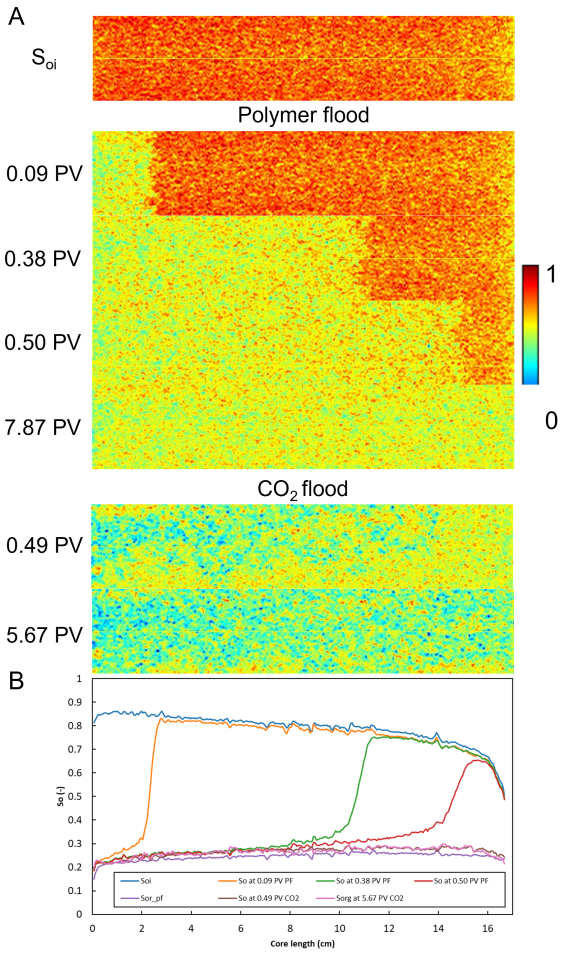

Figure G.2: S_o profile with the corresponding CT-scans during the polymer flood followed by the CO_2 flood of the first experiment. An $S_{or,PF}$ of 0.32 $\pm$ 0.03 and S_{or,CO_2} of 0.30 $\pm$ 0.03 are reached.

H

Oil swelling experiments

The oil swelling effect is investigated at atmospheric pressure in order to validate the effluent readings from which the recovery is determined during the core-flood experiments. The potential swelling is evaluated in the form of two small scale experiments. The first evaluates the if any change occurs in the system with only n-hexadecane (along with dopant agent and Oil Red O) at a low, mid and high case of injected CO_2 . The low, mid, high cases are determined from mole fractions during the core flood using CO_2 as a secondary flooding method, where the respective amounts of oil and CO_2 in contact in the core are the highest of the core-flood experiments. the cases refer to the amounts of CO_2 with respect to the oil phase. The low case taken from the mole fractions just after CO_2 breakthrough determined with volumetric balance, the mid case is at the end of the CO_2 flood and also determined from the volumetric balance and the high case comes from the mole fractions retrieved from CT data. The second experiment evaluates a three phase system with the n-hexadecane, brine and CO_2 at the mid case scenario in terms of mole fractions between oil and CO_2 from the previous experiment. The low, mid and high cases are now distinct from one an other in terms of respective brine volume in the system. During all the experiments, the amounts of CO_2 are injected with a Coriolis meter into the small vials which were also used for determining recovery and phase cuts during the core floods. The system is than led to stabilize for an hour and lightly shaken every 10 minutes. After the hour, the system is opened to simulate the collection at the core-flood experiments (not a closed off system). The fluid levels are then evaluated and compared with the levels before CO_2 injection. During all cases, no visible changes in fluid level is observed which could have led to any incorrect readings during the recovery determinations. The mole fractions determined are visible in Table H.1 and the visualization of the swelling experiments can be seen in figures H.1a and H.1b.

Table H.1: Mole fractions determined from the core-experiment during the use of CO_2 as a secondary recovery method.

	Mole fraction oil	Mole fraction CO_2	Molar concentration CO_2 (mole/L)
LOW	0.915	0.085	0.0007
MID	0.879	0.121	0.0010
HIGH	0.843	0.157	0.0014

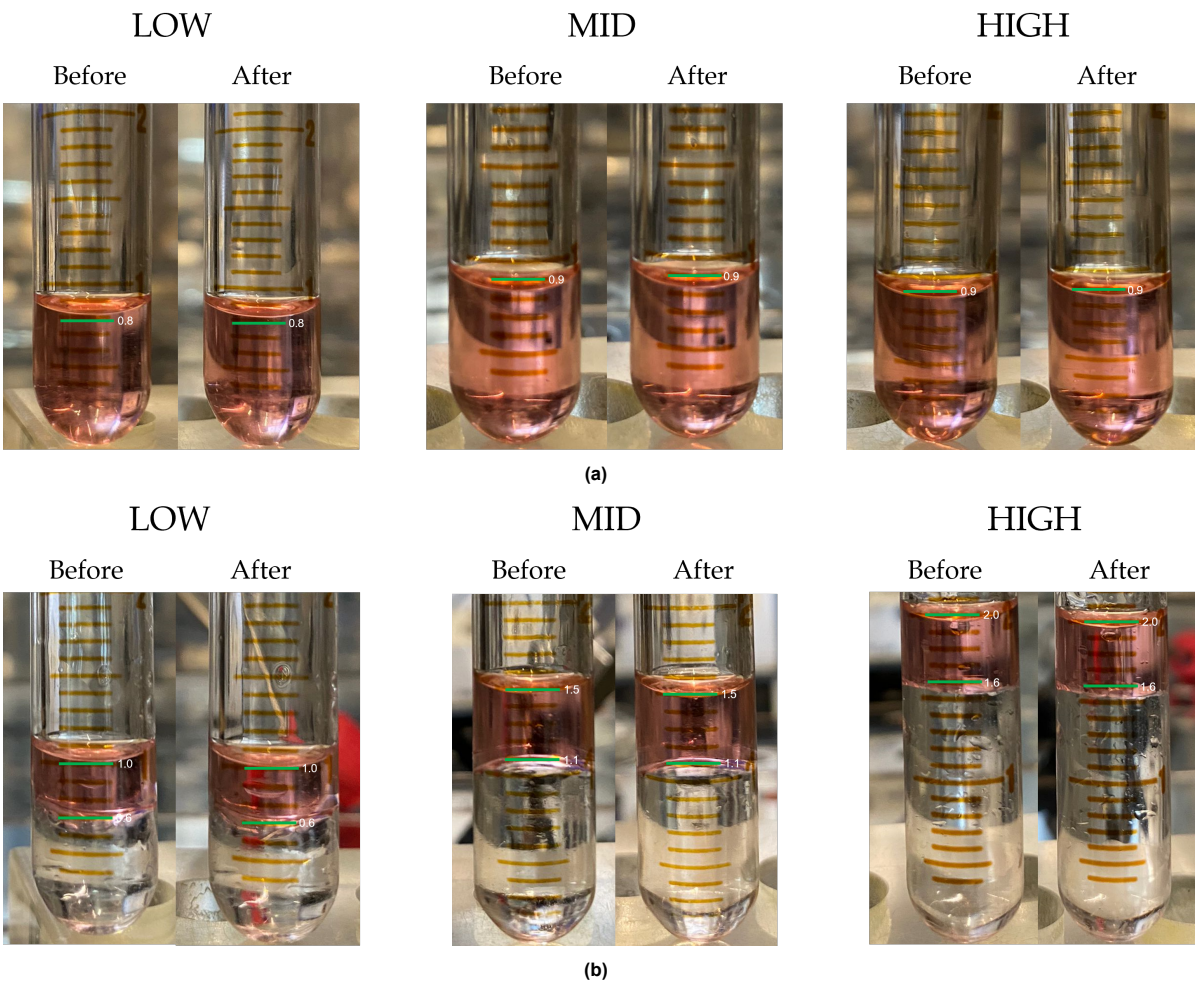

Figure H.1: Small scale oil swelling experiments for recovery determination confirmation. The nearest volume markers are highlighted to illustrate any potential changes. (a) Two phase system tests with n-hexadecane (doped with 20 wt% 1-iododecane and <0.0006wt% Oil Red oil) and CO_2 at the low, mid, high case.

Indiana limestone dry and wet core

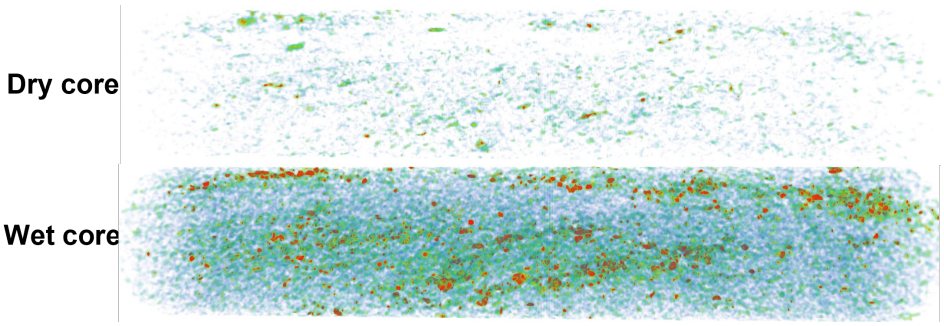

Figure I.1: Dry and wet core for the Indiana limestone used for the experiment with the rest of the results presented in subsection 4.3.5.

J

Comparison polymer degradation with CO_2 at 60 and 80 s^{-1}

Figure J.1 illustrates the comparison of the rheometer results of the polymer solution aged in the presence of CO_2 for the shear rate of 80 s^{-1} which the capillary imposes on the polymer during injection at 0.03 cm^3/min against the shear rate of 60 s^{-1} during the PA-WAG injection. Both show very similar trends in terms of viscosity ratio, only the initial decrease at 60 s^{-1} was slightly more significant, dropping towards 50.2 $\pm$ 5.3%. This is due to the flattening of the shear thinning slope (see Figure 4.3b under the presence of CO_2 during aging.

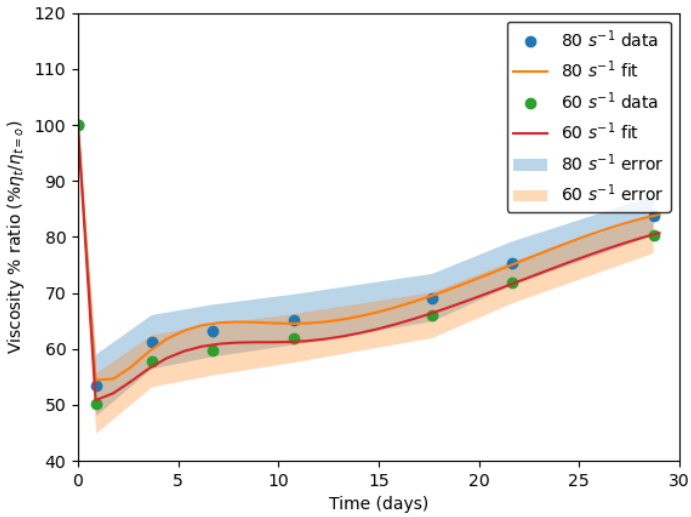

Figure J.1: The rheometer results of the aging experiment in the presence of CO_2 for the fixed shear rate of 80 s^{-1} of the capillary experiment compared against the estimated shear rate of 60 s^{-1} during the PA-WAG injection.

K

Polymer degradation test under oxygen containing conditions

Previously, an stability test of the polymer solution was performed with an a different protocol, namely without creating the oxygen free environment or adding the oxygen scavenger to the polymer. The polymer is very perceptive to oxygen and can quickly degrade when exposed to oxygen without the proper preparation of the sample. Therefore, the new revised protocol was designed, which can be seen in subsection 3.3.2. The previous experiment clearly shows a fast degraded polymer solution in both the capillary as in the rheometer. This gives a good indication of the well executed new protocol and the thermal stability test presented in Figure 4.29a and with that ruling out the impact of oxygen on the stability test with CO_2 .

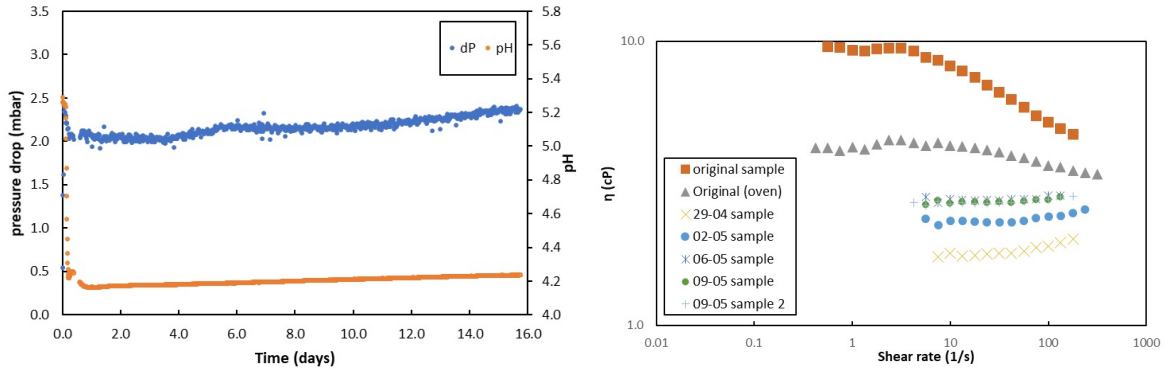

(a) (b)

Figure K.1: Results stability experiment with old protocol, meaning without oxygen measures. (a) pH and dP measurements from the degradation experiment, showing significant lower values as has been reported for the new protocol (see Figure 4.1. (b) The rheometer results from the degrading polymer with CO_2 . The original sample, without CO_2 , is already degraded, with a decreased viscosity compared to the normal original samples. The polymer almost behaves Newtonian at some point during the stability experiment.

Aging HPAM in the presence of CO_2

An aging experiment performed by Tovar, Barrufet, and Schechter (2014) [54] of HPAM in the presence of CO_2 .

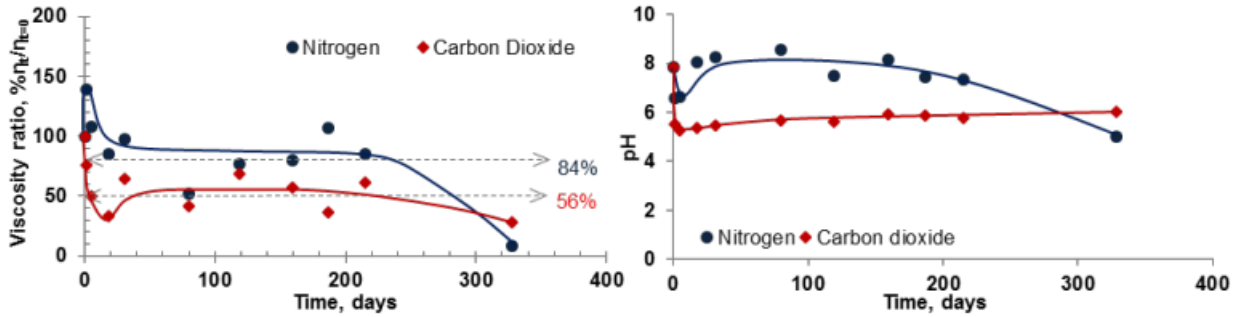

Figure L.1: The viscosity retention and pH as a function of time for the aging of HPAM polymer solution in the presence of nitrogen and CO_2 at 50 °C, atmospheric pressure and a shear rate of 20 s^{-1} [54].

M

Separate dP sections WAG and PA-WAG in Bentheimer sandstone

For the evaluation of the delay in aqueous phase breakthrough and the virtual stationary polymer front during the CO_2 injection of the second cycle, compared to the movable water front of the WAG injection.

During the first aqueous slug injection, both reach the second section of the core (dP2). During the injection of the first CO_2 slug, the brine front continued moving and elevated the pressure drop in dP section 3, ultimately leading to the breakthrough at the end of the first complete cycle. The polymer front remained stationary in the middle dP section, visible in the fact that the pressure in dP section 3 only rises slightly at the start of the CO_2 injection, followed by the return to the stationary pressure around 4 mbar during the rest of the injection of the first CO_2 slug. Halfway the injection of the second cycle, the polymer front reaches the third cycle, leading to the breakthrough of polymer at the end of this polymer slug.

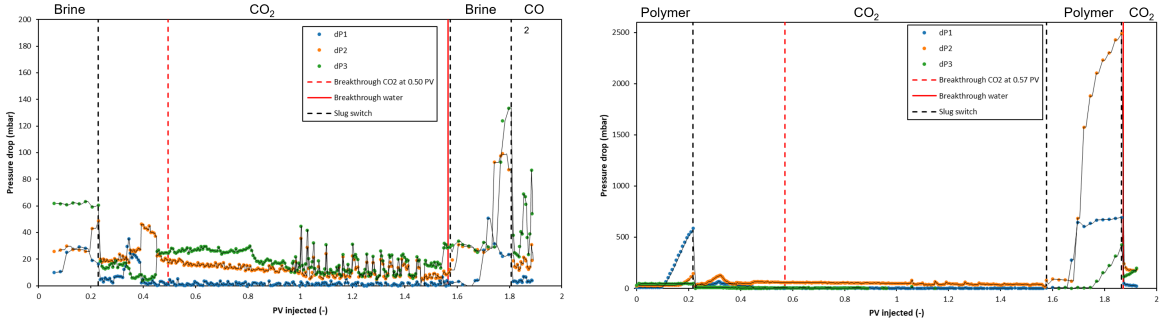

(a) **(b)**

Figure M.1: Separate dP sections of the WAG (a) and PA-WAG (b) injection experiments in Bentheimer sandstone.